THERMOELECTRIC PROPERTIES OF NOVEL MICROSTRUCTURALLY MODIFIED $CoSb_3$ SKUTTERUDITE MATERIALS BY MINOR DOPANTS OF Mn, Hf, Al, Bi AND Yb

MOHAMED HAMID ELSHEIKH YOUSEF

FACULTY OF ENGINEERING
UNIVERSITY OF MALAYA
KUALA LUMPUR

2016

THERMOELECTRIC PROPERTIES OF NOVEL MICROSTRUCTURALLY MODIFIED $CoSb_3$ SKUTTERUDITE MATERIALS BY MINOR DOPANTS OF Mn, Hf, Al, Bi AND Yb

MOHAMED HAMID ELSHEIKH YOUSEF

THESIS SUBMITTED IN FULFILLMENT OF THE REQUIREMENTS FOR THE DEGREE OF DOCTOR OF PHILOSOPHY

FACULTY OF ENGINEERING
UNIVERSITY OF MALAYA
KUALA LUMPUR

2016

UNIVERSITY OF MALAYA

ORIGINAL LITERARY WORK DECLARATION

Name of Candidate: **Mohamed Hamid Elsheikh Yousef**

Registration/Matric No: **KHA120028**

Name of Degree: **Ph.D**

Title of Project Paper/Research Report/Dissertation/Thesis ("this Work"):

Thermoelectric Properties of Novel Microstructurally Modified $Cosb_3$ Skutterudite Materials by Minor Dopants of Mn, Hf, Al, Bi and Yb

Field of Study: **Energy**

I do solemnly and sincerely declare that:

(1) I am the sole author/writer of this Work;
(2) This Work is original;
(3) Any use of any work in which copyright exists was done by way of fair dealing and for permitted purposes and any excerpt or extract from, or reference to or reproduction of any copyright work has been disclosed expressly and sufficiently and the title of the Work and its authorship have been acknowledged in this Work;
(4) I do not have any actual knowledge nor do I ought reasonably to know that the making of this work constitutes an infringement of any copyright work;
(5) I hereby assign all and every rights in the copyright to this Work to the University of Malaya ("UM"), who henceforth shall be owner of the copyright in this Work and that any reproduction or use in any form or by any means whatsoever is prohibited without the written consent of UM having been first had and obtained;
(6) I am fully aware that if in the course of making this Work I have infringed any copyright whether intentionally or otherwise, I may be subject to legal action or any other action as may be determined by UM.

Candidate's Signature Date:

Subscribed and solemnly declared before,

Witness's Signature Date:

Name:

Designation:

ABSTRACT

A key challenge in thermoelectrics research is obtaining materials with high electrical conductivity, a high Seebeck coefficient and low thermal conductivity. The essence of the phonon-glass electron-crystal (PGEC) concept is to synthesize ultimate thermoelectric materials that can conduct electricity like a crystal but insulate heat like a glass. In this respect, the skutterudite system is a promising material that utilizes the PGEC concept. The skutterudite system relies on a crystal "cage-like" structure with a rattler atom to allow simultaneous high electrical conductivity and low thermal conductivity.

In this work, the skutterudite compound was modified by adding Mn, Hf and Al_x (x = 0.3, 0.6 and 2) to the binary skutterudite $CoSb_3$ and Al_x (x = 0.1, 0.2 and 0.3), $Bi_{0.1}$ and $Al_{0.1}Bi_{0.05}$ to the ternary skutterudite $Yb_{0.25}Co_4Sb_{12}$. The fabrication method utilized the mechanical alloying (MA) technique followed by the spark plasma sintering (SPS) process.

The addition of Mn, Hf, and Al_x to the binary skutterudite $CoSb_3$ resulted in the formation of a polycrystalline skutterudite phase with Mn, Hf, and Al located in the grain boundaries. Moreover, the addition of Mn and Al led to an increase in the area fraction of the grain boundary compared with the addition of Hf, leading to an overall modification of the skutterudite microstructure. The addition of Mn, Hf, and Al had a significant effect on the lattice thermal conductivity of $CoSb_3$, which was reduced by up to ~60% by the addition of Hf. However, the tradeoff for the microstructural modification of binary skutterudite is the relatively high electrical resistivity, thus resulting in moderate figures of merit (ZTs < 0.1). Therefore, grain boundary modification is an effective strategy to decrease thermal conductivity for this case.

A similar strategy for microstructural modification to introduce element-rich boundary regions was demonstrated to be effective for the addition of Al_x, $Bi_{0.1}$ and $Al_{0.1}Bi_{0.05}$ to $Yb_{0.25}Co_4Sb_{12}$ ternary skutterudite. Al- and Bi-rich regions were found to exist at the nano-scale along the grain boundaries. An overall improvement in all three parameters was found in comparison to undoped $CoSb_3$. A figure of merit ZT value of more than unity (ZT = 1.36) was found using this strategy. Thus, this work is useful in deriving a pathway for improvement in thermoelectrics through microstructural modification.

An introductory investigation of n- to p-type inversion of the skutterudite thermoelectric material was demonstrated through the formulation of bulk skutterudite $Al_{0.3}Co_4Sb_{12}$. A wide range of Seebeck coefficient values from -251 µV/K at low temperature to +153 µV/K at high temperature with a critical point at 200 °C is reported. This formulation serves as the starting point for new fundamental investigations of the p- to n-type inversion phenomena in thermoelectrics. In addition, this finding indicates the potential of this material as a temperature switch.

ABSTRAK

Cabaran utama dalam termoelektrik ialah mendapatkan bahan yang mempunyai konduktiviti elektrik yang tinggi, pekali Seebeck yang tinggi, dan konduktiviti haba yang rendah. Inti pati konsep fonon-glass electron-kristal (PGEC) adalah untuk sintesis bahan termoelektrik terunggul yang mampu mengalirkan elektrik seperti kristal tetapi menebat haba seperti kaca. Dalam perkara ini, sistem skutterudit merupakan bahan harapan yang menggunakan konsep PGEC. Sistem skutterudit bergantung kepada struktur "sangkar" kristal yang mempunyai atom bergetar untuk membenarkan konduktiviti elektrikal yang tinggi dan haba yang rendah secara serentak.

Dalam kerja ini, pengubahsuaian kompaun skutterudit dengan tambahan Mn, Hf, dan Al_x (x= 2, 0.6 dan 0.3) kepada skutterudit binari $CoSb_3$, dan juga Al_x (x = 0.1, 0.2 & 0.3), $Bi_{0.1}$ dan $Al_{0.1}Bi_{0.05}$ kepada skutterudit ternari $Yb_{0.25}Co_4Sb_{12}$ telah dijalankan. Kaedah fabrikasi yang digunakan ialah teknik pengaloian mekanikal (MA) diikuti dengan proses pensinteran cetusan plasma (SPS).

Penambahan Mn, Hf, dan Alx ke dalam skutterudit binari $CoSb_3$ menghasilkan bentuk fasa skutterudit polihablur dengan kehadiran Mn, Hf, dan Al yang banyak di sempadan bijian. Di samping itu, penambahan Mn dan Al menyebabkan peningkatan luas pecahan sempadan bijian apabila dibandingkan dengan penambahan Hf, menyebabkan pengubahsuaian keseluruhan kepada mikrostruktur skutterudit. Secara nyata, penambahan Mn, Hf, dan Al memberi kesan ketara kepada kekisi konduktiviti haba $CoSb_3$ yang mana dikurangkan sehingga ~60% dengan tambahan Hf. Walaubagaimanapun, trade-off pengubahsuaian mikrostruktur skutterudit binari ialah rintangan elektrikal yang agak tinggi, justeru mengakibatkan angka merit sederhana (ZTs< 0.1). Oleh itu, pengubahsuaian sempadan bijian telah ditunjukkan sebagai strategi efektif untuk mengurangkan konduktiviti haba dalam kes ini.

Strategi yang sama dalam pengubahsuaian mikrostruktur untuk memperkenalkan kawasan sempadan yang kaya elemen telah dibuktikan efektif dalam kes penambahan Al_x, $Bi_{0.1}$ dan $Al_{0.1}Bi_{0.05}$ ke dalam $Yb_{0.25}Co_4Sb_{12}$ skutterudit ternari. Kawasan yang kaya dengan Al dan Bi dijumpai berada di skala-nano di sepanjang sempadan bijian. Penambahbaikan menyeluruh dalam semua tiga parameter didapati apabila dibandingkan $CoSb_3$ ysang tidak didop. Nilai Angka merit ZT lebih daripada kesatuan (ZT = 1.36) telah didapati melalui strategi ini. Oleh itu, kerja ini berguna untuk menerbitkan laluan untuk penambahbaikan dalam termoelektrik melalui pengubahsuaian mikrostruktur.

Penyiasatan pengenalan kepada penyongsangan jenis-n kepada jenis-p untuk bahan termoelektrik skutterudit telah dijalankan melalui formulasi skutterudit pukal $Al_{0.3}Co_4Sb_{12}$. Julat pekali Seebeck besar dari -251 µV/K di suhu rendah ke +153 µV/K di sushu tinggi dengan titik genting di 200 °C telah dilaporkan. Formulasi skutterudit ini berguna sebagai titik mula untuk penyiasatan asas mengenai fenomena penyongsangan jenis-p dan –n dalam termoelektrik. Tambahan lagi, penemuan ini menandakan potensi bahan ini sebagai suis suhu.

ACKNOWLEDGEMENTS

First and foremost, I would like to acknowledge the invaluable sacrifice of my dear wife, Raghda, and my beloved son, Abdulrahman. My research has stolen the time that should have been theirs. I wish to express my heartfelt gratitude for their support, understanding, and encouragement. I also would like to thank my parents for their constant love, encouragement, and moral support throughout all of my life.

I express my sincere gratitude and appreciation to my respectful supervisor Associate Prof. Dr. Mohd Faizul Mohd Sabri for his invaluable advice and supervision throughout this research. He is a very wonderful person. I deeply appreciate all that he did for me. I would like to thank Prof. Dr. Masjuki Bin Haji Hassan for his time serving on my supervising committee and for providing me with valuable suggestions and recommendations. I also need to especially thank Dr. Suhana Binti Mohd Said for taking so much time to help me with my research and for providing me with valuable suggestions and recommendations "***Thank you so much for all the encouragement and support you gave to me. Thank you for all the smart advices that are the reason for my success***". My deep thanks to Miyazaki Sensei for giving me the opportunity to join his laboratory for a period of time at Tohuku University, Japan, and for making my research more valuable by his contribution. I extend thanks to Dr. Dhafer Abdulameer, Mr. Mohamed Bashir, Mr. Shuma Naito, Dr. Bui Duc Long and Associate Prof. Dr. Norbani Binti Abdullah for all of their insightful discussions on thermoelectric materials and many other topics in general.

Last but not least, I would like to thank all of my lab members and the technical staff for their support and encouragement during the entire journey to completing this degree.

TABLE OF CONTENTS

LIST OF FIGURES

LIST OF TABLES

LIST OF SYMBOLS AND ABBREVIATIONS

TE	:	Thermoelectric
Z	:	Thermoelectric figure of merit
ZT	:	Dimensionless thermoelectric figure of merit
α	:	Seebeck coefficient
σ	:	Electrical conductivity
T	:	Temperature
K	:	Thermal conductivity
PF	:	Power factor
ΔV	:	Voltage difference
ΔT	:	Temperature difference
EMF	:	Electromotive force
K_e	:	Electrons and holes transporting heat
K_L	:	Phonons travelling through the lattice
L	:	Lorenz number
K_B	:	Boltzmann constant
e	:	Electron charge
PGEC	:	phonon-glass electron-crystal
ρ	:	Electrical resistivity
HH	:	Half-Heusler
TNTs	:	Titanate nanotubes
PANI	:	Polyaniline
PTH	:	Polythiophene
PEDOT:PSS	:	Poly (3, 4-ethylenedioxythiophene): poly (styrenesulfonate)

PA	:	Polyacetylene
PPY	:	Polypyrrole
PC	:	Polycarbazoles
PPV	:	Polyphenylenevinylene
HMS	:	Higher manganese silicides
E_c	:	Conduction band
E_v	:	Valence band
E_f	:	Fermi level
E_g	:	Band gap
n	:	Carrier density
h	:	Planck's constant
m^*	:	Effective mass of the charge carrier
C	:	Integration constant
υ	:	Directional velocity component
j	:	Current density
E	:	Applied electric field
μ	:	Charge-carrier mobility
l_e	:	Electron mean free path
l_p	:	Phonon mean free path
ρ_m	:	Mass density
υ_s	:	Velocity of sound in the crystal
c	:	Specific heat of the crystal
m_e	:	Electron mass
TSO	:	Transparent semiconducting oxide
SPS	:	Spark plasma sintering
RSPs	:	Rapid solidification processes

H	:	Hardness
LAST	:	Lead-antimony-silver-tellurium
B	:	Bulk moduli
G	:	Shear moduli
E	:	Young's moduli
υ	:	Poisson ratios
α	:	Thermal expansion coefficient
CTE	:	Coefficient of thermal expansion
T_m	:	Melting temperature
HPT	:	High pressure torsion
TEGs	:	Thermoelectric generators
TECs	:	Thermoelectric coolers
COP	:	Coefficient of performance
MCC	:	Microclimate cooling
MS	:	Melt spinning
TEACs	:	Thermoelectric air conditioners
η_{te}	:	Energy-conversion efficiency
T_h	:	Hot-side temperature
T_c	:	Cold-side temperature
QW	:	Quantum-well
SUV	:	Sports utility vehicle
CNG	:	Compressed-natural-gas-fueled engine generator set
STEGs	:	Solar thermoelectric generators
SHP-TE	:	Glass evacuated-tube heat-pipe solar collectors
HSTE	:	Hybrid solar thermoelectric
HGS	:	Hybrid-generation-system

IR	:	Infrared
TMS	:	Thermoelectric microfluidic sensor
DI	:	Injecting deionized
RTGs	:	Radioisotope thermoelectric generators
GPHS	:	General-purpose heat-source
LES	:	Lincoln Experimental Satellite
MHW	:	Multi-hundred watt
JPL	:	Jet Propulsion Laboratory
ARPSs	:	Advanced Radioisotope Power Systems
CTMs	:	Cascaded thermoelectric modules
RPSs	:	Radioisotope power systems
MA	:	Mechanically alloying
XRD	:	X-ray Diffraction
SEM	:	Scanning electron microscope
EDX	:	Energy-dispersive X-ray spectroscopy
FIB	:	Focused ion beam
TEM	:	Transmission electron microscope
XPS	:	X-ray Photoelectron Spectroscopy
ESCA	:	Electron Spectroscopy for Chemical Analysis
I	:	Current
D	:	Thermal diffusivity
C_p	:	Specific heat
ρ_d	:	Density
T	:	Thickness
STA	:	Simultaneous Thermal Analysis
DSC	:	Differential scanning calorimetry

TG	:	Thermogravimetry
HV	:	Vickers hardness
F	:	Force
d	:	Average length
μ_H	:	Hall mobility
LS	:	Low spin
HS	:	High Spin
HT-XRD	:	High temperature - X-ray Diffraction
SCO	:	Spin crossover

CHAPTER 1: INTRODUCTION

1.1 Background

The search for cleaner, more sustainable energy sources is an ever-growing global concern because of escalating energy costs and global warming associated with fossil fuel sources (Afshar et al., 2012; Kalkan et al., 2012; Omer, 2008; Thirugnanasambandam et al., 2010; Xi et al., 2007). Among the viable technologies for this purpose, thermoelectric (TE) energy converters are of increasing interest because these solid-state devices can transform heat given off from sources such as power plants, factories, motor vehicles, computers or even human bodies into electric power using the Seebeck effect (Fthenakis & Kim, 2010; Liu et al., 2010; Martín-González et al., 2013; Saidur et al., 2012; Shu et al., 2013; Vélez et al., 2012; Wang et al., 2011). The many advantages of this energy-conversion phenomenon include solid-state operation, the absence of toxic residuals, vast scalability, maintenance-free operation vis-à-vis the lack of moving parts or chemical reactions, and a long life span of reliable operation (Dai et al., 2011; Riffat & Ma, 2003; Tie & Tan, 2013; Ullah et al., 2013). Conversely, solid-state thermoelectric devices can also change electrical energy into thermal energy for cooling or heating using the Peltier effect. Compared to traditional refrigeration and heating mechanisms, solid-state thermoelectric energy converters have the advantage of simplicity; they produce no vibrations and are highly scalable. Furthermore, because TE devices use no refrigerants or working fluids, they may be expected to produce negligible direct emissions of greenhouse gases over their lifetimes (Tsubota et al., 2008). However, because of their low efficiency, current TE materials have found limited commercial application. A brief perusal of the possibilities is illustrated in Figure 1.1, where the different scales of energy generation that are represented are relevant to different applications (Pichanusakorn & Bandaru, 2010). The problem remains that the efficiency of today's thermoelectric material is inadequate to compete with conventional power generation and refrigeration

(Gao et al., 2006). Moreover, the growing need for alternative power sources is driving a growing interest in developing a new generation of thermoelectric materials. In order to become commercially competitive, novel thermoelectric materials will need to increase in efficiency by a factor of three over the present values (Zhan et al., 2006).

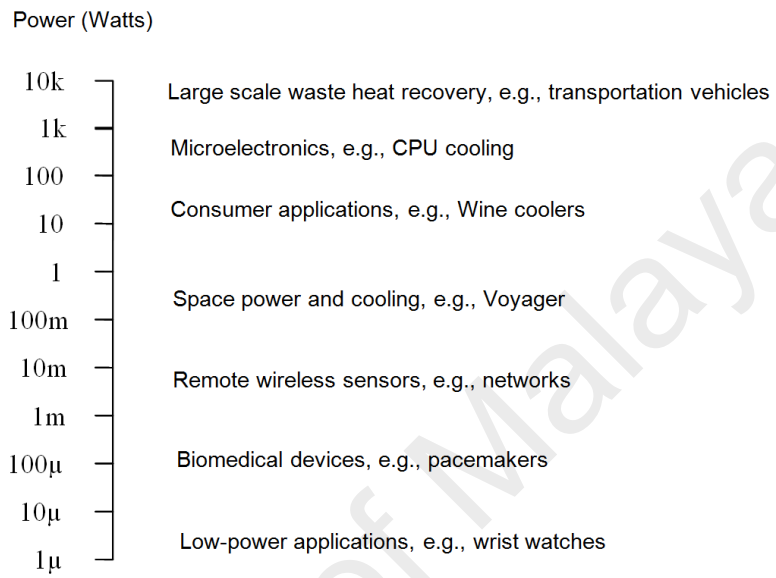

Figure 1.1: Thermoelectric materials can be put to use in various energy conversion applications, encompassing ten orders of magnitude in power, as illustrated above (Pichanusakorn & Bandaru, 2010).

1.2 Thermoelectric phenomena

Thermoelectric devices can convert thermal energy from a temperature gradient into electrical energy. This phenomenon was discovered in 1821 and is called the ‘‘Seebeck effect,’’ while the reverse counterpart of this phenomenon was discovered by Peltier in 1834 (Riffat & Ma, 2003). As knowledge of thermoelectrics increased, the most important discoveries were related to material properties. In 1911, Altenkirch derived the thermoelectric efficiency, now known simply as Z, or the thermoelectric figure of merit. The thermoelectric efficiency can be non-dimensionalized by multiplying by the absolute temperature T, which yields the most common form of thermoelectric efficiency, ZT, also known as the dimensionless figure of merit. This value is given as

$$ZT = \alpha^2 \sigma \frac{T}{K} \qquad 1\text{-}1$$

where α is the Seebeck coefficient, σ is the electrical conductivity, and K is the thermal conductivity. These three transport parameters α, σ and K depend upon one another as a function of the band structure, carrier concentration and many other factors that are discussed later in this paper; Figure 1.2 illustrates the three main parameters, including the carrier concentration (Snyder & Toberer, 2008). In particular, α and σ generally vary in a reciprocal manner, making any improvement in the figure of merit Z difficult (Cai et al., 2004). In addition, the electrical conductivity and the Seebeck coefficient are inversely related, so it is not generally possible to increase the thermoelectric power factor ($PF = \alpha^2\sigma$) above a particular optimal value for a bulk material (Zide et al., 2006). However, ideal thermoelectric materials would have a high electrical conductivity to allow the conduction of electricity, which would create a potential difference across the sample, and a low thermal conductivity to maintain the temperature gradient between the hot and cold side (Bian & Shakouri, 2006). Early work in thermoelectrics resulted in very small values of Z because the materials being used (mostly metals) did not possess ideal thermoelectric properties; i.e., metals possess both high electrical conductivity and high thermal conductivity. Most traditional materials exhibit a correlation between electrical and thermal conductivity. A material that conducts electricity well, such as a metal, also conducts heat well, and a material that insulates heat, such as glass or ceramic, also insulates electricity (Snyder & Toberer, 2008).

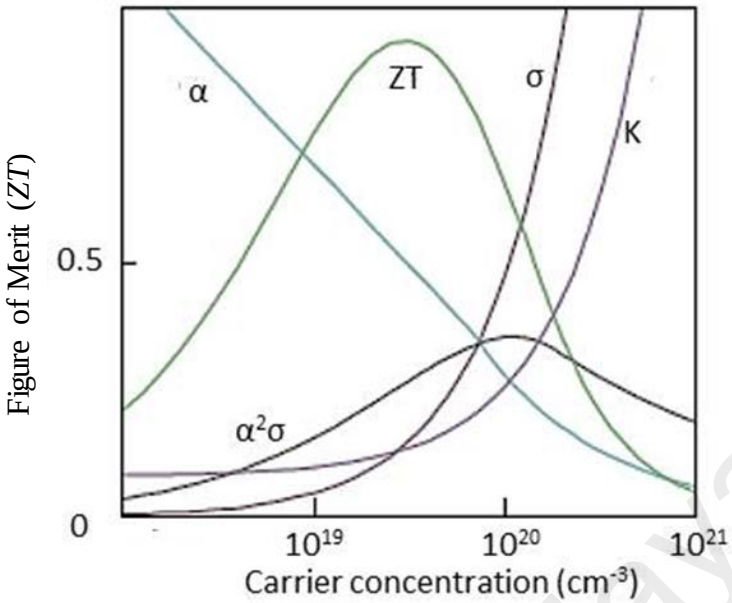

Figure 1.2: Maximizing the efficiency (ZT) of a thermoelectric involves a compromise of thermal conductivity (k; plotted on the y axis from 0 to a top value of 10 W m^{-1} K^{-1}) and Seebeck coefficient (S or α; 0 to 500 μV K^{-1}) with electrical conductivity (σ; 0 to 5,000 $\Omega^{-1}cm^{-1}$) (Snyder & Toberer, 2008).

Many years of effort to increase *ZT* have not yet led to a fundamental breakthrough. In fact, the history of thermoelectric materials can be characterized by the progress in increasing *ZT*, as shown in Figure 1.3 (Zheng, 2008). Thus, for devices operating at room temperature ($T \approx 300$ K), traditional thermoelectric materials, such as bismuth telluride (Bi_2Te_3) and lead telluride (PbTe), possess values of $ZT \approx 1$ (Hochbaum et al., 2008). In recent years, work by Venkatasubramanian and his colleagues (Venkatasubramanian et al., 2001) and Harman et al. (Harman et al., 2002) using superlattices and quantum dots based on these materials has increased their room room-temperature *ZT* to ~2–2.4. These improvements in performance are primarily the result of a reduction in lattice thermal conductivity, and the thermoelectric power factor (*PF*) is largely unchanged. For practical purposes, a suitable high-performance TE material should have a *ZT* of > 4, and the achievement of this goal has remained a formidable challenge (Gao et al., 2006). However, commercial materials are available with $ZT \approx 1$.

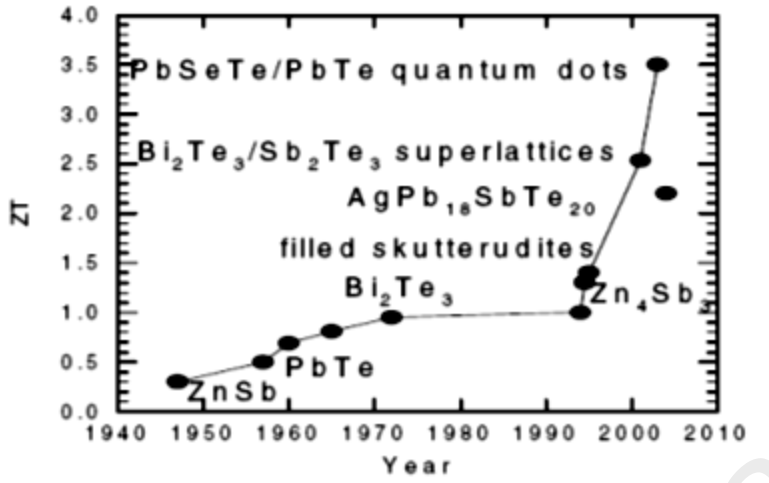

Figure 1.3: ZT of many typical thermoelectric materials as a function of year (Zheng, 2008).

1.3 Problem statement

To modulate high-performance the thermoelectric skutterudite material $CoSb_3$ with dopants, a lengthy synthetic process is required. The current state of the art for skutterudites in thermoelectrics usually consists of two pathways: a) a simple fabrication process (mechanically alloying + hot pressing) achieves a relatively low figure of merit (ZT = 0.78) (Liu et al., 2011) , whereas b) the state-of-the-art processing (induction melting + long-term high-temperature annealing + cold pressing + long-term high-temperature annealing + ball milling + spark plasma sintering) achieves a higher figure of merit (ZT =1.7) (Shi et al., 2011). Furthermore, some of the effective dopants, such as lanthanide elements, are costly. Thus, the scope of this work was to explore a high-performance skutterudite formulation using relatively simple fabrication methods.

1.4 Research objectives

For this thesis, the following objectives were defined to address the problem statement framed above:

1. To formulate new thermoelectric materials by incorporating Mn, Hf, and Al into $CoSb_3$ binary skutterudite and Al and Bi into $Yb_{0.25}Co_4Sb_{12}$ ternary skutterudite thermoelectric materials.
2. To fabricate high-performance skutterudite thermoelectric materials through a simple synthesis process of mechanical alloying and spark plasma sintering.
3. To characterize the microstructural, thermoelectric, charge transport, and mechanical properties and the thermal stability of the developed skutterudite materials.
4. To provide a physical framework for achieving improved ZT in $CoSb_3$ skutterudites.

1.5 Organization of the dissertation

- The purpose of this study is presented in Chapter 1.
- Chapter 2 presents the background and literature review relevant to this study. The literature review primarily focuses on the parameters that affect the performance of thermoelectric materials and the thermoelectric applications.
- Chapter 3 describes the methodology and experimental study by explaining the steps of fabrication and testing.
- Chapter 4 deeply discusses the effect of minor doping on the skutterudite thermoelectric material formulation in terms of microstructure, thermoelectric properties, electronic properties, thermal stability and mechanical properties.
- General conclusions and potential future research are presented in Chapter 5.

CHAPTER 2: LITERATURE REVIEW

2.1 Thermoelectric properties

2.1.1 The Seebeck coefficient

A temperature difference between two points in a conductor or semiconductor results in a voltage difference between these two points. Stated differently, a temperature gradient in a conductor or semiconductor gives rise to a built-in electric field. This phenomenon is called the Seebeck effect or the thermoelectric effect (Sootsman et al., 2009). The Seebeck coefficient gauges the magnitude of this effect. The thermoelectric voltage developed per unit temperature difference in a conductor is called the Seebeck coefficient or thermopower ($\alpha = \Delta V/\Delta T$). Only the net Seebeck voltage difference between different metals can be measured (Zheng, 2008). In fact, it is via the Seebeck effect that thermoelectric devices can act as electrical power generators (Nolas et al., 1999). A schematic diagram of a simple solid-state thermoelectric refrigerator or power generator operating based on the Seebeck effect is shown in Figure 2.1.

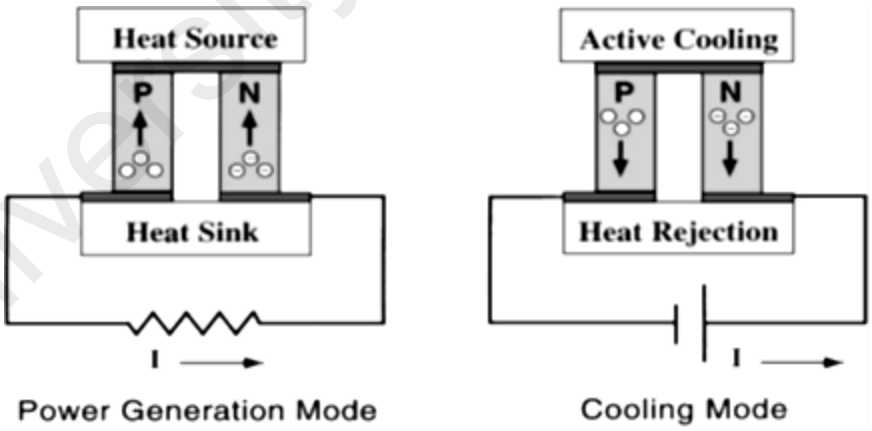

Figure 2.1: A thermoelectric modules illustrating the versatility of these materials for use in solid-state thermoelectric refrigeration or in power generation. The thermoelectric module is composed of an n-type and a p-type semiconducting material connected electrically in series through metallic electrical contact pads and thermally in parallel between ceramic ends (Nolas et al., 1999)

The Seebeck coefficient is expressed in units of V/K (or, more commonly, μV/K or μV/°C). It has been found that only a combination of two different materials, a so-called

thermocouple, exhibits the Seebeck effect. For two leads of the same material, no Seebeck effect manifests, although both leads intrinsically possess a Seebeck coefficient, for reasons of symmetry. It is, however, present because the Seebeck effect is a bulk property and does not depend on either the specific arrangement of the leads or the material or the specific method of joining them (Van Herwaarden & Sarro, 1986). Metals have different thermoelectric sensitivities, or Seebeck coefficients. For example, iron has a Seebeck coefficient of 19 μV/°C at 0°C, which means that for every 1°C difference in temperature, a positive thermoelectric electromotive force (EMF) or (Seebeck voltage) of 19 μV is induced in iron at temperatures near 0°C. A negative thermoelectric electromotive force (EMF) can also be induced in a metal, so Seebeck coefficients can also have negative values. For example, constantan (a copper-nickel alloy) has a Seebeck coefficient of -35 μV/°C at 0°C. Generally, most metals possess Seebeck coefficients of 10 μV/K or less, but semiconductor materials are promising for the construction of thermocouples because they have Seebeck coefficients in excess of 100 μV/K. It should be noted that the relation between the Seebeck voltage and the temperature is linear only for small changes in temperature (Nolas et al., 1999). For larger temperature ranges, the relationship becomes non-linear. It is therefore important to state the temperature at which the Seebeck coefficient is being specified. However, thermopower ≥ 225 is required to achieve $ZT > 2$ (Tritt & Subramanian, 2006).

Recently, the interfacial thermoelectric effect has been generalized to include spin transport phenomena. The spin Seebeck effect refers to the generation of a spin voltage caused by a temperature gradient in a ferromagnet, which enables the thermal injection of spin currents from the ferromagnet into an attached nonmagnetic metal over a macroscopic scale of several millimeters. The main feature of the spin Seebeck device is that the output power is proportional to the length perpendicular to the temperature gradient. In addition, the paths of the heat current and charge current are separated in the

spin Seebeck device in dissimilarity to the charge Seebeck device (Adachi et al., 2013). Therefore, the spin Seebeck device could be a new trajectory to enhance the thermoelectric efficiency.

2.1.2 Thermal conductivity

A high-quality thermoelectric material must have a high electrical conductivity, a high thermopower, and a low thermal conductivity. Because the first two are determined only by the electronic properties of the material, they are often combined into the quantity $PF = \alpha^2\sigma$, referred to as the `power factor.' In contrast, the thermal conductivity $K = K_e + K_L$ in thermoelectrics is the sum of two contributions: (1) electrons and holes transporting heat (K_e) and (2) phonons travelling through the lattice (K_L) (Gonçalves et al., 2010). It then follows that the thermoelectric figure of merit can be maximized by maximizing the electrical conductivity and minimizing the thermal conductivity. However, there is a relation between the two: the Wiedemann-Franz law for electrons that obey degenerate and non-degenerate statistics (K_B is the Boltzmann constant, and e is the electron charge).

$$\frac{K_e}{\sigma} = \mathrm{L}_\circ \mathrm{T} \qquad 2\text{-}1$$

$$\mathrm{L}_\circ = \left(\frac{\pi^2}{3}\right)\left(\frac{K_B}{e}\right)^2 = 2.44 \times 10^{-8}\left(\frac{K^2}{V^2}\right) \qquad 2\text{-}2$$

And

$$\mathrm{L}_\circ = 2\left(\frac{K_B}{e}\right)^2 = 1.48 \times 10^{-8}\left(\frac{K^2}{V^2}\right) \qquad 2\text{-}3$$

Increasing the electrical conductivity not only produces an increase in the electronic thermal conductivity but also usually decreases the thermopower; optimizing ZT thus turns out to be a challenge. While the power factor can in some cases be increased by varying the concentration of charge carriers in the material, decreasing K and K_L is much

more problematic, especially for K_L, which is determined by the structure, rigidity, atomic masses, and other characteristics of the lattice (Dmitriev & Zvyagin, 2010). Because the ZT values of the presently available materials are too low for cost-effective applications, various efforts have been made to improve them. The idea of reducing the K_L of a compound by substituting the crystal lattice with an amorphous (glass-like) structure has been suggested, and the phonon-glass electron-crystal (PGEC) concept, which was first introduced by Slack and discussed in detail in a review by Nolas et al. (1999) and has become a general guideline for the development new thermoelectric materials, is at the heart of the investigation into the skutterudite material system for thermoelectric applications. A PGEC material would possess electronic properties similar to those normally associated with a good semiconductor single crystal but would have thermal properties akin to those of an amorphous material.

It is believed that the ideal thermoelectric material would have regions of its structure composed of a high-mobility semiconductor, which provides the electron-crystal electronic structure, interwoven with a phonon glass. The phonon-glass region would be ideal for hosting dopants and disordered structures without disrupting the carrier mobility in the electron-crystal region (Wan et al., 2010). The thermal conductivity of a semiconductor material is related to its position in the periodic table, i.e., for a larger mean atomic weight, the thermal conductivity is lower. This behavior has been attributed to the increase in density causing the velocity of sound in the crystal to decrease, leading to a subsequent decrease in thermal conductivity (Bulusu & Walker, 2008).

The most widely used commercial thermoelectric material is bulk Bi_2Te_3 and its alloys with Sb, Se, and so on, which exhibit $ZT \approx 1$. It is difficult to scale bulk Bi_2Te_3 to large-scale energy conversion, but fabricating synthetic nanostructures for this purpose is even more difficult and expensive. Conversely, the most common semiconductor, Si, is abundant and widely used in the electronics industry, and a large industrial infrastructure

exists for the low-cost and high-yield processing of Si. Bulk Si, however, has a high K (~150 Wm^{-1} K^{-1} at room temperature), yielding $ZT \approx 0.01$ at 300 K (Ma et al., 2008). Increasing ZT via the reduction of K, by reducing the lattice contribution to the thermal conductivity, is a powerful concept. The most important factors that can aid in accomplishing this are (i) the use of compounds with complex crystal structures, (ii) the presence of heavy atoms weakly bonded to the structures, (iii) the existence of inclusions and/or impurities, (iv) the formation of solid solutions and (v) the existence of a large number of grain boundaries (Gonçalves et al., 2012).

The introduction of nanostructure has also become a potential tool for reducing K and consequently increasing ZT. This concept has revolutionized the field of TE because, the utilization of nanostructures has led to the achievement of ZT values of approximately 1-2 compared to < 1 for bulk materials. The Nanostructured $Bi_xSb_{2-x}Te_3$ have been shown to exhibit significantly improved $ZT \approx 1.4$ at 100 °C, mostly because of the reduced K_L (Ma et al., 2008). However, it is difficult to scale up these superlattices for large-volume energy-conversion applications because of limitations in both heat transfer and cost. Joshi et al. (Joshi et al., 2008) investigated the enhanced thermoelectric figure of merit in nanostructured p-type silicon germanium bulk alloys and found that this ZT enhancement is most likely attributable to the increased phonon scattering at the grain boundaries and crystal defects formed by lattice distortion, with some contribution from the increased electron power factor at high temperatures.

2.1.3 Electrical resistivity (ρ)

Electrical resistivity is an important material-dependent property that is usually a function of temperature. The value of ρ at room temperature is indicative of whether a material is an insulator an insulator (ρ is on the order of 10^6 Ω.m or more) or a metal (ρ is on the order of 10^{-6} Ω-m or less). In the latter case, if the lattice were perfect, the electron

would travel infinitely through it, and the material would only exhibit finite conductivity because of the thermal motion of the lattice and the effect of impurities (Bulusu & Walker, 2008). The resistivity of a semiconductor material falls between the metal and insulator regimes. It has been found that the optimum range of electrical resistivity for a thermoelectric material is from 10^{-3} to 10^{-2} Ω-m (Cadoff & Miller, 1960). Variations in the electrical resistivity of a semiconductor depend on changes in the carrier concentration and the mean free path of the charge carriers. The charge carriers are reflected/scattered by the surface of the material when they reach it (Das & Ganesan, 1998). To achieve low electrical resistivity in semiconductors, the lattice should have nearly infinite conductance at low temperatures, but in reality, the conductivity of semiconductors is very low at low temperatures because of the limited number of free electrons (Bulusu & Walker, 2008). Moreover, the analysis of the temperature dependence of the electrical resistivity in intermetallic compounds is a powerful tool for obtaining information regarding the intrinsic properties of these materials. Depending on the temperature range considered, one can draw certain conclusions regarding the scattering of electrons on the thermal excitations of the lattice (Kowalczyk et al., 2008).

2.2 Categories of TE materials

Thermoelectric materials comprise a huge family, including various materials from semimetals and semiconductors to ceramics, containing various crystalline forms from monocrystals and polycrystals to nanocomposites and covering varying dimensions from bulk, films and wires to clusters. Recently, certain polymers have also been shown to exhibit interesting thermoelectric material properties.

2.2.1 Metal-based thermoelectrics

The history of applications of thermoelectric materials is strongly associated with their efficiency. The earliest application of the thermoelectric effect was in metal

thermocouples, which have been used to measure temperature and radiant energy for many years (Zheng, 2008). However, metals possess very high electrical conductivity and very high thermal conductivity. Several TE materials containing heavy metals such as Bi, Sb, Pb and Te have been developed so far; these materials are mostly toxic and unstable at high temperatures (~1000 K) (Wang et al., 2008). Therefore, metal oxides that exhibit good TE performance are in high demand because metal oxides are environmentally friendly and essentially stable at high temperatures (Wang et al., 2008). (Watanabe et al., 2012) measured the temperature dependence of the electrical resistivity and the thermoelectric power of $(Ni_{1-x}M_x)Mn_2O_4$ (M = Zn and Mg, x = 0, 0.1 and 0.2), and they reported that the activation energy for electrical conduction is increased above a certain temperature (~450 °C). In the low-temperature region, the absolute value of the thermoelectric power is increased by Mg substitution, and the thermoelectric powers of all samples are found to change sign from negative to positive as the temperature increases.

To obtain phonon-glass electron-crystal PGEC materials, the idea of a complex structure, which imagines a material with distinct regions that each provide different functions, has been advanced (Wan et al., 2010). Two relatively new material classes are widely regarded as PGEC materials, namely, the clathrates and the filled skutterudites. Clathrates are periodic solids in which tetrahedrally coordinated atoms form cages that surround a metal atom (Iversen et al., 2000). Clathrate I materials have the general formula A_8E_{46}, with A = Na, K, or Ba and E = Al, Ga, In, Si, Ge, or Sn. Clathrates II and III have idealized formulas of $A_{24}E_{136}$ and $A_{30}E_{172}$, respectively, and exist with the same A and E elements; see Figure 2.2 (Kleinke, 2010). The low thermal conductivities for semiconducting clathrates are attributed to resonant scattering of the acoustic heat-carrying phonons by the guest atoms. The localized low-frequency vibration mode of the guest atoms is expected to cut through the acoustic branches, which decreases the number

of acoustic phonon modes and effectively limits the heat transport (Christensen et al., 2006), i.e., the enhanced vibration of the guest atoms A causes a flattening of the phonons bands, lowering the velocity of the phonons, which significantly contributes to the low thermal conductivity of these materials (Kleinke, 2010). However, a few studies have investigated clathrate structures, and all have reported $ZT < 1$ (Anno et al., 2012).

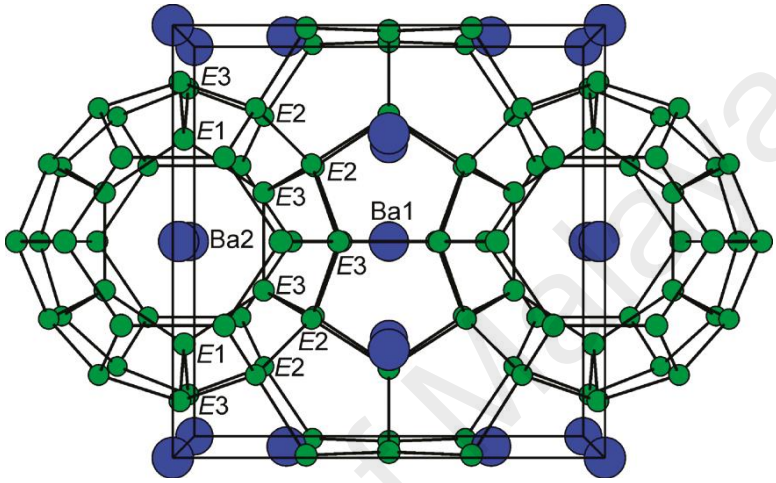

Figure 2.2: Crystal structure of cubic $Ba_8Ga_{16}Si_{30}$. All three E sites are mixed occupied by Ga and Si (Kleinke, 2010).

The essence of the PGEC concept is to synthesize semiconducting compounds in which one of the atoms is weakly bonded in an oversized atomic cage. In this sense, the skutterudite system is a promising material for thermoelectric applications (Kim et al., 2003). The basic family of binary semiconducting compounds has been widely investigated (Mi et al., 2006; Yang et al., 2010); a skutterudite structure generally has the form MX_3, where M is the transition metal element, Co, Rh, or Ir, and X is the pnictogen element, such as P, As, or Sb. Examples of skutterudite structures are CoP_3, $CoAs_3$, $CoSb_3$, RhP_3, $RhAs_3$, $RhSb_3$, IrP_3, $IrAs_3$ and $IrSb_3$ (Nolas et al., 1999).

For several years, efforts have focused on the preparation and characterization of ternary skutterudites that are isoelectronic to the binary skutterudites (Vaqueiro et al.,

2006). Ternary skutterudites can be obtained either by substitution at the anion site, X, by a pair of elements from groups IV and V (e.g., $CoSb_{3-y}Sn_y$) (Kim et al., 2007) or by isoelectronic substitution at the cation site, M, by a pair of elements from subgroup VIII (e.g., $Fe_xCo_{4-x}Sb_{12}$) (Ur et al., 2007). Binary skutterudites are known for their high electron mobilities and favorable Seebeck coefficients but, unfortunately, have large values of lattice thermal conductivity. However, up to date the highest Figure of merit *ZT* of 0.15 for high purity $CoSb_3$ nanostructured TE material at 650 K was achieved by Khan et al. (2014).

Filling the voids with elements that are loosely bond and thus able to ''rattle,'' thereby providing a phonon-scattering mechanism in the skutterudite structure, provides a possible solution to this obstacle (Alboni et al., 2007). Filling the interstitial voids in the structure with foreign atoms, especially alkaline-earth atoms (Matsuoka et al., 2006; Kwan-Ho Park & Kim, 2010), rare earth atoms (Alleno et al., 2006; Kim et al., 2004; Rogl et al., 2011; Sklad et al., 2010) and other ions (Grytsiv et al., 2003; Jung et al., 2008), is an effective method of reducing the thermal conductivity while maintaining the electrical conductivity and the Seebeck coefficient of $CoSb_3$-based skutterudites (Lu et al., 2010). Many such efforts toward filling skutterudites have been reported: (i) partially filled skutterudite (e.g., $La_{0.1}Co_4Sb_{12}$) (Liu et al., 2006), (ii) filled skutterudite (e.g., $CeFe_4Sb_{12}$) (Ravot et al., 2001), (iii) double-filled skutterudite (e.g., $Ba_xCe_yCo_4Sb_{12}$) (Bai et al., 2009) and (iv) multiple-filled skutterudite (e.g., $Yb_{0.2}Ce_{0.15}In_{0.2}Co_4Sb_{12}$) (Ballikaya et al., 2012). Meanwhile, filling the core of the cage-like framework, as shown in Figure 2.3, via doping (Chakoumakos & Sales, 2006) can also serve to reduce the thermal conductivity (Deng et al., 2011). The substitution of antimony by Se and Te can influence the electronic structure and electrical properties of the material; in particular, such substitution leads to a substantial change in the carrier masses and enhanced scattering of phonons on impurities (Wojciechowski et al., 2003). Generally, n-type $CoSb_3$ is prepared

by substituting Fe, Ni, Pd or Pt into Co sites, which enhances the mass fluctuation scattering (Kitagawa et al., 2005; Peng et al., 2004), thereby significantly reducing the lattice thermal conductivity from its original value. However, investigations of filled skutterudite as a promising candidate for power-generation applications in the temperature range of 500–800 K (Yu et al., 2013) have led to observations of large *ZT* values for many n-type filled skutterudites, such as 1.3 at 800 K for $Ba_{0.08}Yb_{0.14}Eu_{0.10}Co_4Sb_{12}$ (Shi et al., 2009) and 1.7 at 850 K for $Ba_{0.08}La_{0.05}Yb_{0.04}Co_4Sb_{12}$ (Shi et al., 2011). .

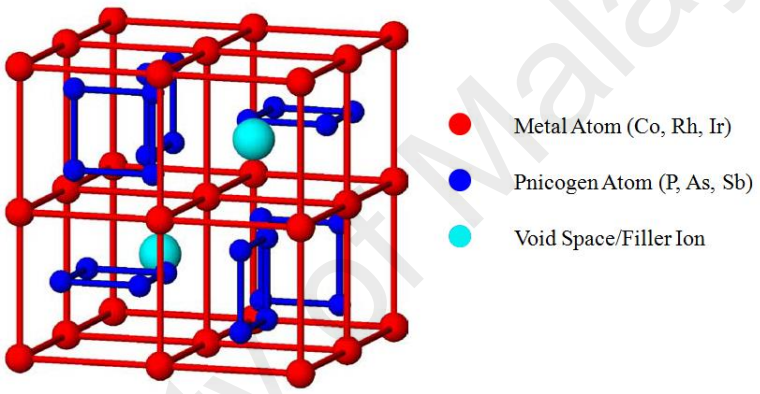

Figure 2.3: Crystal structure of filled skutterudite (Chakoumakos & Sales, 2006).

Among the numerous TE materials, half-Heusler (HH) alloys have attracted considerable attention because of their appealing electrical transport properties and their relatively high Seebeck coefficients in addition to their rich elemental combinations (Zou et al., 2013). These alloys have three components that may originate from different elemental groups or may be a combination of elements in the same group. Two of the groups are composed of transition metals, and the third group consists of metals and metalloids. The chemical formula of half-Heusler alloys is XYZ, where X, Y, and Z can be selected from many different elemental groups (for example, X = Ti, Zr, Hf, V, Mn, or Nb; Y = Fe, Co, Ni, or Pt; Z=Sn or Sb). The crystal structures of the ternary

intermetallic compounds usually are of the cubic MgAgAs type (space group F-43m) (Wang et al., 2010). Figure 2.4 shows the crystal structure of half-Heusler compounds XYZ (Kawaharada et al., 2004). These compounds have a narrow band gap on the order of 0.1–0.2 eV at the Fermi level and have garnered interest because of their potential as thermoelectric materials (Shutoh & Sakurada, 2005). Their associated large effective masses lead to several characteristics, including large thermoelectric power factors, large Seebeck coefficients (250 μVK^{-1}) at room temperature, moderate electrical resistivity (1–10 $\mu\Omega m$) and high thermal conductivity (~10 $Wm^{-1}K^{-1}$) at room temperature (Lee & Chao, 2010). MNiSn and MCoSb (M = Ti, Zr, Hf) compounds are of great interest among the half-Heusler family because of their good thermoelectric properties. The state-of-the-art *ZT* values of MNiSn (M = Ti, Zr, Hf) compounds are close to unity (Fu et al., 2013). However, most efforts thus far have concentrated on the optimization of the thermoelectric performance of n-type half-Heusler alloys. The search for promising p-type half-Heusler materials that can be coupled to existing high-performance n-type half-Heusler alloys for high-temperature thermoelectric power generation has only been initiated in the past decade (Maji et al., 2010).

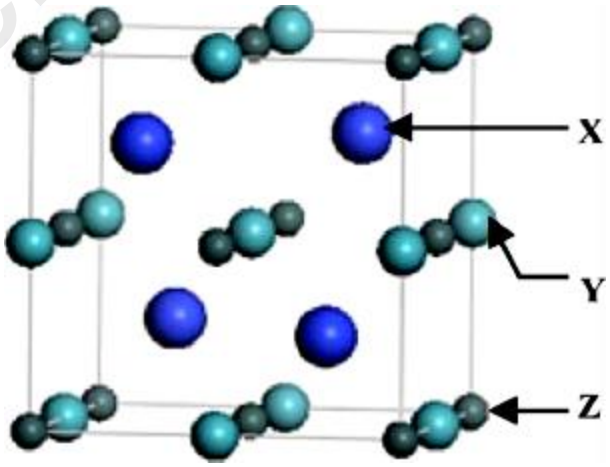

Figure 2.4: Crystal structure of the half-Heusler type compounds (Kawaharada et al., 2004).

Typically, other metals have been used as dopants. β-Zn_4Sb_3 has a hexagonal rhombohedric crystal structure, space group R3C with 66 atoms per unit cell. With its complex structure low thermal conductivity values can be expected (Zhu et al., 2000). The low-temperature structural phase transitions of Bi-, Pb-, In- and Sn-doped samples of thermoelectric Zn_4Sb_3 have been characterized on crystals grown from molten metal fluxes by Nylén et al. (2007), and they observed that when preparing β-Zn_4Sb_3 in the presence of metals with low melting points (Bi, Sn, In, and Pb), the additional metal atoms are unavoidably incorporated in small concentrations (0.04–1.3 *wt*%), act as dopants and alter the subtle balance between Zn disorder and Zn deficiency in Zn_4Sb_3, which has dramatic consequences for its low-temperature structural behavior.

In general, metals with poor conductivity are good candidates for providing enhanced values of thermoelectric power. It might be important to consider that most metallic materials contain inclusions, which can be either metallic or non-metallic. Inherent to the elaboration process, they are distributed inside the materials. These inclusions in alloys reduce their mechanical strength and resilience, are detrimental to surface finish and increase porosity, and they have a tendency to increase corrosion (Carreon, 2013). Furthermore, they act as stress enhancers and can cause the premature failure of in-service components.

2.2.2 Ceramics

Over the past two decades, from the discovery of the first ceramic thermoelectric material, many efforts have been put forth to obtain high-performance thermoelectric materials for application in energy-conversion systems (Ferreira et al., 2012). To date, the doped alloy TE materials based on Bi_2Te_3 are the best-known ones, and they exhibit $ZT \approx 1$ at room temperature. However, because they are easily oxidized and vaporized, these TE alloy materials cannot be used for applications at high temperatures in air (Liu et al.,

2012). Therefore, oxide TE materials are used instead at high temperatures and in oxygen. Thermoelectric oxide materials have drawn much attention because of their good thermal stability at high temperatures and their low toxicity compared to conventional intermetallic alloys (Wang et al., 2010). However, research seeking efficient thermoelectric materials often involves no conventional semiconductors. In this sense, oxide compounds such as $NaCo_2O_4$, $LaCoO_3$, $(ZnO)_mIn_2O_3$, $BaSnO_3$, $BaPbO_3$, $Ca_3Co_4O_9$, $Sr_{1-x}Nd_xTiO_3$ and $Bi_2Ca_2Co_2O_x$ are promising candidates for thermoelectric materials because of their transport properties and their physical and chemical stability (Constantinescu et al., 2013; Kenfaui et al., 2010; Li & Li, 2011; Liu et al., 2010; Tajima et al., 2001; Wang et al., 2012; Yasukawa & Kono, 2006; Yasukawa et al., 2010).

The addition of titanate nanotubes (TNTs) (2 vol%) fabricated via the pressureless sintering method has been found to enhance the *ZT* value of Nb-doped $SrTiO_3$ polycrystalline ceramic to approximately 0.14 at 900 K (Wang et al., 2010). $(Ca_{1-x}Sr_x)_3Co_4O_9$ polycrystalline has been fabricated by using spark plasma sintering method to substitute Ca by Sr, and the result demonstrated that the figure of merit *ZT* achieves 0.22 at 1000K for the composition $(Ca_{0.995}Sr_{0.005})_3Co_4O_9$ (Delorme et al., 2011). However, the fabrication of modules based on oxide materials has only recently begun to emerge, and there exist very few reports concerning the performance of these materials (Noudem et al., 2008). The oxide nature of the thermoelectric elements and the processing specifications, which involve very high temperatures, make the fabrication a difficult task and different from that of conventional thermoelectric modules (Noudem et al., 2008).

2.2.3 Polymers

Among the various categories of thermoelectric materials, a great deal of attention has recently been paid to organic TE materials, particularly since the discovery of conducting polymers (Tsai et al., 2011). In this regard, polymers are very attractive because they are

light, flexible, and suitable for room-temperature applications and because they generally require relatively simple manufacturing processes (i.e., spin coating and inkjet printing) compared to semiconductor-based thermoelectrics. Polymers are intrinsically poor thermal conductors, which makes them ideal for use as thermoelectrics, but their low electrical conductivity, Seebeck coefficient, and stability have hampered their use in thermoelectric applications (Choi et al., 2011). However, compared to inorganic TE materials, organic or polymer TE materials exhibit several inherent advantages, such as potentially low cost because of the abundance of carbon resources, simple synthesis in general, abundant electron-energy bands through modulation, simple processing into versatile forms, high energy density, and low *k*, which may be of great importance for their potential TE applications.

The physical and chemical properties of certain polymers are tunable within a fairly large range of modifications of their molecular structures (Yue & Xu, 2012). The ionic conducting polymers, such as poly(3,4-ethylenedi-oxythiophene):poly(styrenesulfonate) (PEDOT:PSS), which possess high electrical conductivity and intrinsically low thermal conductivity, are considered to be the most promising novel organic TE materials (Tsai et al., 2011). In a two-component nanocomposite, the selection of a conducting polymer and an inorganic thermoelectric material may yield high thermoelectric power and high electrical conductivity of the material. Because these properties are dependent on the particle size and morphology, it is interesting to map the relation between the structural and electrical properties of the material.

Recently, various researchers have attempted to prepare nanocomposites/hybrids/heterostructures of inorganic thermoelectrics with conducting polymers (Chatterjee et al., 2009). Table 2.1 summarizes the electrical conductivity σ, Seebeck coefficient α, thermal conductivity k and power factor *PF* as well as the highest

ZT value of a few typical polymer and polymer-inorganic TE nanocomposites. Du et al. (Du et al., 2012) reviewed the research progress concerning conducting polymers and their corresponding TE nanocomposites, and their primary focus was TE nanocomposites based on conducting polymers such as polyaniline (PANI), polythiophene (PTH), and poly (3, 4-ethylenedioxythiophene): poly (styrenesulfonate) (PEDOT:PSS), as well as other polymers such as polyacetylene (PA), polypyrrole (PPY), polycarbazoles (PC) and polyphenylenevinylene (PPV); these materials appear to have great potential for producing relatively low-cost and high-performance TE materials, and the authors reported that in polymer and polymer-inorganic TE nanocomposites, the value of the Seebeck coefficient typically ranges from −4088 to 1283 μV/K, the electrical conductivity ranges from 10^{-7} to 10^{4} S/cm, and the thermal conductivity ranges from 0.02 to 1.2 W/mK. However, it has been demonstrated that the transport properties of conducting polymers are greatly influenced by the process of doping with various materials.

Table 2.1: The electrical conductivity σ, Seebeck coefficient α, thermal conductivity k and power factor PF as well as the highest ZT value of a few typical polymer and polymer-inorganic TE nanocomposites.

Materials	σ (S/cm)	α (μV/K)	K (W/mk). Maximum PF (μW/mK^2) or ZT
PANI	~10^{-7}-320	~ -16-225	K, ~ 0.02-0.542 ZT_{max}, 1.1×10^{-2} at 423K
PANI-inorganic TE nanocomposites	0-140	~ -30-626	κ,0.25-1.2
PTH	~10^{-2}-10^{3}	~ 10-100	K, 0.028-0.17 , ZT_{max}, 2.9×10^{-2} at 250K
PTH -inorganic TE nanocomposites	7.1-8.3	-56-1283	PF_{max}, 2.5×10^{-2}
PEDOT:PSS	0.06-945	8-888	K, 0.34 , ZT_{max}, 1.0×10^{-2} at 300K
PEDOT-Tos	6×10^{-4}-300	40-780	K, 0.37, ZT_{max}, 0.25 at RT
PEDOT:PSS-inorganic TE inorganic nanocomposites	0-400	~ -125-167	K,0.22 , ZT_{max}, 0.10 at RT
PPY	0-340	-1-40	K, 0.2, ZT_{max}, 3×10^{-2} at 423 K
PA	~1.53×10^{-3}-2.85×10^{-4}	~ 0.5-1077	
PC	~4.0×10^{-5}-5×10^{2}	4.9-600	PF_{max}, 1.9
PMeOPV	46.3	39.1	PF_{max}, 7.1
P(ROPV-co-PV)(RO-MeO,EtO and BuO)	183.5-354.6	21.3-47.3	K, 0.25-0.80 (estimated) , ZT_{max}, 9.87×10^{-2} at 313 K
Others polymer-inorganic TE nanocomposites (polymer/carbon nanotube with different contents of CNT	~0-48	~ 40-50	K, 0.18-0.34, ZT_{max}, 0.006 at RT

(Du et al., 2012)

2.2.4 Semiconductors

Since the late 1950s, research concerning semiconducting thermoelectric devices has been applied for terrestrial cooling and power generation and later for space power generation because of their competitive energy conversion compared to other types of small-scale electric power generators (Zhang et al., 2009). Semiconductor thermoelectric power generation, which is based on the Seebeck effect, has very interesting capabilities with respect to conventional power-generation systems (Chen et al., 2005). During the 1990s, there was a heightened interest in the field of thermoelectrics driven by the need for more efficient materials for electronic refrigeration and power generation. Because of the use of semiconductor materials for thermoelectric applications, there has been a considerable effort to improve the figures of merit (*ZT*) of these materials to greater than 3 to make them commercially viable. Semiconductor materials are promising for the construction of thermocouples because they have Seebeck coefficients in excess of 100 μVK^{-1} (Dughaish, 2005), and the only way to reduce *K* without affecting α and σ in bulk materials, thereby increasing *ZT*, is to use semiconductors of high atomic weight, such as Bi_2Te_3 and its alloys with Sb, Sn, and Pb. A high atomic weight reduces the speed of sound in the material and thereby decreases the thermal conductivity (Majumdar, 2004). A solid-state or semiconductor electronics component, for example, can perform well and reliably for many years when it is operating at or near the ambient temperature (Alam & Ramakrishna, 2013). Intermetallic compounds such as Mg_2X (X = Si, Ge, Sn) and their solid solutions are semiconductors with the antifluorite structure and have been proposed as good candidates for high-performance thermoelectric materials because of their superior features such as large Seebeck coefficients, low electrical resistivities, and low thermal conductivities (Tani & Kido, 2005). For example, higher manganese silicides (HMS) are proven to be promising candidates as p-type thermoelectric material in the

temperature range of 400–700 K (Saleemi et al., 2015). However, the best-*ZT* materials are found to be heavily doped, small-band-gap semiconductors.

2.3 Fabrication process of the skutterudite TE materials

The best results of mechanical processing of skutterudites involve multiple steps, which can be generalized as follows:

- Melting the powder or/and the shots using arc furnace,
- Formation of ingots using the molten material above,
- Grinding of the ingots into fine powder,
- Loading of the powder into quartz ampoules,
- Sealing of the ampoules and heating in a furnace to 1473 K at 5 K/min,
- Maintain at 1473 K for 1 h,
- Cooling to 1073 K at 5 K/min,
- And, finally annealing at 1073 K for 50 h or more (Kawaharada et al., 2001).

Examples of high performing filled skutterudites have shown a high Figure of merit ($ZT \geq 0.9$) when prepared using the process described above. The addition of filler atoms have served to act as rattler atoms which consequently reduce the thermal conductivity and consequently improve the figure of merit. A composition of $Eu_{0.27}Co_4Sb_{12}$ were synthesized by melting method and sintered by spark plasma sintering technique has shown a maximal value of 0.9 at 850 K (Pei et al., 2008).

Mallik et al. (2009) have shown that utilizing the above and including nano-inclusions have further enhanced the ZT value. For example, a maximum ZT value of 0.96 was achieved for $In_{0.4}Co_4Sb_{12}$ with InSb nano-inclusions by using vacuum induction melting and long annealing process. These results indicate that a small amount of secondary

phases in the skutterudite system will not prevent high TE performance. In addition, it may increase the phonon scattering hence decrease the thermal conductivity.

The multi-filling approach was then exploited by other workers to further improve the Figure of Merit. For example, The Yb atom is one of the most effective species among the lanthanide atoms for filling the skutterudite voids due to their large atomic mass, radius and it is intermediate valence state. Yb-filled skutterudite has been optimized with different combinations of Ce and In by Ballikaya et al. (2012) have achieve high values of ZT. The highest ZT value of 1.43 was achieved for $Yb_{0.2}Ce_{0.15}In_{0.2}Co_4Sb_{12}$ triple-filled skutterudite at 800 K containing nanoinclusions of Yb_2O_3 and Sb. The process which enabled this high Figure of Merit was melting–annealing followed by spark plasma sintering to prepare the samples.

On the other hand, the fast fabrication process such as mechanical alloying followed by hot pressing or spark plasma sintering has always shown a ZT < 0.9. Starting from elemental powder mixtures of $La_xCo_4Sb_{12}$ were prepared via mechanical alloying (MA) and spark plasma sintering (SPS) by Liu et al. (2006) and the maximum ZT value was 0.3425 when x = 0.9 at 500 °C. To enhance the thermoelectric performance of fast prepared element the addition of nono-inclusions in the lattice system would be a good approach, which is the central theme explored in this thesis. The composition of $Yb_{0.2}Co_4Sb_{12}$ with PbTe inclusions has shown a higher ZT value of 0.78 at 700 K when prepared by the ball-milling and hot-pressing process (Liu et al., 2011). This is the record ZT achieved using fast fabrication process, prior to the work discussed in this thesis. Therefore, the short time of fabrication process needs extra effort in term of the microstructure modification to overcome the low ZT of < 1.

2.4 Governing parameters for thermoelectric material selection: Intrinsic material properties

2.4.1 Energy gap and band structure in semiconductors

In a solid, electrons exist at energy levels that combine to form energy bands. A simplified energy-band diagram is shown in Figure 2.5. The top band is called the conduction band E_c, and the next lower one is called the valence band E_v. The Fermi level E_f (the hypothetical level of potential energy for an electron inside a crystalline solid and a term used to describe the highest of the collection of electron energy levels at a temperature of absolute zero) in intrinsic semiconductors lies essentially halfway between the valence and conduction bands. The region between the valence band and the conduction band is called the forbidden band, where, ideally, no electrons exist (Ozpineci & Tolbert, 2003). For a conductor such as copper, no forbidden band exists, and the energy bands overlap. For an insulator, conversely, this band is so wide that the electrons require a great deal of energy to move from the valence band to the conduction band. For semiconductors, the gap of the forbidden band is smaller than for an insulator. If the electrons in the valence band are excited externally, they can move to the conduction band. In the valence band, they have an energy of E_v. To move to the conduction band, they require an amount of energy $E_g = E_c - E_v$, where E_g is the band gap (Ozpineci & Tolbert, 2003).

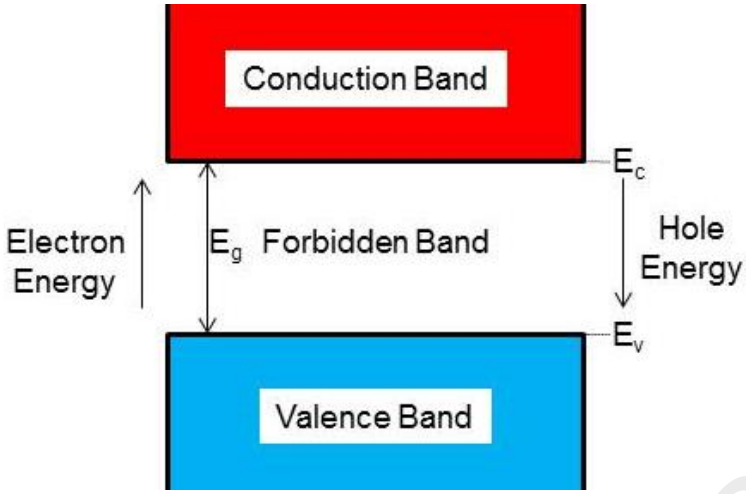

Figure 2.5: A simplified energy band diagram of a semiconductor (Ozpineci & Tolbert, 2003).

Since 1954, the control of the energy gap via the effect of the carrier concentration has become one of the methods of greatest interest for controlling the properties of semiconductors. This phenomenon, however, has also been used to analyze the degree of impurity in semiconductor crystals (Omar & Gorges, 2006). A great improvement of electrical properties is closely related to the narrowing of the band gap, though precipitated impurity phases can influence the measured band-gap value (Gao et al., 2012) . Table 2.2 lists some semiconducting elements and compounds alongside their band gaps at 300 K (Hummel, 2011). Because electrical transport properties are closely related to the electronic states near the highest valence band and the lowest conduction band for some compounds, it is reasonable to focus on the energy bands near the Fermi level. The band-gap energy is expected to decrease as the atomic number of the constituent atoms increases. The atomic potential spreads more and more as the atomic number increases. This spreading should cause a lowering of the band-gap energy according to two theories that describe these energy bands: the free-electron theory and the tight-binding approximation theory (Nag, 1995).

The Fourier coefficient for the periodic potential should decrease as the overlapping of the atomic potentials increases, and therefore, the band-gap energy should decrease, according to the free-electron theory. However, increasing overlap should cause a larger coupling between neighboring atoms and a broadening of the allowed band, consequently leading to a narrowing of the forbidden band or a decrease of the band-gap energy (Zhang et al., 2011). When the dispersion of the top valence bands fluctuates within a small energy region, these relatively heavy bands with large effective mass contribute to a high thermopower. For materials with simple band structures, the absolute thermopower value α can be described as follows:

$$\alpha = C\left(\frac{K_B}{e}\right)\frac{\ln(\pi m K_B T)^{\frac{3}{2}}}{nh^3} \qquad 2\text{-}4$$

where α is the thermopower, K_B is the Boltzmann constant, e is the elementary charge, n is the carrier density, h is Planck's constant, m^* is the effective mass of the charge carrier, C is an integration constant, and T is the absolute temperature (Zhang et al., 2011). Ramdas et al. (Ramdas et al., 2005) investigated the electronic band gaps of semiconductors as influenced by their isotopic composition, and they reported that isotopically controlled crystals offer an extraordinary opportunity to test theoretical predictions using a variety of spectroscopic techniques.

Table 2.2: List of some semiconducting elements and compounds together with their bandgaps at 300 K.

	Material	**Direct / Indirect Bandgap**	**Band Gap Energy at 300 K (eV)**
Elements	C (diamond)	Indirect	5.47
	Ge	Indirect	0.66
	Si	Indirect	1.12
	Sn	Direct	0.08
Groups III-V compounds	GaAs	Direct	1.42
	InAs	Direct	0.36
	InSb	Direct	0.17
	GaP	Indirect	2.26
	GaN	Direct	3.36
	InN	Direct	0.70
Groups III-V compounds	α-SiC	Indirect	2.99
	ZnO	Direct	3.35
	CdSe	Direct	1.70
	ZnS	Direct	3.68

(Hummel, 2011)

2.4.2 Charge carrier concentration

An effective adjustment in the carrier concentration dominates the electronic transport behavior by exerting a significant effect on both the electrical conductivity and the Seebeck coefficient (Tan et al., 2012). Furthermore, all thermoelectric properties depend closely on the carrier concentration and typical thermoelectric materials exhibit an optimum carrier concentration of $10^{19} - 10^{21}$ per cm^3 (Wang et al., 2011). One of the technologically simplest (and therefore virtually universally used) methods of improving

the thermoelectric properties of a semiconductor material is to choose the optimum level of doping, where `optimum' is used in the sense of maximizing the thermoelectric figure of merit. As mentioned above, an optimum electron concentration exists because, as the concentration increases, the conductivity usually increases, accompanied by a simultaneous decrease in the thermopower (Dmitriev & Zvyagin, 2010). Delaizir et al. (2012) investigated the p-type alloys $Bi_{1\_x}Sb_xTe_3$ with $0.9 \leq x \leq 1.7$, and they observed a linear relation between the amount of antimony, x, and the charge-carrier concentration. The thermoelectric properties and non-stoichiometry of GaGeTe have been studied by Drasar et al. (2012), and the authors reported that the measurement of the transport parameters qualitatively indicated that both $Ga_{1+x}Ge_{1\_x}Te$ and $GaGeTe_{1-y}$ are p-type semiconductors ($n \approx 10^{19}$ cm^{-3}). Their hole concentration generally rises with increasing x and y, as demonstrated by the experiment. However, the negative Seebeck coefficient indicates that the transport processes are dominated by electrons as carriers (Roudebush et al., 2011). Thus, the Seebeck coefficient, the electrical conductivity, and the thermal conductivity vary systematically with the carrier concentration (Anno et al., 2012).

2.4.3 Mobility

In the presence of several scattering mechanisms, theoretical calculation of the resultant mobility of the charge carriers becomes rather complicated. Until now, no thorough analysis of the validity limits of the common theoretical approaches and adopted models has been performed (Mikhnovich Jr., 2001). Electronic transport is described by the (local) electric-field-induced directional velocity component, υ, of the mobile charge carriers (superimposed on their random thermal motion as a time and ensemble average of a fast sequence of acceleration and scattering events), which is associated with a current density $j=e.n.\upsilon$, where e is the electric unit charge, and n is the local charge-carrier density. The latter can be altered, in principle, by doping, injection, or photo-generation (Karl, 2003). The relation between υ and the applied electric field E is usually linear for

moderate field strengths (reflecting Ohm's law), $\upsilon = \mu \times E$ and it is obvious that μ, the charge-carrier mobility, is the fundamental (intrinsic) electronic-transport quantity that is specific to a given semiconductor material (Karl, 2003). Because the mobility of electrons serves as a direct relation between the crystal structure and the electrical conductivity, the ratio of the mobility μ to the thermal conductivity K is a function of the mean atomic weight. Thus, using the relation for mobility in semiconductors and the Pierls relation for thermal conductivity, we can calculate the ratio as a function of the electron mean free path l_e and the phonon mean free path l_p in a crystal (Bulusu & Walker, 2008).

$$\left(\frac{\mu}{K}\right) = \frac{(4e\rho_m l_e)}{c v_s (2\pi m_e K_B T)^{\frac{1}{2}} l_p} \qquad 02\text{-}5$$

Here, ρ_m is the mass density; υ_s the velocity of sound in the crystal; c is the specific heat of the crystal; and m_e and e are the electron mass and charge, respectively. Using material properties that have been measured for some common semiconductors, the above ratio is plotted against the mean atomic weights of these semiconductors in Figure 2.6.

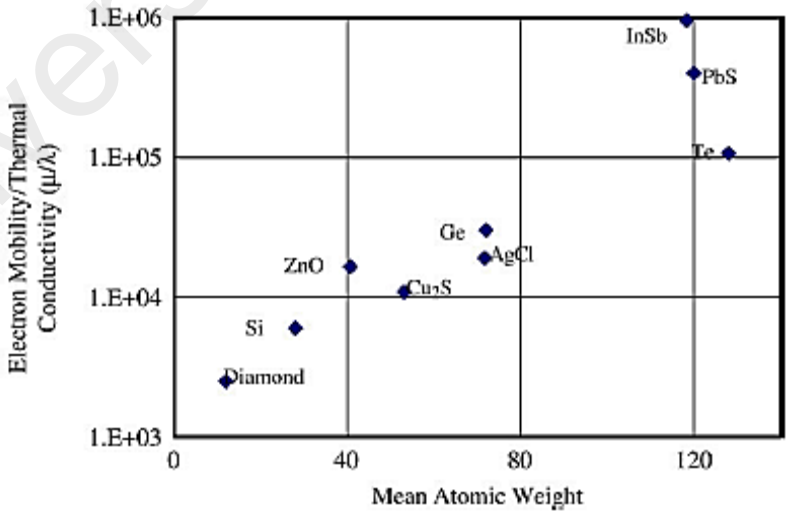

Figure 2.6: Ratio of electron mobility to thermal conductivity of thermoelectric materials (Bulusu & Walker, 2008).

2.5 Auxiliary properties

2.5.1 Diffusion properties

Diffusion is the movement of particles from regions of high concentration to regions of low concentration. Diffusion in semiconductors is of great importance for semiconductor technology. As the dimensions of circuits shrink, an understanding of the atom-scale mechanisms of the diffusion processes will become crucial to accurately model and design future devices (Uberuaga et al., 2002). In pure (undoped or unalloyed) compounds, the effects of diffusion are not apparent at temperatures below that at which the compound begins to dissociate (Cadoff & Miller, 1960). Once a small amount of dissociation has taken place, however, the products may diffuse at differing rates in the temperature gradients present in the device, and the diffusion of an intentionally added impurity may exhibit similar behavior, as shown in Figure 2.7. Self-diffusion in binary compound semiconductors is more complex than in elemental semiconductors because of the larger number of possible native point defects that can, in principle, mediate self-diffusion. In addition to vacancies and self-interstitials on the corresponding sublattices, antisite defects must be considered (Bracht et al., 2005). Homogeneities in thermoelectric materials are affected by the temperature gradient because the optimal properties can only be obtained within a very narrow temperature region for each homogeneous material, which greatly limits the efficient utilization of many dispersed energy sources (Cui et al., 2002). However, the diffusion effect depends on the band-gap width and the ratio of electron conductivity to hole conductivity. Heavy carrier doping effectively suppresses the diffusion effect, i.e., it inhibits the increase of thermal conductivity at high temperatures.

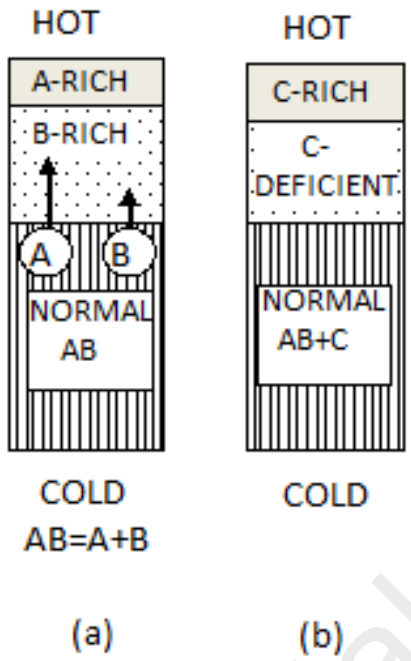

Figure 2.7: Effects of diffusion. (a) Unequal rates of diffusion of dissociation products of compound AB results in inhomogeneity. (b) Greater solubility of doping agent C in AB leads to concentration of C at hot end. In both cases, temperature at cold end is insufficient to produce disproportionation (Cadoff & Miller, 1960).

There have been a number of efforts to characterize defect structures by studying defect-structure-sensitive properties, such as impurity diffusion (Nakagawa et al., 2005), and many of these efforts have successfully determined diffusion coefficients in semiconductor materials and have also quantitatively analyzed the diffusion process and predicted the results of annealing. Wanwan et al. (2006) studied the effect of Cd-diffusion annealing on the electrical properties of CdZnTe and reported that the crystal's resistivity is affected by annealing, which limits diffusion. The nature of this treatment is a diffusion process. Thus, it is meaningful to relate the change in resistivity to the diffusion parameters. The undesirable diffusion of thermoelectric materials when placed in a thermal gradient will result in non-homogeneous and inferior materials, and the importance of diffusion processes is evident at temperatures of approximately 80 percent to 90 percent of the absolute melting point of the materials. A micro-thermoelectric device

consists of a bonding layer, electrodes and thermoelectric thin films. At the interfaces between the metallic electrodes, solder materials and thermoelectric thin films in a micro-thermoelectric device, diffusion occurs and degrades the performance and reliability of the device. Thus, a Ni layer is used as the diffusion barrier in some commercial devices that use bulk thermoelectric materials (Bae et al., 2011). However, because of undesirable and unpredictable diffusion phenomena, modern process technologies try to reduce diffusion by decreasing the thermal range experienced by the device during operation.

2.5.2 Oxidizability

For want of a better term, the tendency of the composition of a thermoelectric material to become altered when exposed to the oxygen in the air may be called "oxidizability." As is well known, oxygen is a reactive gas. When oxygen is introduced during deposition, highly energetic atomic ions ejected from the target may react with the oxygen ions via collisions and transform into oxides on the target surface. As the oxygen partial pressure increases, the collision probability between the reactive gas and the atomic ions increases, causing the sputtering and deposition rates to decline (Xu et al., 2012). The results of this undesirable phenomenon take two: in one type, a thin surface layer of oxidized material is formed, and the deposition process is inhibited by its formation; the other form involves the diffusion of oxygen into the interior of the material and is therefore progressive (Cadoff & Miller, 1960). Thus far, oxides have been regarded as unsuitable for thermoelectric applications because of their poor mobility, but some years ago, Terasaki (2003) found that a single crystal of the layered cobalt oxide $NaCo_2O_4$ exhibits high thermoelectric performance.

Recently, several electrically conductive oxide systems have been recognized as potential candidates for thermoelectric materials; these thermoelectric oxides can be used at high temperatures with no deterioration of their performance caused by oxidation, and

their production costs are comparatively low. Ito and Furumoto (2008); Zhou et al. (2011) investigated the effects of the annealing atmosphere on thermoelectric signals from ZnO films, and they suggested that ambient oxygen plays an important role in the electronic properties of ZnO films. P-type transparent semiconducting oxide (TSO) materials, Cu_2O is one of the most promising candidates, and because of the effect of the oxygen flow rate during deposition on the properties of Cu_2O films, the oxygen flow rate must be kept low to avoid the over-oxidation of Cu_2O to CuO and to ensure a non-oxidized/non-poisoned metallic copper target in the reactive sputtering environment. The proper control of the amount and flow rate of oxygen during deposition can produce good-quality p-type transparent Cu_2O films with electrical resistivities ranging from 10^2 to 10^4 Ω-cm, hole mobilities of 1–10 cm^2/V-s, and optical band gaps of 2.0–2.6 eV (Li et al., 2011). The synthesis and post-annealing effects on the transport properties of thermoelectric oxide $(ZnO)_mIn_2O_3$ ceramics have been studied by Wang et al. (2012), and they inferred that the oxygen defects or vacancies in the InO_2 layers play an important role on both the electrical and thermal transport properties of these $(ZnO)_mIn_2O_3$ ceramics. It has also been reported that the resistivity, carrier concentration, and Hall mobility of Z_5IO films depend strongly on the annealing temperature and ambient atmosphere. Measurements of the Seebeck coefficient and electrical resistivity are most likely among the most sensitive means for the detection of small amounts of diffusive oxidation (Cadoff & Miller, 1960). However, in some of the most-studied compounds, traces of diffusive oxidation that are visually and chemically undetectable can so severely affect the Seebeck coefficient as to change its sign, and the resistivity can be increased by several decades as a result of this process.

2.5.3 Brittleness

At low temperatures (T < 200 K), single crystals of the Bi–Sb alloys exhibit the best thermoelectric performances, but the brittleness of the single crystals is a problem in

practical devices. To ameliorate this limitation, some efforts have been devoted to studying the influence of the growth parameters on the mechanical properties of such alloys (Liu et al., 2007). However, the requirements for producing nanostructured TE materials are two-fold: improve their mechanical properties (reduce brittleness and improve machining) and improve their TE properties (figure of merit) (Prokhorov & Pivovarov, 2011). Moon et al. (2010) prepared p-type Te-doped Bi_2Te_3–Sb_2Te_3 compounds using rapid solidification and spark plasma sintering (SPS) techniques, and they reported that the solidified powders consisted of homogeneous thermoelectric phase and that as the SPS temperature increases, the microstructure becomes coarser, resulting in a reduction of the hardness. At present, rapid solidification processes (RSPs) such as gas atomization and melt spinning have been reported to offer a novel opportunity for modifying the intrinsic brittleness and thermoelectric anisotropy of Bi–Te-based thermoelectric materials by forming a fine-grained and homogeneous microstructure (Kim & Chun, 2007). One reason for the broad interest in hardness (H) testing is that the microstructure (and hardness) of materials can change dramatically with alloying, and the machinability of brittle materials also has been correlated with hardness. Thus, the compositional dependence of H is significant because H is related to other mechanical properties. For LAST (lead-antimony-silver-tellurium), the fabrication of thermoelectric (TE) modules for waste-heat recovery will require the machining of perhaps several hundred (or more) individual TE legs. Because machinability and wear resistance are functions of H for other brittle materials (Ren et al., 2008). Zhou et al. (2012) investigated the thermal stability and elastic properties of Mg_2X (X = Si, Ge, Sn, Pb) phases from first-principle calculations and calculated the bulk moduli B, shear moduli G, Young's moduli E and Poisson ratios υ; they reported that Mg_2Si, Mg_2Ge, Mg_2Sn and Mg_2Pb are all brittle.

2.5.4 Compression and shear strength

The average strength (the mean of the strength distribution) and Young's modulus (which characterizes the stress–strain response of a brittle material prior to fracture) are fundamental to understanding the mechanical properties of a TE material in a practical device (Fan et al., 2012). Enhancement of the mechanical strength of a TE module will render it more robust. The largest improvement must be in the shear strength, which is the weakest point of many TE modules. The compressive strength also must be increased, especially near the perimeter of the module. Such additional compressive strength will be especially useful in preventing damage to the module if, during the assembly process, clamping forces are accidentally applied unevenly to the module. Not only does the brittleness of the material limit the resistance of the device to mechanical and thermal shocks, but the cutting and fabrication of the arms themselves require that the materials used not be too brittle. Hong et al. (2003) studied the thermoelectric properties of novel n-type 95% Bi_2Te_2 5% Bi_2Se_3 alloys by gas atomizing and extrusion process, and they reported that the compressive strengths of the compounds hot extruded at 16:1 and 25:1 were 160 and 160 MPa, respectively. The figures of merit Z of the compounds extruded at 16:1 and 25:1 were 2.50 and 2.07×10^{-3} K^{-1}, respectively, because of the different grain sizes induced by the differences in deformation caused by varying the extrusion ratio. The shear strength of aged $CoSb_3$/Ti/Mo–Cu TE joints has been investigated by Zhao et al. (2009), and the results indicated the joints possessed sufficient strength after aging at 575°C for 720 h. Moreover, the $CoSb_3$/Ti/$W_{80}Cu_{20}$ elements exhibit sufficient shear strength and good electrical contact for the reliability of a thermoelectric device (Zhao et al., 2012). Experiments conducted by Zhu and Li (2010) on nanostructured materials, such as nanoparticles, nanowires, nanotubes, nanopillars, thin films, and nanocrystals, have revealed a host of ''ultra-strength" phenomena, which are defined by the stresses in a material component generally increasing to a significant fraction (>1/10) of its ideal

strength – the highest achievable stress of a defect-free crystal at zero temperature. However, while thermoelectric modules exhibit relatively high mechanical strength in the compression mode, their shear strength is comparatively low.

2.5.5 Coefficient of thermal expansion (CTE)

Thermal expansion is critical, as devices for high-temperature applications will be subjected to extreme temperature fluctuations. This property, defined as the fractional change in length or volume with a unit change in temperature, affects several aspects of the design of thermoelectric devices. Generally, the thermal expansion coefficient α ($\alpha = (\Delta L/L_0) / (T_2-T_1)$) varies inversely with the melting temperature (T_m), and it has been empirically confirmed that the product αT_m is a constant for many substances. This means that a material with high T_m should exhibit low α (D. Y. Jung et al., 2010). The CTE of TE materials is of critical importance because the shear stress is proportional to the temperature gradient, and the larger the heterogeneity in the thermal expansion coefficient of a material is, the larger is the shear stress that will result (Huang et al., 2006). Al-Merbati et al. (2013) examined the influence of device geometry on thermal stress, thermal efficiency and output power, and the result indicated that the presence of high stress can be attributed to the mismatch of thermal expansion coefficients between the pin and the hot plate, which generates high stress levels at the interface between the hot plate and the pin. With respect to the space group (in mathematics and geometry, a space group is a symmetry group, usually for three dimensions, that divides space into discrete repeatable domains), the Pnma phase exhibited a small but significant decrease in thermal expansion with increasing dopant levels, while the Imma phase exhibited no significant change in CTE with increasing dopant levels. However, these values can be considered representative of the behavior of a bulk polycrystalline sample because of the independence of the thermal expansion from microstructure and porosity (Asenath-Smith et al., 2011). Tachibana and Fang (2012) estimated the thermal stress to investigate the

reliability of thermoelectric devices by devices via temperature-cycling tests, and they claimed that it was obvious that the thermal stress was determined by the temperature difference, coefficients of thermal expansion, die height, die cross section, substrate size and so on. However, no explicit relations among these parameters were given. Rogl et al. (2012) investigated the effects of high pressure torsion (HPT) processing on the structural, thermoelectric and mechanical properties of $Sr_{0.07}Ba_{0.07}Yb_{0.07}Co_4Sb_{12}$, and they reported that the thermal expansion coefficient below room temperature after processing was slightly lower than before HPT. The thermal expansion of the sample was measured above room temperature both parallel and perpendicular to the pressing direction, and interesting results were obtained: the thermal expansion coefficient calculated for the temperature range of 600–700 K was the same as for the low-temperature region, but the expansion behavior from room temperature to 550 K differed between the first and third measurements and requires further investigation. As the temperature increased from 300 to 550 K, the length first reached a maximum and then was observed to decrease.

2.6 Applications

Thermoelectric (TE) modules comprise arrays of thermoelectric (TE) junctions, which are connected electrically in series and thermally in parallel. The TE junctions, in turn, consist of p- and n-type thermoelectric materials, which are selected from the range of materials discussed so far in this review, based primarily on their physical thermoelectric performance. Auxiliary to the basic array of TE modules are components that contribute to the overall efficiency of the module, such as heat sinks, which absorb heat from the hot side, and cooling fins or cooling systems, which dissipate heat from the cool side. Typically, a single module may produce power in the range of 1 to 125 W and may be modularly connected to produce power up to ~5 kW. The maximum temperature gradient between the hot and cold side can be as high as 70°C (Riffat & Ma, 2003). The general TE module architecture is shown in Figure 2.8. Given the nature of TE modules as solid-

state devices with no moving parts, they are durable and reliable, with over 100,000 hours of operating lifetimes, and have a simple structure. They may operate in two modes: as thermoelectric generators (TEGs), generating electricity from a temperature gradient, or as thermoelectric coolers (TECs), converting a direct current into a temperature gradient (Ahiska et al., 2012).

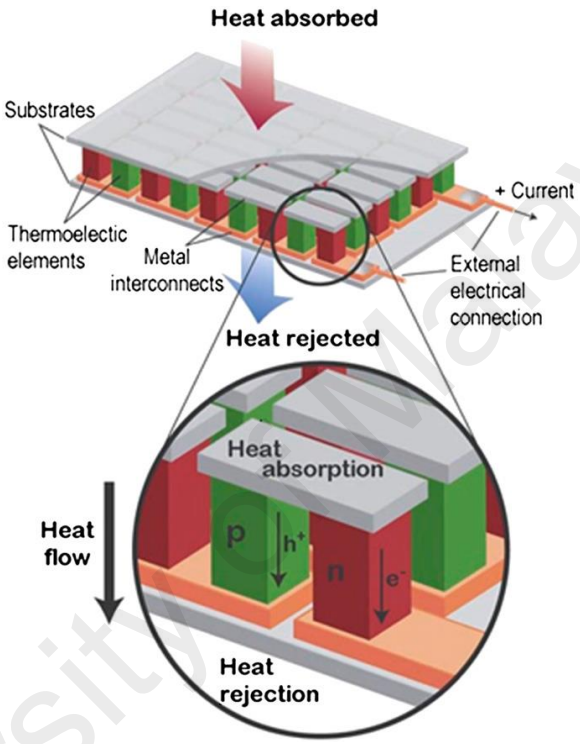

Figure 2.8: Schematic of atypical thermoelectric device (Saidur et al., 2012).

2.6.1 Applications of thermoelectric devices as coolers

Thermoelectric coolers, which are commonly known as Peltier coolers, have been successfully commercialized for high-performance, niche cooling systems that require high heat-flux dissipation to a very low temperature at a precise rate. These Peltier coolers are well suited for such applications, for which a conventional air-cooling system is no longer adequate to remove the heat fluxes at a sufficiently high rate. The general design criteria for these TECs include high reliability, flexibility in packaging and integration and low weight (Chein & Huang, 2004; Putra et al., 2011).

2.6.1.1 Cooling electronic devices

In electronic cooling applications, a thermoelectric cooler (TEC) serves as a device for transporting heat away from a surface that has a temperature higher than the ambient temperature. The purpose of a TEC is to maintain the junction temperature of an electronic device below a safe temperature by pumping heat away from the device (Chein & Huang, 2004). A significant increase in both microprocessor power dissipation and CPU size has resulted in an increase in heat fluxes. As a result of the increasing miniaturization of electronic circuitry, microprocessor heat fluxes have also increased and are expected to exceed 100 W/cm^2 for many commercial applications (Putra et al., 2011). The development of thermoelectric coolers (TECs) in combination with air cooling or liquid cooling approaches has been of major thermal benefit because a negative temperature gradient and, therefore, a reduced thermal resistance can be generated with the use of a TEC. Figure 2.9 illustrates air-cooling techniques (in which a fan is simply added to blow air through the enclosure that houses the electronic components to enhance the heat transfer) for high-power electronic packages such as processors (Zhang et al., 2010).

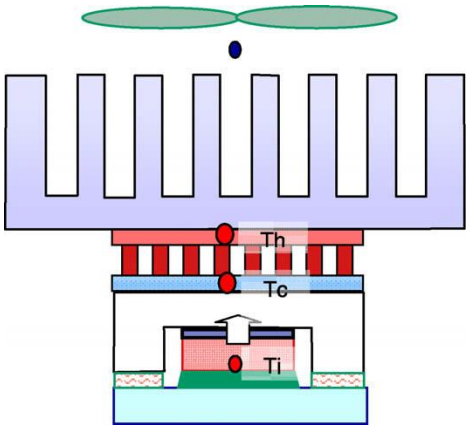

Figure 2.9: Schematic of the TEC cooling of a processor with an air cooled heat sink at the top (H. Y. Zhang et al., 2010).

In addition, TEC applications have been studied for hot-spot thermal management. To aid the design and analysis of these TECs, intensive modeling work concerning the

performance of TECs has been carried out, such as that for the material Bi_2Te_3 (PrezAparicio et al., 2012). Chang et al. (2009) a theoretical model of a thermal analogy network was developed to predict the thermal performance of a TEC with an air-cooling module. They reported that at a specific heat load, the TEC air-cooling module achieves its best cooling performance at an optimum input current between 6 A and 7 A and for heat loads between 20W and 100W. Their result also demonstrated that the thermoelectric air-cooling module performs better at a lower heat load. Similarly, Huang et al. (2010) demonstrated experimentally that the thermal performance of a conventional water-cooling device can be effectively enhanced by integrating it with a thermoelectric cooler when the heat load is below 57 W. Zhou and Yu (2012) conducted detailed analyses of the optimal allocation of the finite thermal conductance between the cold-side and hot-side heat exchangers of a TEC system. The analysis results when the constraint of the total thermal conductance was considered demonstrated that the maximum coefficient of performance (COP) can exceed 1.5 when the finite total thermal conductance is optimally allocated. However, overall, the efficiency of the hot-side heat exchanger parameters is usually the predominant factor in determining the overall performance of a TEC system (Wang et al., 2013; Zhou & Yu, 2012).

2.6.1.2 Refrigerators and air conditioners

In refrigeration applications for which cost is not the main criterion, Peltier cooling appliances provide rapid cooling; a solar Peltier refrigerator may reduce the temperature from 27°C to 5°C in approximately 44 min (Abdul-Wahab et al., 2009). A thermoelectric refrigeration system, which has the merits of being light, reliable, noiseless, rugged, and low cost in mass production, uses the charge carriers in the thermoelectric material rather than refrigerant as the heat dissipation carrier (Dai et al., 2003). One attractive application is for outdoor purposes, when operated in tandem with solar cells, as shown in Figure 2.10. In the daytime, solar cells receive solar energy and turn it into electric power

supplied to the thermoelectric refrigerator by means of the photovoltaic effect. If the amount of electric power produced is sufficient, the power surplus can be accumulated in a storage battery in addition to driving the refrigerator. If the solar cells cannot produce sufficient electric power, for example, on cloudy or rainy days, the storage battery may serve as a supplementary power source, and it can be used to power the refrigerator at night. Although the coefficient of performance of such a system is not as high as for a vapor-compression cycle (Dai et al., 2003), thermoelectric refrigerators have been used in military, aerospace, instrument, and industrial or commercial products as cooling devices for specific purposes; for example, TEC systems, when used as microclimate cooling (MCC) systems, can remove a significant amount of heat from a soldier's body while he or she is wearing combat clothing, thus increasing mission duration and enhancing mission performance (Chen et al., 2012). Luo et al. (2013) investigated the cooling potential of bulk single-phase $Bi_{85}Sb_{15}$ material. This material, which was prepared via melt spinning (MS) combined with a subsequent spark plasma sintering (SPS) technique, provided an optimized power factor of 7.9 mW/mK^2 for the sample with the highest cooling rate. Meng et al. (2011) conducted numerical studies of the cooling load and coefficient of performance of a commercial water-cooling thermoelectric refrigerator with a maximum cooling load of 2.33 W and a maximum COP of 0.54. The results demonstrated that the heat convection of the heat exchanger and the heat leakage through the air gap are the main factors that can cause irreversibility and decrease the performance of the system. The COPs of present commercial thermoelectric refrigerators (for example, Melcor's Polar TEC™ series of thermoelectric devices) are typically between 0.3 and 0.7 for single-stage applications. Moreover, COPs greater than 1.0 can be achieved when the module is removing heat from an object that is warmer than the ambient temperature (TE Technology, 2010).

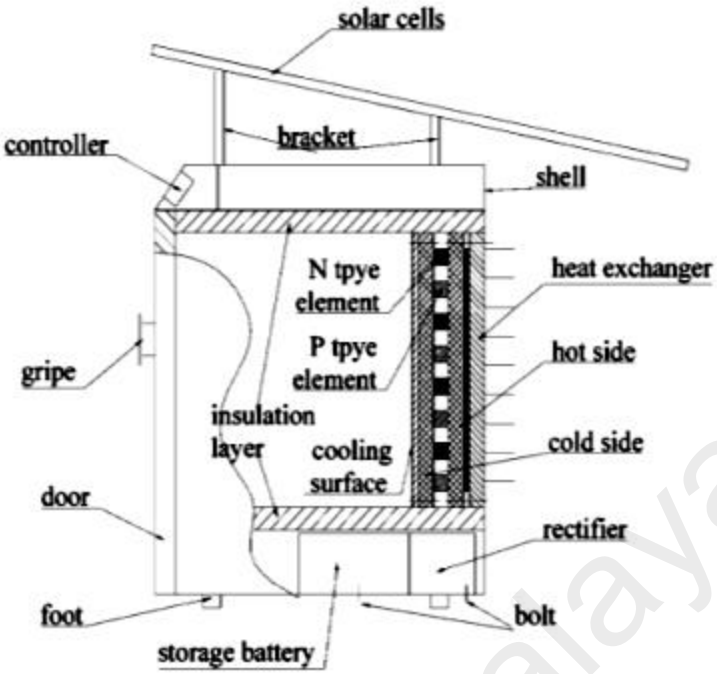

Figure 2.10: Schematic of solar cell driven, thermoelectric refrigerator (prototype) (Dai et al., 2003).

Thermoelectric air conditioners (TEACs) are environmentally friendly, simple and reliable; they offer convenient installation and support complex water distribution pipes, and switching between the cooling and heating modes can be easily achieved by reversing the input current. However, these systems are still very expensive at present (Shen et al., 2013). TEACs are portable and low noise, but they have a relatively low COP, which is an additional factor that limits their application for domestic cooling. TEACs, however, have a large potential market as air conditioners for small enclosures, such as cars and submarine cabins, where the power consumption would be low or safety and reliability would be important (Riffat & Qiu, 2004). For example, Cherkez (2012) theoretically determined the maximum coefficient of performance (COP) of an air conditioner based on a permeable thermoelectric converter. Considering the optimal structural and thermophysical parameters, including the applied electrical current and the heat-carrier

velocity in the channels of the thermo-elements, the results indicated the possibility of increasing the COP by a factor of 1.6 - 1.7.

2.6.2 Application of thermoelectric devices for power generation

Thermoelectric generators (TEG), in principle, may offer many advantages over conventional electric-power generators, such as being highly reliable, silent in operation, and environmentally friendly and containing no moving parts (Niu et al., 2009). Because of these advantages, considerable emphasis has been placed on the development of TEGs as a standalone power-generation technology for a variety of aerospace, biomedical, remote power and military applications (Riffat & Ma, 2003).

2.6.2.1 Low power generation

Body-mounted electronic devices may be broadly categorized into those intended for mobile communications purposes, such as smartphones, MP3 players and iPods, and those for medical purposes, such as hearing aids and cardiac pacemakers. The power requirements of these body-mounted devices range from 5 μW to 1 W, with a corresponding life expectancy of up to 5 years, indicating a need for an energy source that is both portable and autonomous (Vullers et al., 2009). Today, batteries represent the dominant energy source for portable devices. Although the energy density of batteries has increased by a factor of 3 over the past 15 years, in many cases, their presence has had a large impact on, or even dominated, the overall size and operational cost of portable devices (Vullers et al., 2009). Furthermore, batteries contain chemical substances or materials that are harmful to the environment, such as sulfuric acid, mercury, zinc, lithium, lead, nickel and cadmium, and exhibit toxicity that can cause damage to humans and the environment. For this reason, body-mounted TEGs are an attractive proposition, as they may be fabricated out of safer materials than Ni-Cd or lithium-ion batteries (Riffat & Ma, 2003). So far, a thermoelectric wristwatch that is driven by body heat has appeared

as one commercialized example of body-mounted TEGs. Two known manufacturers of these TEG wristwatches are Seiko and Citizen; the Seiko watch typically produces 300 mV of open-circuit voltage from a temperature gradient of 1.5 K, and its efficiency is approximately 0.1% (Snyder, Fall 2008).

2.6.2.2 High power generation

(a) Waste heat thermoelectric generators

Traditionally, large-scale electricity generation is achieved via the burning of fossil fuels (e.g., heat engines) or from nuclear or hydropower sources. Each of these technologies has some disadvantages in terms of environmental impact. For example, the burning of fossil fuels has been linked to environmental pollution and global warning, while nuclear electricity carries a risk of nuclear meltdown, as demonstrated by the 2011 Fukushima disaster. TEGs circumvent these problems, as they generally offer a low environmental risk. Furthermore, TEGs are an intelligent way of mitigating the adverse effects of global warming, as they are able to generate electricity by harvesting waste heat, such as heat that is the byproduct of industrial processes, such as the steelworks industry, and automobile engines. Recognizing the potential of waste heat as an energy resource, these two industries have been the main driving force behind the development of commercial TEGs for high-power electricity generation. The energy-conversion efficiency of a TEG (η_{te}) is determined by both the operating temperature of the generator and the unitless figures of merit (ZT) of the thermoelectric materials used, as follows:

$$\eta_{te} = \left(\frac{(T_h - T_c)}{T_h}\right)\left(\frac{\sqrt{(1+ZT)} - 1}{\sqrt{(1+ZT)} + \frac{T_c}{T_h}}\right) \qquad 2\text{-}6$$

where T_h is the hot-side temperature, and T_c is the cold-side temperature; these temperatures are selected based on the application of the TEG. Komatsu's Bi_2Te_3-based

thermoelectric generator, touted as the world's most efficient, has η_{te}=7.2% and produces an output density of approximately 1 W/cm^2 when operating at T_c= 30°C and T_h= 280°C (Group, 2010). In the case of waste-heat-recovery power generation, several leading automobile manufacturers, such as Volkswagen, Volvo, Ford and BMW, have been developing TEG waste-heat-recovery systems to improve the fuel economy of their automobiles with potential power generated from the TEGs in the range of ~1 kW. Even despite the currently low TEG efficiency, diligent harvesting of waste heat from resources such as automobile exhaust via judicious design and fabrication methods and maintenance strategies render TEGs a worthwhile technology for investment by these automobile manufacturers (Snyder, Fall 2008). A TEG with a *ZT* of 1.25 and an efficiency of approximately 10% could be used to harvest 35% to 40% of the energy from the exhaust manifold, which has an average temperature of 250°C, to generate useable power that would contribute directly to the operation of the equipped vehicle, which could increase fuel efficiency by up to 16% (Yu & Chau, 2009). Most of these automobile TEGs use BiTe-based bulk thermoelectric materials, as an optimal *ZT* in the temperature range < 500 K may be achieved using this compound, and therefore, the manufacturing processes for this compound have been extensively developed. Table 2.3 presents the characteristics of available thermoelectric generator semiconductors (Tie & Tan, 2013). Hsu et al. (2011) have designed a system for the recovery of waste heat that comprises 24 TEG modules to convert heat from the exhaust pipe of an automobile to electrical power; a temperature difference of 30 °C was able to produce a total power output of 12.41 W. In another development effort, Karri et al. (2011) simulated a performance comparison of a TEG containing bismuth telluride (Bi_2Te_3) and quantum-well (QW) thermoelectric materials. The TEGs containing these two materials were placed in the exhaust streams of a sports utility vehicle (SUV) and a stationary, compressed-natural-gas-fueled engine generator set (CNG). The results predicted an increase in power between the QW- and

Bi_2Te_3-based generators of approximately a factor of three for the SUV and a factor of seven for the CNG generator under the same simulation conditions. The relative fuel savings for the SUV averaged approximately -0.2% using Bi_2Te_3 and 1.25% using the QW generator. For the CNG case, the fuel savings was approximately 0.4% using Bi_2Te_3 and approximately 3% using the QW generator. However, any temperature fluctuation on the hot side leads to a rapid change in the output power generated by the TEG, which is dangerous to electric devices (Gou et al., 2013).

Table 2.3: The characteristic of available thermoelectric generator materials.

Temperature (°C)	**Type**	**TEG materials**	***ZT* (maximum)**
< 150	p	Bi_2Te_3	0.8
	n	Bi_2Te_3	0.8
150 - 500	p	Zn_4Sb_3	-
	p, n	PbTe	0.7 – 0.8
	p	TeAgGeSb(TAGS)	1.2
500 - 700	p	$CeFe_4Sb_{12}$	1.1
	n	$CoSb_3$	0.8
700- 900	p, n	SiGe	0.6 – 1.0
	p	LaTe	0.4

(Tie & Tan, 2013)

While the energy conversion efficiency is a useful metric for considering the performance and selection of TEGs, the cost of generating electricity is of comparatively equal importance for the development of commercial devices. For practical applications, the cost of power generation – as governed by material, manufacturing, and heat-exchanger costs – is a critical factor that is not captured by the figure of merit, *ZT*, alone (Yee et al., 2013). Komatsu, which boasts the world's highest-efficiency TEG module, in

their technical report by Sano et al. (2003), deduced that the selling prices of Bi-Te-based thermoelectric modules range from $7 to $42 per watt at a maximum energy-conversion efficiency of 15%. Consequently, current applications of TEGs are restricted to niche sectors where reliable power generation is required irrespective of cost and efficiency, such as deep-space missions and oil and gas platforms.

(b) Solar thermoelectric generators (STEGs)

Solar thermoelectric generators (STEGs) were initially designed and optimized for space applications because of their advantages of reliability and long lifetimes as well as their ability to capture high levels of incident solar radiation in extraterrestrial regions; however, much of the recent interest in these systems has been focused on residential solar-thermal-energy harvesting (Deng et al., 2013; He et al., 2012; Kraemer et al., 2012; SOmer & Infield, 1998, 2000; Suter et al., 2010; Xi et al., 2007; Xiao et al., 2012). The STEG may be described as consisting of a TEG and a thermal collector. Solar heat can be absorbed by the thermal collector and then concentrated and conducted over the thermoelectric generator using a fluid pipe or some other means. Subsequently, the thermal resistance of the thermoelectric generator will lead to a temperature difference that is proportional to the heat flux from the absorber of the thermal collector to the fluid. As a result, electric power will be generated by the thermoelectric generator, and this power will be proportional to the temperature difference (Xi et al., 2007). Suter et al. (2010) simulated a 4-leg TEC module consisting of two pairs of p-type $La_{1.98}Sr_{0.02}CuO_4$ and n-type $CaMn_{0.98}Nb_{0.02}O_3$ legs sandwiched between two ceramic Al_2O_3 hot/cold plates and exposed to concentrated solar radiation. The heat-transfer analysis for the module indicated that a large amount of solar heat is lost in such STEGs: more than 70% of the incident solar power was lost to re-radiation and free convection from the absorber, while 20% was conducted through the legs, and <10% was lost via radiation to the cold plate, resulting in a maximum efficiency of only 0.081%. Further experimental and analytical

improvements to overcome these thermal losses were achieved by He et al. (2012), who incorporated thermoelectric modules with glass evacuated-tube heat-pipe solar collectors (SHP-TE). The simulation results indicated that the evacuated-tube heat-pipe solar collectors had a significant effect on the TEG by increasing the thermal efficiency by approximately 55%, which may increase the performance to above 1%. Meanwhile, Kraemer et al. (2012) predicted a peak efficiency of 5 with a thermoelectric material cost of below 0.05 $\$/W_p$ by modeling an optimized methodology for terrestrial solar thermoelectric generators (STEGs). Miljkovic and Wang (2011) modeled and optimized a novel hybrid solar thermoelectric (HSTE) system that uses a thermosyphon to passively transfer heat to a bottoming cycle to determine the overall performance in a temperature range of 300–1200 K for solar concentrations of 1–100 suns and various thermosyphon and thermoelectric materials with a geometry resembling an evacuated-tube solar collector. Bismuth telluride, lead telluride, and silicon germanium thermoelectrics were studied with copper/water, stainless-steel/mercury, and nickel/liquid-potassium thermosyphon/working-fluid combinations. The system contained a parabolic trough mirror that concentrated solar energy onto a selective-surface-coated thermoelectric to generate electrical power, and a thermosyphon adjacent to the back side of the thermoelectric maintained the temperature of the cold junction and carried the remaining thermal energy to a bottoming cycle; see Figure 2.11. This HSTE system demonstrated that ideal efficiencies as high as 52.6% can be achieved at a solar concentration of 100 suns and a bottoming-cycle temperature of 776 K. However, the performance of a solar thermoelectric generator is primarily limited by the thermoelectric materials used to construct it; bismuth telluride is a favorable low-temperature thermoelectric material that exhibits advantageous properties and can reaches a maximum of ZT~1 at low temperatures in the range of (25–225°C), while filled skutterudite is a good medium-temperature thermoelectric material that can be operated over a wide temperature range

(25–525°C) (Xiao et al., 2012). Moreover, the total conversion efficiency for solar energy of a solar thermoelectric generator based on a multi-stage thermoelectric module could be as high as 10%. With the continuous emergence of new thermoelectric materials, solar thermoelectric generators using multi-stage and hybrid-generation-system (HGS) thermoelectric modules will have good application prospects (Deng et al., 2013; Xiao et al., 2012).

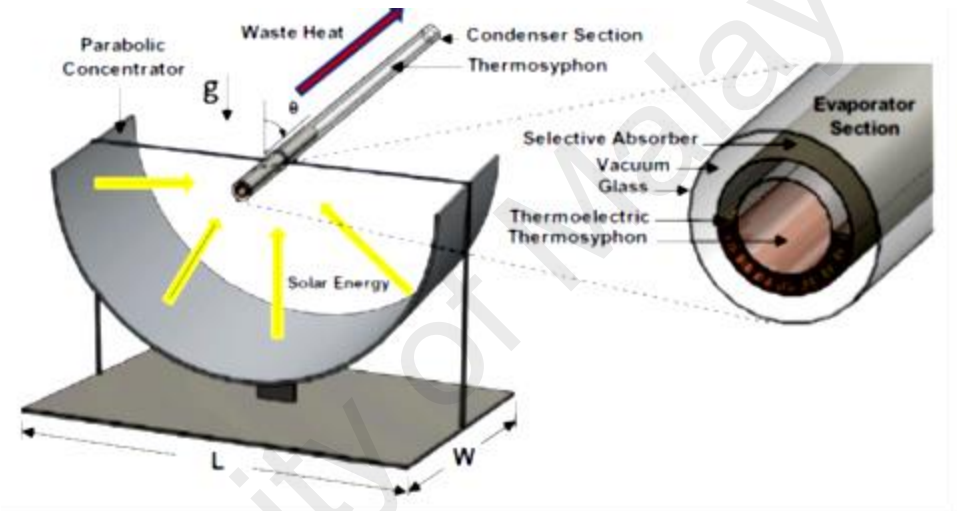

Figure 2.11: Schematic of the hybrid solar thermoelectric system (HSTE). (Miljkovic & Wang, 2011).

2.6.3 Applications of thermoelectric devices as thermal-energy sensors

Many new types of thermal-energy sensors based on the Peltier effect or Seebeck effect of thermoelectric modules have been developed in the last two decades, such as sensors for power ultrasound effects (Faid et al., 1998), cryogenic heat-flux sensors (Ahamat & Tierney, 2011; Faid et al., 1998), water-condensation detectors (Sawaguchi et al., 2005; Vancauwenberghe et al., 1996), fluid-flow sensors (Jacobs, Kutzner, Kropp, Brokmann, et al., 2009; Jacobs, Kutzner, Kropp, Lang, et al., 2009; Stachowiak et al., 1998), and infrared sensors (Escriba et al., 2005; Hirota et al., 2007; Ihring et al., 2011; Mülller et

al., 1996; Ploteau et al., 2007; Sion et al., 2012). These sensors generally rely on the conversion of heat into electrical signals or vice versa.

Infrared (IR) sensors, which operate on the principle that any mass radiates heat, allow the detection of heat using the Seebeck effect; the absorption of heat causes a specific temperature rise, which subsequently produces a Seebeck voltage. The main sensor parameters are the responsivity, which is given by the ratio of the sensor voltage to the incoming radiation power; the time constant; and the noise voltage (Escriba et al., 2005; Mülller et al., 1996). Hirota et al. (2007) developed a low-cost thermoelectric infrared sensor (thermopile) using polysilicon with a precisely patterned Au-black absorber that provides a high responsivity of 3900 V/W and a low cost potential. However, most thermoelectric IR sensors are able to operate in the range of 7 to 14 μm.

Kopparthy et al. (2012) developed a thermoelectric microfluidic sensor (TMS) for biochemical applications. The device consists of a 100 μm deep microfluidic channel with a Bi/Sb thin-film thermopile attached to its bottom surface. The device has a sensitivity of 0.045 V-s J^{-1} when known quantities of energy are applied to a nichrome heater incorporated on the inner side of the bottom wall of the microfluidic sensor bottom channel wall, while continuously injecting deionized (DI) water. Using the Seebeck and Peltier effects Stachowiak et al. (1998) developed a fluid-flow sensor for use in the low-velocity range. This sensor, when placed in a typical cylindrical duct of 100 mm in diameter, produced an output signal of 185 μV for a fluid-flow range from zero to 1.5 m^3/s with a maximum error of ± 4%. A sensor system combining a novel pressure-stable thermoelectric flow and an impedimetric sensor for monitoring chemical conversion in microfluidic channels was developed by Jacobs et al. (2009). Both sensor chips were optimized for hydraulic diameters of ~1 mm and exhibit a high chemical, temperature and

pressure stability. However, in terms of size and light weight, the most effective structure for thermoelectric sensors is the thin-film structure (Kozlov, 1999, 2000).

2.6.4 Aerospace applications

Advanced autonomous power systems that can be operated continuously and independently of the sun and are capable of providing electric power from a few watts to hundreds of kilowatts for 7–10 years are required for extraterrestrial exploration vehicles. For example, the solar brightness on Mars and Jupiter is as weak as 45% and 4%, respectively, and it is negligible on other planets. As a result, the solar option is suitable only for robotic and spacecraft missions that are limited in their time scope of operation and require only a few watts of electrical power (~10 W) (El-Genk & Saber, 2005). Radioisotope thermoelectric generators (RTGs) have been used by the United States to provide electrical power for spacecraft since 1961. The required electrical output power levels can be achieved by the appropriate selection of a number of general-purpose heat-source (GPHS) modules incorporated in an RTG system. A GPHS module is a composite carbon body that houses a total of four fuel pellets and acts as an aero-impact shell. The isotope fuel for the GPHS-RTG is in the form of plutonium dioxide ($^{238}PuO_2$) at approximately 80% density. For power conversion by the GPHS-RTG, thermoelectric junctions have been used, such as SiGe junctions (O'Brien et al., 2008). SiGe unicouples partially convert the heat generated by the radioactive decay of ^{238}Pu in the $^{238}PuO_2$ fuel pellets that are encapsulated in the general-purpose heat-source (GPHS) modules (El-Genk et al., 2003), as shown in Figure 2.12. Previously, lead telluride was used as the thermoelectric converter for lower-powered RTGs operated at a maximum hot junction temperature of <865 K to produce a power of ~2.7 W_e (Rinehart, 2001). Because of the deleterious effects of oxygen on these materials (Lange & Carroll, 2008), silicon-germanium thermoelectric elements were later adopted for high-powered RTGs operated at high temperatures of up to 1275 K (Rinehart, 2001). Their sublimation rates and

oxidation effects, even at these higher temperatures, can be controlled by the use of sublimation barriers around the elements and an inert cover gas within the generator during ground operation (Lange & Carroll, 2008). In 1976, the Lincoln Experimental Satellite (LES) 8/9 was the first spacecraft to use the new ">150 W_e multi-hundred watt (MHW) RTG," which employed 312 SiGe-alloy thermoelectric elements per RTG (Bennett et al., 1996).

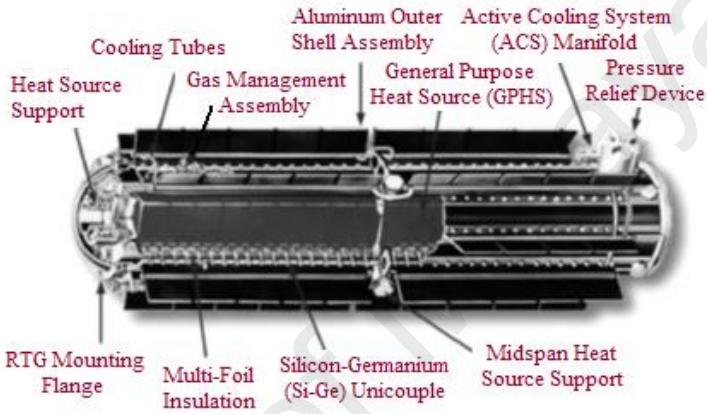

Figure 2.12: Current RTGs with 18 GPHS modules and SiGe thermoelectric unicouples for generating 280 We at beginning of life (~5.5 We/kg) (El-Genk et al., 2003).

Recently, skutterudite alloys with ZTs ranging from ~0.92 to 1.48 in the temperature range from 300 to 973 K (El-Genk et al., 2003) have been developed at the Jet Propulsion Laboratory (JPL) in Pasadena, California and are being considered for use in Advanced Radioisotope Power Systems (ARPSs) to support NASA's planetary exploration missions (El-Genk et al., 2006). The use of skutterudite unicouples in the bottom array with SiGe unicouples in the top array has been proposed for cascaded thermoelectric modules (CTMs) for use in radioisotope power systems (RPSs) to generate electric power of 108 W_e and to achieve a net decrease of ~43% in the required amount of $^{238}PuO_2$ (El-Genk & Saber, 2006). However, an operational issue with skutterudite-based unicouples is the sublimation of antimony from the legs near the hot junction at ~973 K. Such sublimation

could change the thermoelectric properties of the material and degrade the unicouples' performance over time (El-Genk et al., 2006). The use of TEGs in commercial aerospace vehicles, which is expected to reduce fuel consumption by 0.5%, is also being explored by Boeing Research & Technology (Huang, 2009). As a rough estimate, this fuel savings, if implemented solely in the US, would save passenger and cargo airlines more than $12 million every month and reduce global carbon emissions by 0.03% (Kousksou et al., 2011).

CHAPTER 3: METHODOLOGY

3.1 Synthesis of skutterudite materials

In this research, $CoSb_3$ skutterudite voids were filled with transition metals such as Mn and Hf, as well as other metals such as Al, to form ternary skutterudites. This strategy is a departure from the conventional approach of substituting Co atoms in skutterudites, as attempted by Kitagawa et al. (2005) and Ur et al. (2007) using Ni and Fe in the $CoSb_3$ matrix. Next, the effect of excess doping on the texture of the grain boundaries in enhancing thermoelectric performance was assessed through Al addition.

Ternary skutterudite formulations were then investigated with lanthanide (Yb) acting as a partial filler for $CoSb_3$ skutterudite. In this work, doping of Al and Bi was attempted to modify grain boundaries to achieve superior thermoelectric performance. The particle size and purity of the elements used in the synthesis and the atomic ratio of the formulations are shown in Table 3.1. The synthesis and characterization of the skutterudite materials included two preparation steps and several properties, which are shown in the flowchart of Figure 3.1.

Table 3.1: The elements used in the synthesis and the atomic ratio of the formulations

Materials	Formulation
Elemental Powders	Mn (200 mesh, >99.9 wt%), Hf (200 mesh, >99.9 wt%), Al (200 mesh, >99.99 wt%), Bi (200 mesh, >99.9 wt%), Yb (200 mesh, >99.9 wt%), Co (22 mesh, >99.998 wt%) and Sb (200 mesh, >99.99wt%)
Ternary Skutterudites	(1Mn:4Co:12Sb), (1Hf:4Co:12Sb), (0.3Al:4Co:12Sb), (0.6Al:4Co:12Sb), and (2Al:4Co:12Sb)
Quaternary Skutterudites	(0.1Al:0.25Yb:4Co:12Sb), (0.2Al:0.25Yb:4Co:12Sb), (0.3Al:0.25Yb:4Co:12Sb), and (0.1Bi:0.25Yb:4Co:12Sb
Quintuple Skutterudites	(0.1Al: 0.05Bi:0.25Yb:4Co:12Sb)

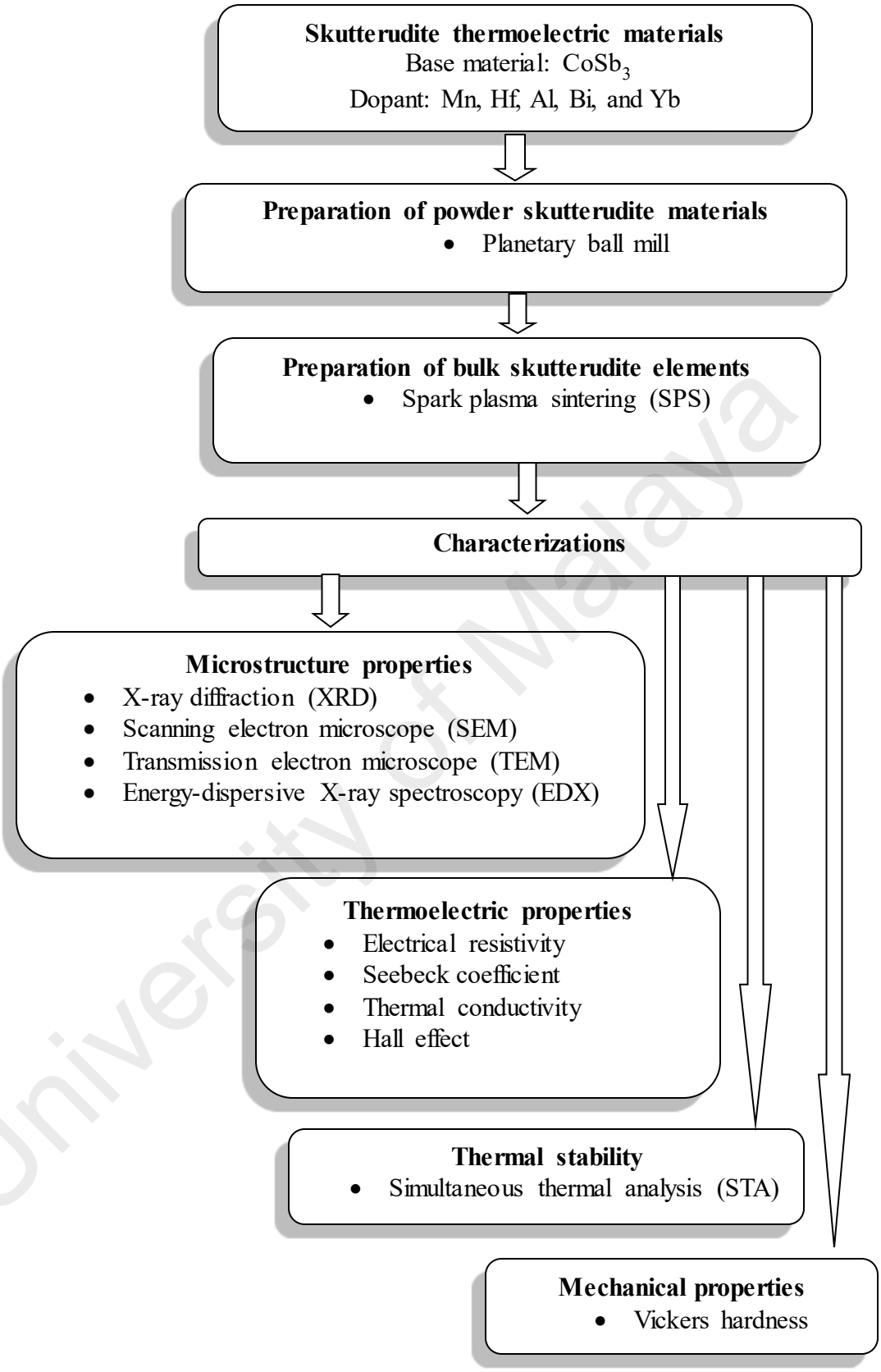

Figure 3.1: Flowchart of sample preparation and characterizations.

3.1.1 Mechanical alloying technique

The mixed powders were subjected to mechanical alloying in a planetary ball mill (GOKIN Ltd., PLANET) with a milling time of 10 h. Zirconium oxide vials and balls (φ=5 mm) were used. The ball-to-powder weight ratio was maintained at 15:1. The rotation speed was fixed at 400 rpm. To avoid contamination and oxidization, the powders were loaded and unloaded in a glove box filled with an argon atmosphere.

3.1.2 Spark plasma sintering process

Using the spark plasma sintering (SPS) system shown in Figure 3.2(a), the powders pretreated by MA were pressed under a vacuum atmosphere in a cylindrical die with an inner diameter of 10 mm that was lined with graphite sheet to facilitate easy removal of the sintered compact. The sintering process was performed under a uniaxial press static pressure of 36 MPa combined with a pulsed DC power supply via the graphite die. A heating rate of 100 °C min^{-1} from room temperature to 600 °C was used. The temperature was then held at 600 °C for 10 min, after which the sample was left to cool naturally for 2 hours. Temperature control during the SPS process was carried out using a K-type thermocouple located in a hole that had been drilled into the graphite die up to 1 mm to the sample/die interface (see Figure 3.2(b)). The actual temperature distribution within the powder sample, which depends on the sample material's electrical conductivity and the die wall thickness and material, can deviate from the measured temperature, and thus only an 'apparent' temperature is recorded by this method. Finally, the disc sample obtained from the SPS process was extracted from the die and manually ground (see Figure 3.2(c)) to remove the remaining graphite sheet stuck to the sample surface from the process. Silicon carbide (SiC) sandpaper was used to grind the samples. The SiC sandpaper was selected by grit size in a sequence of 800, 1200, 2400, and 4000; the grit is the number of grains of silicon carbide per square inch of abrasive paper.

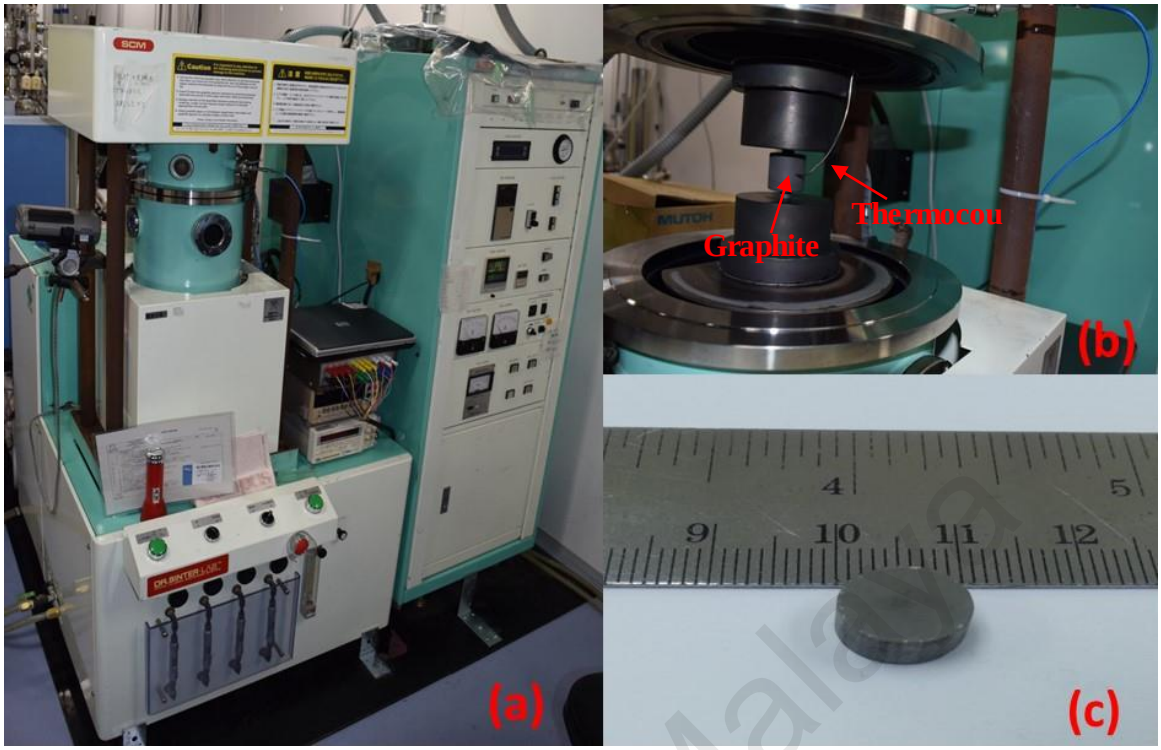

Figure 3.2: (a) Spark plasma sintering (SPS) system, (b) graphite die inside the chamber, and (c) the final disc shape after the SPS process.

3.2 Microstructural analysis

3.2.1 X-ray powder diffraction

In this study, X-ray diffraction (XRD) was used to elucidate structural information of the disc samples using the Bruker AXS D8 Advance X-ray diffraction spectrometer shown in Figure 3.3 with Cu-Kα at a wavelength of 1.5406 Å. The patterns were recorded in a 2θ range between 10° and 90° at a rate of 0.0264 in step width. The lattice parameters of the compound were calculated using the following formulae:

$$\frac{1}{d^2} = \frac{h^2}{a^2} + \frac{k^2}{b^2} + \frac{l^2}{c^2} \text{ and } d = \frac{\lambda}{2\sin\theta} \qquad 3\text{-}1$$

The scattered waves produced a unique pattern corresponding to the compositions of the sample, and comparative analysis was therefore performed using HighScore Plus

software to determine the chemical composition of the samples from their recorded patterns.

Figure 3.3: Bruker AXS D8 Advance X-ray Diffraction spectrometer.

3.2.2 Scanning electron microscopy

The samples were subsequently ground and polished with a "Struers TegraPol-21" machine. Silicon carbide (SiC) sandpaper was used to grind the samples. The SiC sandpaper was selected by grit size in a sequence of 800, 1200, 2400, and 4000. The rotation direction of the sample holder was contrary to the direction of the grinding disc rotation. The duration with each grit size was 1 min under 15 N of force at a disk speed

of 150 rpm. Tap water was used for lubrication during grinding by the SiC sandpaper. The specimens and holding disk of the grinding machine were washed and dried after each use to prevent contamination from larger grit sizes. After grinding with the 4000 SiC sandpaper, the polishing process began with a polycrystalline diamond suspension as the abrasive (particle size: 3.0 μm) on a MD-MOL polishing cloth. Final polishing was performed with a MD-CHEM polishing cloth using a colloidal silica suspension (particle size: 0.04 μm). After polishing, the sample surface was thoroughly cleaned with distilled water and methyl alcohol and dried with a hot air blower to eliminate water spots and to remove any remaining residue.

Scanning electron microscopy was used to observe the specimen surfaces. When the specimen is irradiated with a fine electron beam (called an electron probe), secondary electrons are emitted from the specimen surface. The topography of the surface can be observed by two-dimensional scanning of the electron probe over the surface and acquisition of an image from the detected secondary electrons. The SEM instrument contains an electron optical system to produce an electron probe, a specimen stage to support the specimen, a secondary electron detector to collect secondary electrons, an image display unit, and an operation system to perform various operations.

The FEI Helios 450HP dual beam linked with energy-dispersive X-ray spectroscopy (EDX) shown in Figure 3.4 was used for imaging, structure determination and elemental mapping. The FEI Helios NanoLab 650 dual beam is a state-of-the-art scanning electron microscope (SEM) and a focused ion beam (FIB) packaged in one instrument, designed for extremely high-resolution 2D and 3D characterization, nanoprototyping, and sample preparation. The incredible versatility of this machine accommodates conventional imaging and analysis in addition to site-specific analysis, deposition, and ablation of materials with the ion beam. In this system, the SEM is configured to provide complete

analysis of the samples. This includes true surface imaging, atomic number imaging, elemental analysis (energy dispersive X-ray spectroscopy), and crystal orientation (electron backscattered diffraction).

In this study, the FIB was used for high-resolution imaging and real phase structure determination. In addition, because the main purpose of this source is sample preparation, the FIB was used to remove materials for the preparation of electron transparent lamellae for subsequent scanning transmission electron microscopy.

Figure 3.4: FEI Helios 450HP DualBeam FIB-SEM.

3.2.3 Transmission electron microscopy

After the electron transparent lamellae was prepared by FIB, the transmission electron microscope (TEM), model Tecnai G2 F20 from FEI, shown in Figure 3.5 was used to investigate the nano-scale structure. The system was linked to an Oxford instruments EDS detector, which was used for the elemental mapping and determination of the chemical

compositions. The main features of this setup are as follows: ZrO2/W (100) Schottky field emitter (FEG); twin objective lens; point resolution: 0.27 nm; information limit: 0.16 nm; magnification range: 21x - 700 kx in TEM mode and 410x - 1350 kx in EFTEM mode; camera length range: 52 – 1500 mm in TEM mode and 110 – 7000 mm in EFTEM mode; fully computer-controlled; eucentric side-entry; high-stability CompuStage; Gatan Tridiem GIF-CCD: 2kx2k CCD camera and post column energy filter (GIF); Fischione ultra-high resolution STEM HAADF detector; single and double tilt specimen holders (α= +/- 60º); Gatan 626 cryo specimen holder, cryo transfer station and cold stage controller; FEI Vitrobot for cryo-TEM preparation; Xplore3D for automated tomographic tilt series acquisition; and Inspect 3D on a support PC for tomographic reconstructions.

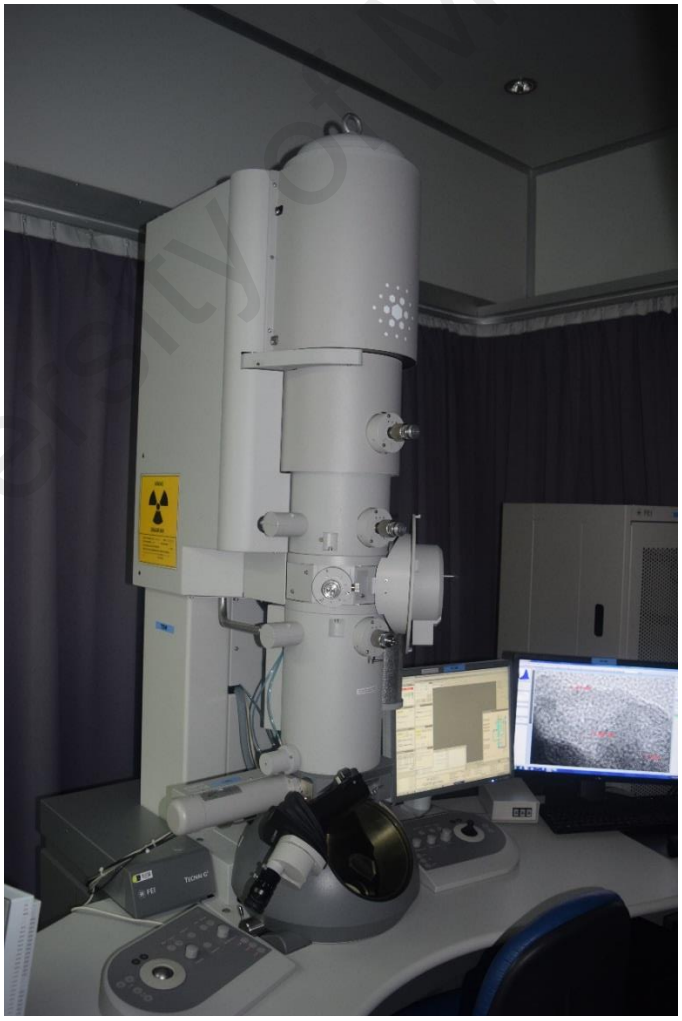

Figure 3.5: Transmission electron microscope (TEM) from FEI (model: Tecnai G2 F20)

3.2.4 X-ray Photoelectron Spectroscopy

The X-ray photoelectron spectroscopy (XPS) instrument from Ulvac Phi (model: Quanterra II) shown in Figure 3.6, also known as electron spectroscopy for chemical analysis (ESCA), was used in this work to provide quantitative and chemical state information from the surface of the material being studied. The PHI XPS instrument provided the ability to obtain spectra with a lateral spatial resolution as small as 7.5 µm, with an average depth of analysis of approximately 5 nm. Spatial distribution information was obtained by scanning the micro focused X-ray beam across the sample surface. XPS was typically accomplished by exciting the sample surface with mono-energetic Al kα X-rays, causing photoelectrons to be emitted from the sample surface. An electron energy analyzer was used to measure the energy of the emitted photoelectrons. From the binding energy and intensity of a photoelectron peak, the elemental identity, chemical state, and quantity of a detected element were determined.

Figure 3.6: X- photoelectron spectroscopy (XPS) from Ulvac Phi (model: Quanterra II).

3.3 Measurement of thermoelectric transport properties

3.3.1 Measurement setup for electrical resistivity (ρ) and the Seebeck coefficient (α)

After the SPS process, one sample of each composition was cut into a bar shape as illustrated in Figures 3.7(a) and 3.7(b). Then, the Seebeck coefficient and electrical resistivity were measured simultaneously on the ZEM-3 (Ulvac-Riko) apparatus shown in Figure 3.7(c). The electrical conductivity was measured using a four-point probe method; therefore, the voltage decline could be neglected. The sample to be measured was held vertically in between two electrodes mounted on the upper and lower blocks. An electrical heater resistance was provided at the lower block, which was responsible for creating the temperature gradient along the sample length. Therefore, two pairs of chromel-alumel (type-K) thermocouples using two channels of a Keithley 2010 digital multimeter were used to measure temperatures T_1 and T_2 and the electric potential difference dV between them across the sample. Using the electrodes, a small electric current I runs through the sample, and the thermocouple wires measure the voltage difference dE created by the current in the sample. These probes were spring loaded to ensure that there was good and direct contact between the probes and sample. Constant spacing was assumed between the two pairs of thermocouples and considered for the electrical resistivity and Seebeck coefficient calculations. From the V-I curve, the resistance, and consequently the resistivity, can be determined at various temperatures. Voltage differences of the sample over different temperatures were used to calculate the Seebeck coefficient. Therefore, the Seebeck value was calculated from the slope of ΔV vs. ΔT plot. A schematic of the electrical resistivity and Seebeck coefficient measurements is given in Figure 3.8.

This arrangement was surrounded by a nickel radiation shield to ensure an isothermal environment. The setup was enclosed in an infrared furnace with a high purity helium atmosphere to prevent oxidation of the sample at elevated temperature measurements.

Sufficient pressure was applied in between the samples and all of the contact surfaces to reduce the contact resistance. To approximate the voltage losses over these contacts, which yield incorrect voltage values, the heat and current flow was in one dimension, and the distance between the probes and end plates was maintained 1.5 times larger than the samples' characteristic lengths. The samples for the ZEM measurements were all rectangular in shape with an average size of 2 mmW×2 mm D×7 mm L ~ 4 mmW×4 mm D×9 mm L, and the measurement temperature range was from RT to 577 °C.

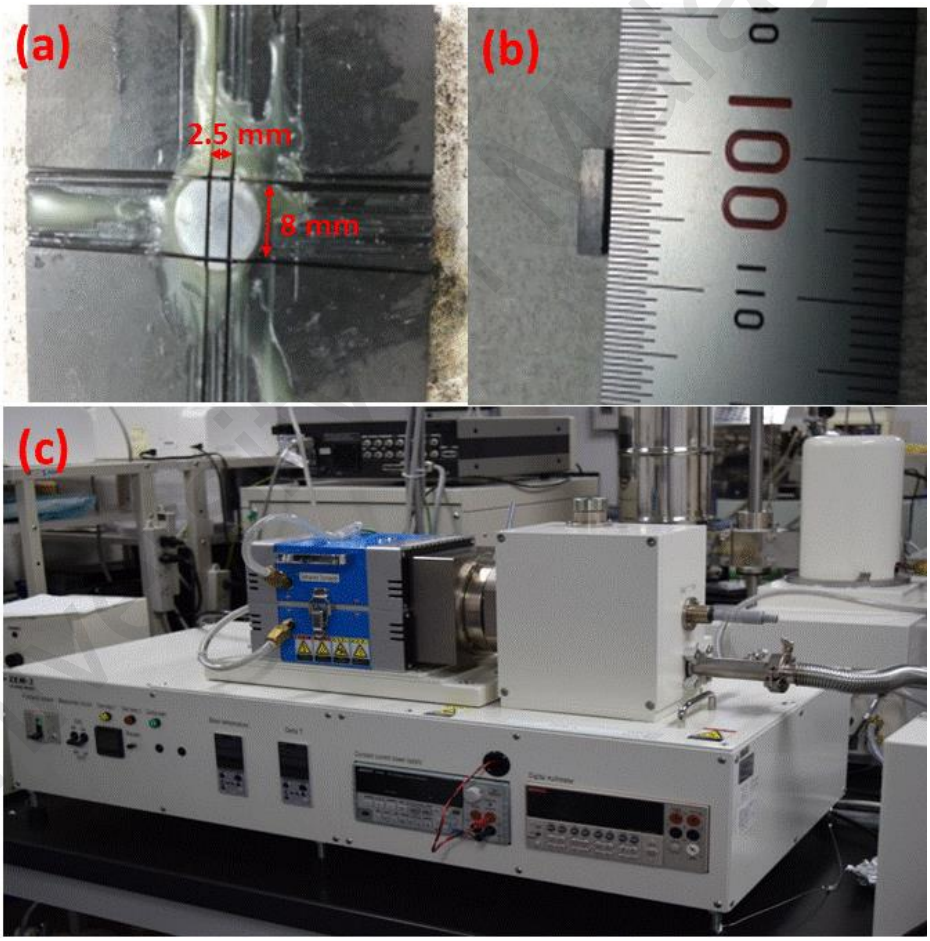

Figure 3.7: (a) Cutting the sample for electrical resistivity and Seebeck coefficient measurements, (b) final dimensions after cutting, and (c) the ZEM-3 (Ulvac-Riko) apparatus.

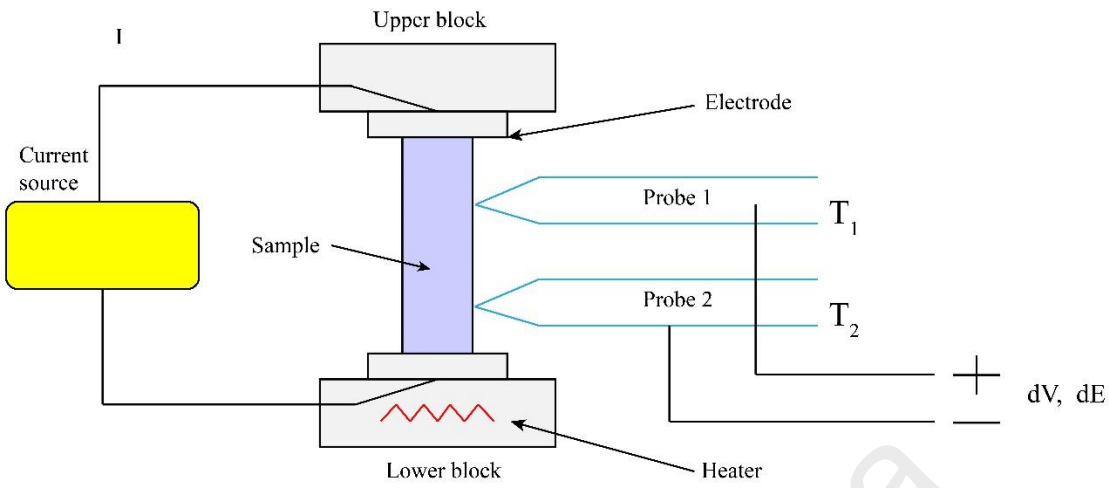

Figure 3.8: A schematic diagram of the electrical resistivity and Seebeck coefficient measurements.

3.3.2 Measurement setup for thermal conductivity

The two surfaces of the sample prepared for the thermal conductivity measurement were parallel and flat. The first step was to attach thermocouples to the sample using a ceramic paste (see Figure 3.9(a)) for the temperature reading, followed by graphite coating as shown in Figure 3.9(b) to avoid a high laser reflection, which may reduce the energy absorption and induce a bad rear face signal. The thermal conductivity was measured with a TC-7000H (Ulvac-Riko) apparatus shown in Figure 3.9(c). A laser flash method was employed for the thermal conductivity measurement in the temperature range of RT-850 K. Liquid nitrogen was used for cooling below room temperature. The system included four main parts: the infrared furnace, the electronic control console, the detector assembly, and the sample holder. In the laser flash method, a laser pulse of 1 ms or less in width was used to momentarily heat the front side of a 10 mm diameter, 2 mm thick discoid sample, and the back side temperature change was measured. The temperature of the sample was detected by the thermocouples adjacent to the sample. The thermal conductivity was calculated using the relationship $K = D \cdot C_p \cdot \rho_d$, with the thermal diffusivity D and specific heat C_p measured by a Flashline analyzer and a density of ρ_d.

The lattice thermal conductivity K_l was calculated by subtracting the electronic thermal conductivity K_e from the measured K using the Wiedemann-Franz law $K_e = L_0T/\rho$ (assuming a temperature-independent Lorenz number $L_0 = 2.45 \times 10^{-8}$ V^2/K^2).

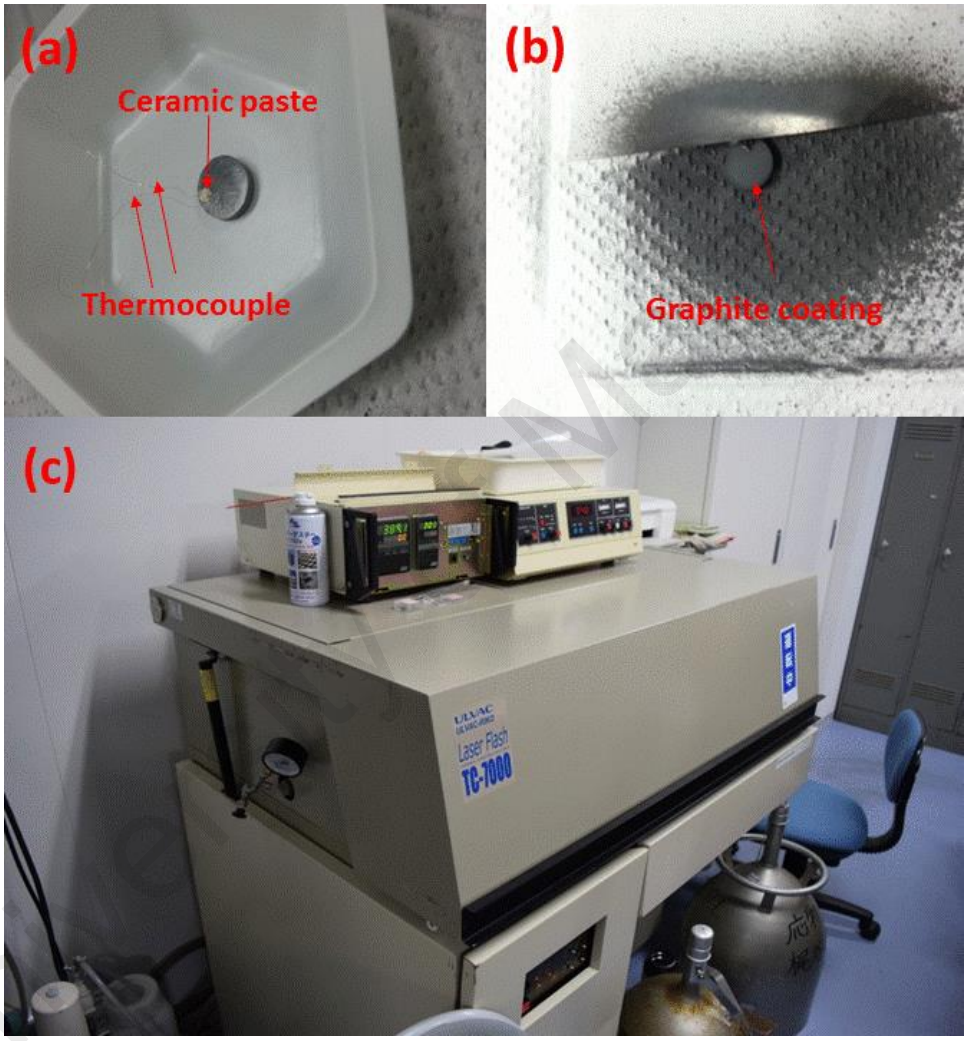

Figure 3.9: (a) Preparation of the sample by fixing the thermocouple using a ceramic paste, (b) spraying of a thin layer of graphite to coat the sample, and (c) the TC-7000H (Ulvac-Riko) apparatus.

3.3.3 Measurement setup for the Hall mobility

The Lake Shore 8400 Series (see Figure 3.10) standard system used in this study is capable of DC field measurements and has a resistance range from 0.5 mΩ to 10 MΩ. It

measures the Hall voltage, Hall coefficient, Hall mobility, and resistivity. With added options, the system can measure down to 0.5 μΩ and as high as 200 GΩ in DC fields. The carrier density and carrier mobility versus temperature can also be determined in a temperature range of 10 K to 1273 K with a closed-cycle refrigerator and high-temperature oven. In this research, a single applied field was used to characterize the room temperature and temperature-dependent transport properties of the samples being studied, with sample dimensions of Φ = 10 mm and T = 1 mm, in a temperature range of RT to 227 °C.

Figure 3.10: The Lake Shore 8400 Series instrument for Hall mobility measurement.

3.4 Simultaneous Thermal Analysis (STA)

Figure 3.11 shows the simultaneous thermal analysis equipment from PerkinElmer (model: STA 6000) that was used in an operational range of RT to 1000 °C to

simultaneous measure and analyze the weight change and heat flow and thus indicate the thermal stability as well as the melting point temperatures. Combining differential scanning calorimetry (DSC) with proven thermogravimetry (TG) enabled the generation of accurate and reliable results while simplifying data interpretation. The measurements were performed from 25 °C to 1000 °C, heating up at a rate of 5 °C/min with 100 ml/min of N_2 gas.

Figure 3.11: Simultaneous thermal analysis (STA) by a PerkinElmer instrument (model: STA 6000).

3.5 Measurement setup for mechanical properties (Vickers hardness)

The Vickers hardness was used to evaluate the ability of a thermoelectric element to resist plastic deformation from a standard source. The Shimadzu G21 series micro-hardness tester shown in Figure 3.12 was employed for this measurement under a load of 1 N sustained for 10 seconds. The micro-hardness was computed by the following equation:

$$HV = 1.891\ \frac{F}{d^2} \qquad 3\text{-}2$$

where HV is the Vickers hardness in MPa, F is the force in Newtons, and d is the average length of the diagonals of the indent in mm.

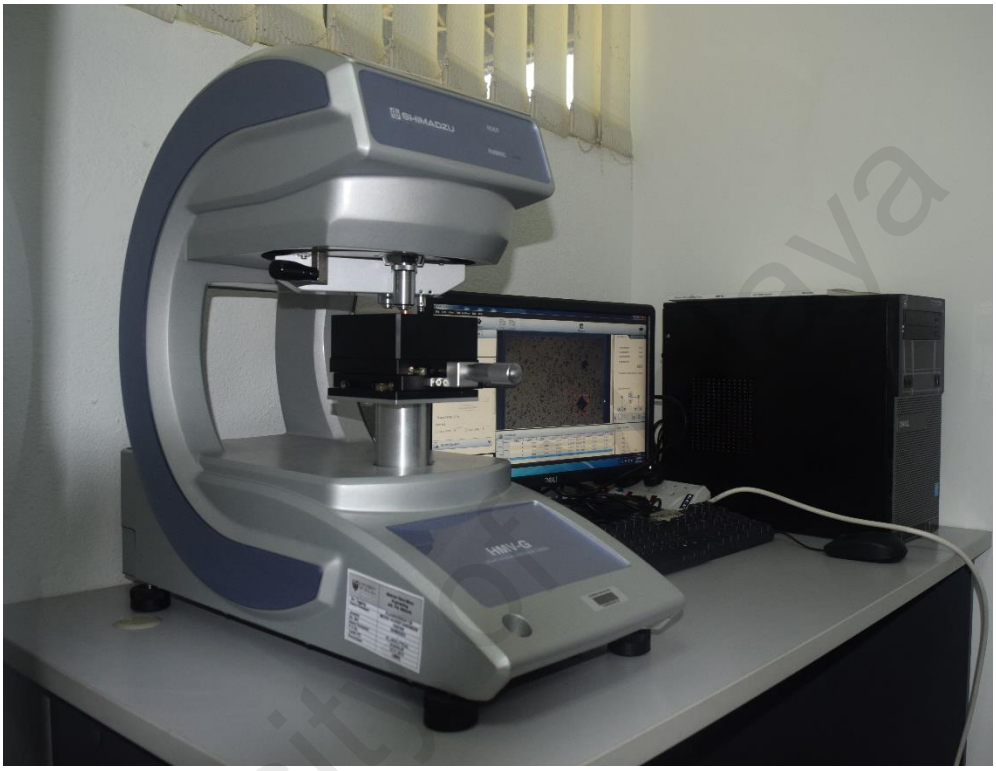

Figure 3.12: A Shimadzu G21 series micro hardness tester

CHAPTER 4: RESULTS AND DISCUSSION

In this chapter, the analysis of Mn, Hf, and Al in a $CoSb_3$ binary skutterudite material and of Al and Bi in a $Yb_{0.25}Co_4Sb_{12}$ ternary skutterudite thermoelectric material will be discussed. The formulations will be discussed individually in the context of microstructural, thermoelectric, electronic, thermal and hardness properties. In the first 3 formulations, the effect of doping (Mn, Hf, and Al) on the binary $CoSb_3$ will be discussed. In this section, a spin crossover behavior from n-p type for the formulation $Al_{0.3}Co_4Sb_{12}$ will also be presented. Next, the effect of excess doping on the microstructural and thermoelectric behaviors using Al as a case study will be elaborated. Finally, extension of doping to the ternary skutterudite $Yb_{0.25}Co_4Sb_{12}$ formulation using Al and Bi will be discussed to demonstrate the achievement of a high *ZT* using strategies to manipulate the grain boundary morphology.

4.1 Mn-added $CoSb_3$ composition

Manganese has been widely used as a main element in half and full Heusler alloy thermoelectric materials (Dyck et al., 2002; Hornbostel et al., 1997; Nolas et al., 2005; Park et al., 2014) as well as in higher manganese silicide thermoelectric materials (Luo et al., 2011; Ponnambalam et al., 2013; Saleemi et al., 2015; A. J. Zhou et al., 2010; A. Zhou et al., 2012).

In this section, Mn which has a small atomic radius, is proposed as an alternative loosely bonded filler element for the $CoSb_3$ skutterudite thermoelectric material. This approach is in contrast to the substitution approach tackled by previous research involving transition metals. For example, Mn has been used to substitute the Co side in $CoSb_3$ skutterudite (Park et al., 2014). (Kitagawa et al., 2005) prepared a single phase of skutterudite by doping Ni into the $CoSb_3$ matrix, and they found that the lattice parameter increased linearly with an increasing Ni content, indicating that the Ni atoms occupy the

Co site in the skutterudite structure. This finding was extended to include an Fe-doped $CoSb_3$ matrix in the study conducted by (Ur et al., 2007), whose found that Fe could also occupy the Co site without forming a secondary phases. Thus, it will be interesting to observe whether the doping of Mn in to the $CoSb_3$ system will succeed in filling the skutterudite voids.

4.1.1 Microstructural properties

The MAed powders were strongly deformed by the high impact of mechanical energy, and they were thermodynamically metastable (Yang et al., 2006). During the SPS process the elements were almost completely reacted into the skutterudite phase; therefore, a polycrystalline phase of filled skutterudite with a secondary phase of MnO were obtained and presented in the as-sintered XRD pattern shown in Figure 4.1. The cubic-type skutterudite structure (Im-3 space group) with a room temperature lattice constant of a = 9.0340 Å was obtained in this study, which is lower than the value of 9.0345 Å for the single crystalline $CoSb_3$. Furthermore, a small shift in the position of the binary skutterudite $CoSb_3$ (Kawaharada et al., 2001) was observed for the Mn-added $CoSb_3$. The change in the valence state and structure defect due to strain as a result of Mn substitution might be the reasons for contraction in the lattice constant as well as the shift in the 2 theta value. Furthermore, the effect of the small radii of Mn compared to the radii of Co may result in a decreased lattice parameter of $CoSb_3$, while the elements with an identical or larger radii as Co (i.e., Fe, Ni and In) (Kitagawa et al., 2005; Mallik et al., 2008; Peng et al., 2004) may result in an increased lattice parameter.

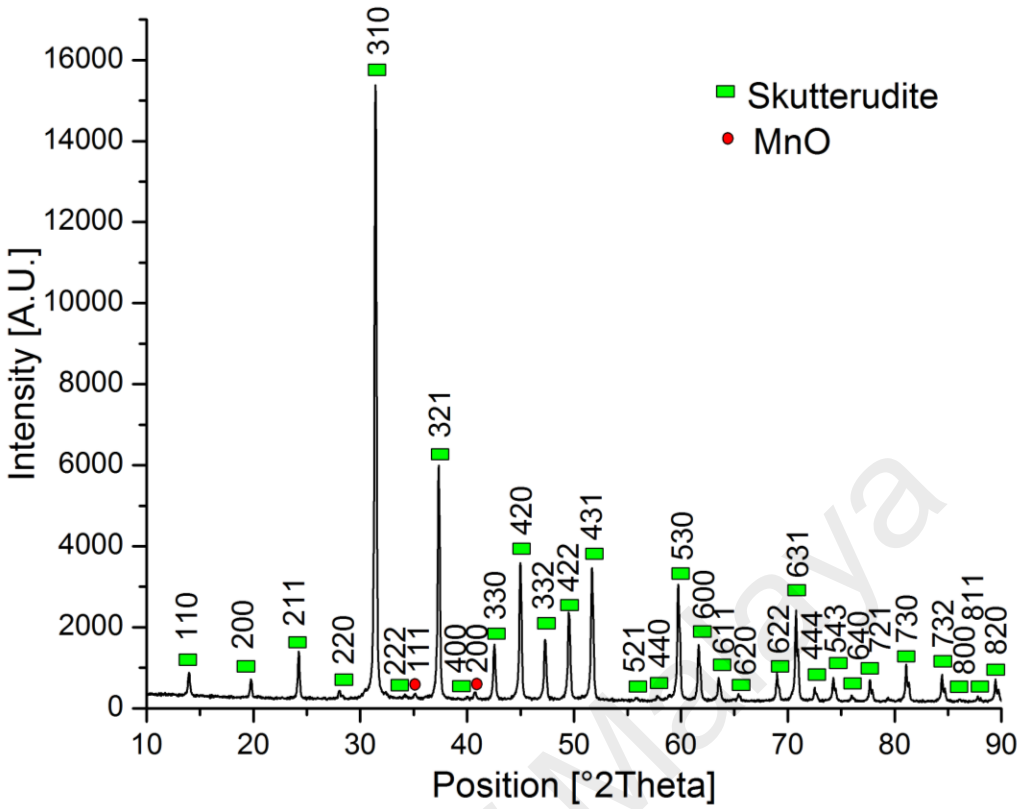

Figure 4.1: XRD pattern of the as-sintered sample of Mn-added Co_4Sb_{12}

The actual density for the as-sintered sample was found to be 6.7 g/cm^3. This relatively high density is in agreement with the small number of pores observed in the SEM micrograph image shown in Figure 4.2(a). The average grain size was less than 5 µm. The composition of the grains and the grain boundaries were investigated by EDX (Table 4.1) and are explained in Figure 4.2(a). This indicates that Mn atoms substituted the Co sites inside the grains rather than filling the skutterudite voids. However, an excess amount of Mn atoms was indicated in the grain boundaries, as well as substitution of Co sites by Mn atoms. Furthermore, the elemental mapping shown in Figure 4.2(c) indicates that Mn takes on various microstructural modification roles within the skutterudite; Mn distributed systematically in the grains, agglomerated as Mn-rich regions at the edges of the grains, and formed a nano-sized Mn-containing secondary phase along the grain boundaries. This behavior agrees with the Bi-filling $CoSb_3$ described in the work of

Mallik et al. (2013), although Bi is a heavy atom element. However, most of the lanthanides and alkali earth metals tended to fill the voids of the $CoSb_3$ without making secondary phases, if a suitable fraction was used. We can also observe some Co-rich regions in Figure 4.2(d) that might have been formed as a result of the substitution of Mn instead of Co in the skutterudite phase.

Table 4.1: EDX results indicating the actual composition of Mn-added $CoSb_3$

		Position	
No.	**Element**	**Grain composition (Atomic %)**	**Grain boundary compositions` (Atomic %)**
1	Mn	2.18	8.70
2	Co	23.33	20.82
3	Sb	74.49	70.48

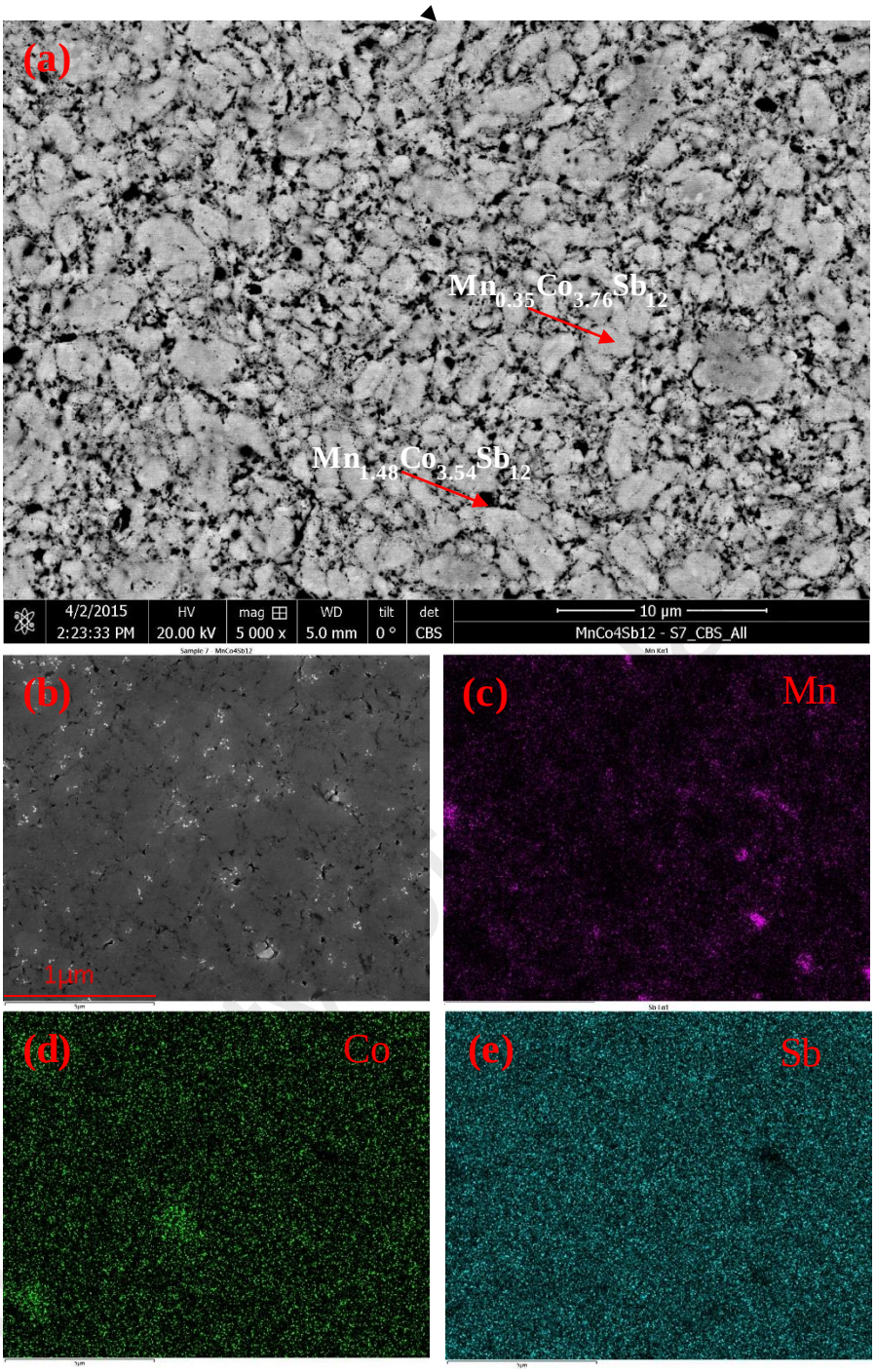

Figure 4.2: SEM images of $MnCo_4Sb_{12}$, (a) a micrograph of an SPS-compacted sample, and (b) an SEM/EDX micrograph. The elemental mapping of (c), (d), and (e) show Mn, Co, and Sb, respectively, extracted from (b) using EDX.

4.1.2 Thermoelectric properties

The electrical resistivity for the Mn-added $CoSb_3$, at the measured temperature region (RT – 577 °C) shown in Figure 4.3(a) indicates a slight decrease in the electrical resistivity of the binary skutterudite $CoSb_3$ (Kawaharada et al., 2001). The high resistivity of the skutterudite modified by Mn-addition compared to the lanthanides and alkali earth metals additions can be attributed to the presence of the MnO secondary phase which provides additional interfaces in the bulk of the material. The increased number of interfaces in the samples may lead to additional scattering of the carriers, which could result in high resistivity (Mallik et al., 2013). Moreover, due to the increase in the carrier concentration and excitation of the carriers across the band gap, the electrical resistivity decreased with increasing temperature, exhibiting a semiconducting behavior (Laufek et al., 2009).

Figure 4.3(b) shows the temperature dependence of the Seebeck coefficient (α) for the Mn-added $CoSb_3$. A positive Seebeck coefficient was observed, indicating a p-type thermoelectric material. A tiny increase in the value of α was realized from RT until 127 °C, at which point there was a peak with a value of 242 μVK^{-1}; there was then a dramatic decrease from 127 °C to 577 °C when the intrinsic effect of manganese becomes active. The absolute value of the Seebeck coefficient of Mn-added $CoSb_3$ is larger than that of $CoSb_3$ (~225 μVK-1) (Kawaharada et al., 2001). The power factor (*PF*) exhibits a parabola-like behavior (see Figure 4.3(c)) due to the reverse interrelationship between the Seebeck coefficient and the electrical conductivity. A maximum *PF* of 0.39×10^{-3} $Wm^{-1}K^{-2}$ was obtained at 277 °C.

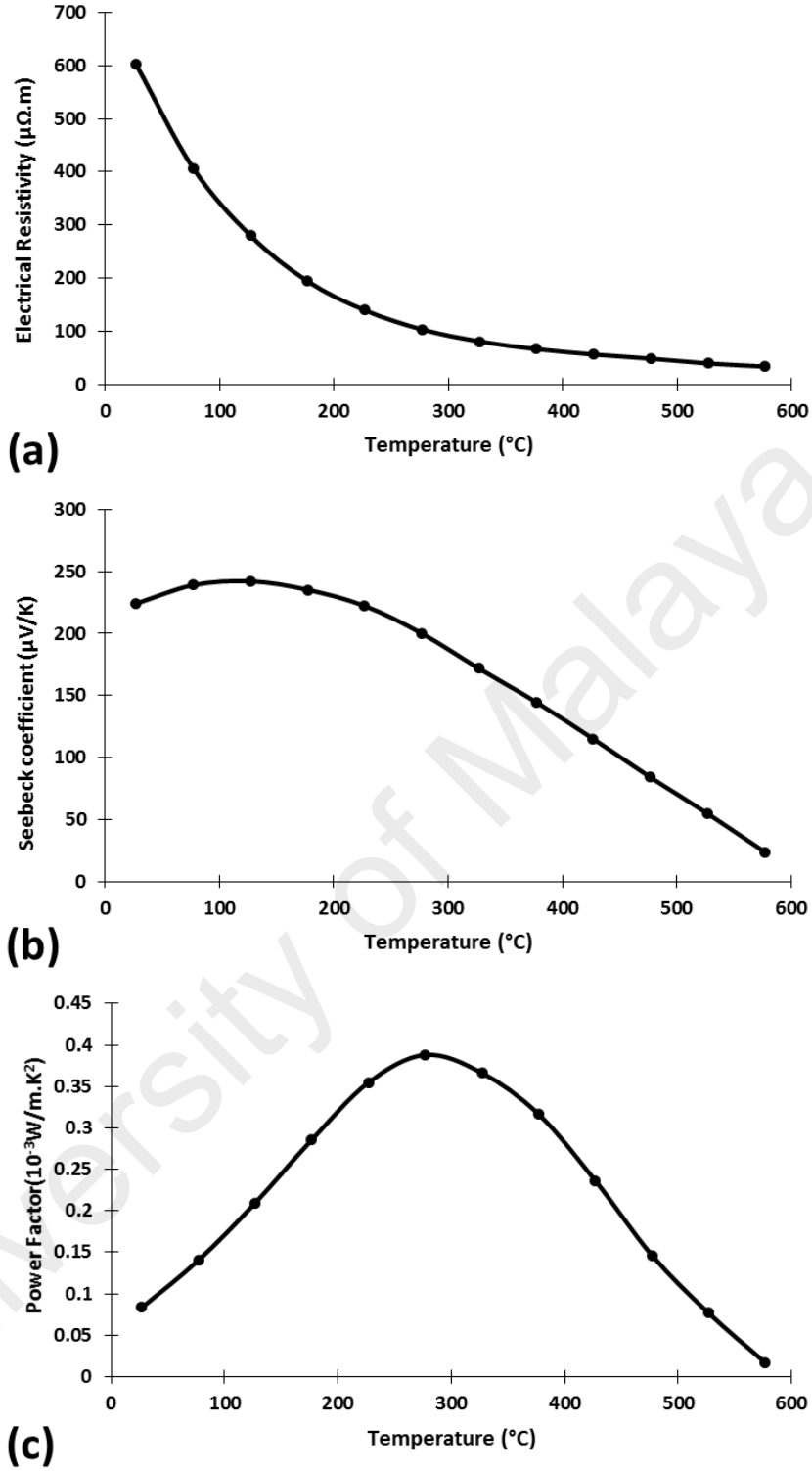

Figure 4.3: Temperature dependence of the (a) electrical resistivity, (b) Seebeck coefficient, and (c) power factor (*PF*).

Figure 4.4(a) shows the temperature dependence of the thermal conductivity (K). The thermal conductivity decreased with an increase in temperature up to 500 K, at which point K = 3.3 W/m.K (the minimum thermal conductivity of the $CoSb_3$ binary skutterudite is ~4.5 W/mK (Kawaharada et al., 2001)). Generally, the scattering of lattice vibrations becomes more vigorous with the rise of temperature. However, the thermal conductivity increased gradually from 500 K to 850 K, indicating less phonon scattering from the interfacial phase of MnO located in the grain boundaries. The lattice thermal conductivity, K_L, can be estimated by subtracting the electronic contribution, $K_e = LT/\rho$, from the total thermal conductivity, where L = 2.45 × 10-8 V^2K^2 is the Lorenz number. As shown in Figure 4.4(b), K_L was highly suppressed compared with the lattice thermal conductivity of $CoSb_3$ reported in the work of Zhang et al. (2015) due to the addition of Mn, which created a highly disordered lattice structure that was more effective in phonon scattering. Thus, the relative contribution of electron thermal conductivity to the total thermal conductivity was negligible. It is therefore evident that small and light Mn atoms are effective in reducing heat-carrying phonons. Consequently, Mn is a promising candidate for multiple doping in $CoSb_3$ materials with a heavy atom element. However, a low ZT of 0.06 at 577 K, as shown in Figure 4.4(c), was found as a result of high electrical resistivity, although the thermal conductivity was reduced.

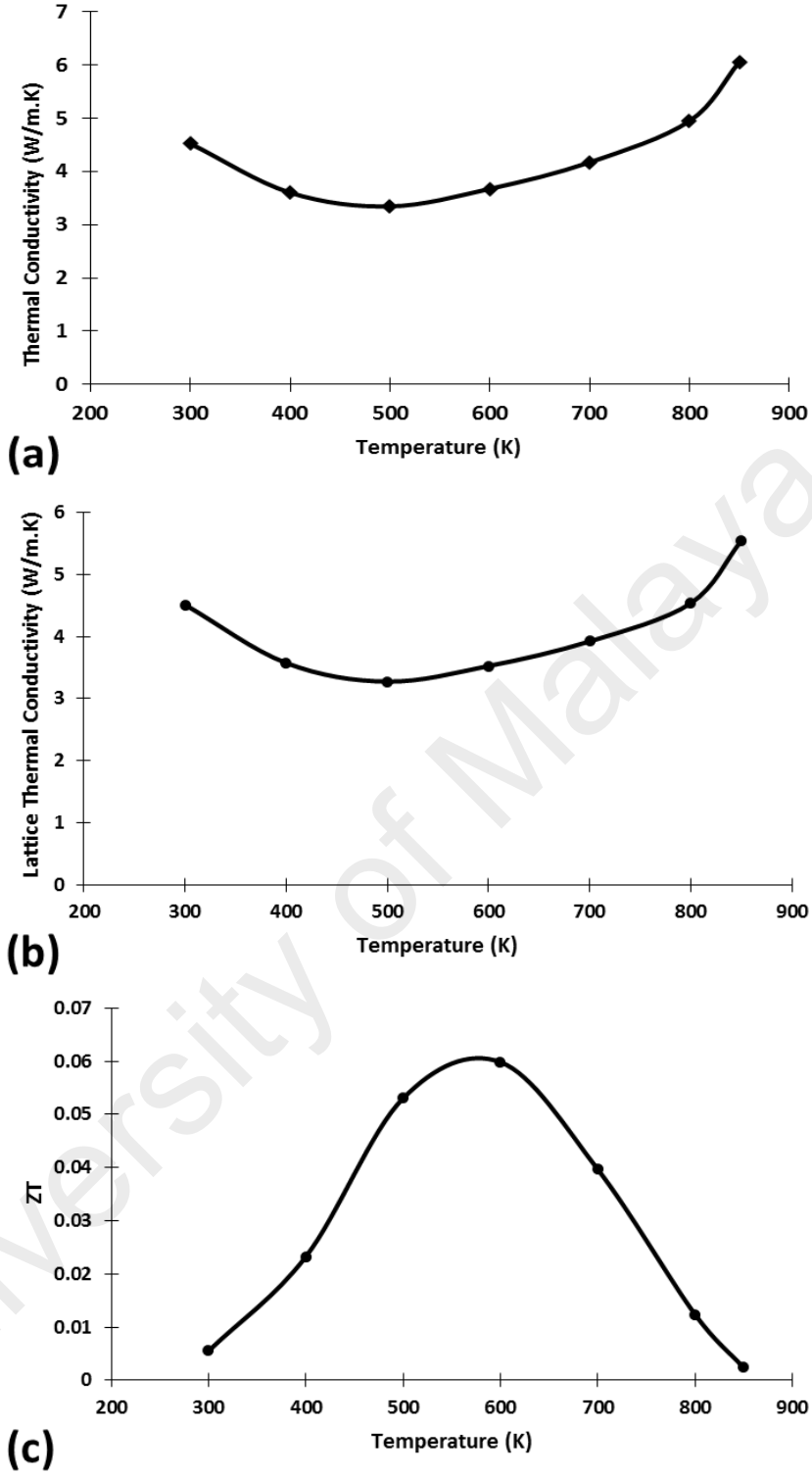

Figure 4.4: Temperature dependence of the (a) thermal conductivity, (b) lattice thermal conductivity, and (c) Figure of merit *ZT*.

4.1.3 Thermal behavior

Figure 4.5 indicates the thermal stability of the Mn-added $CoSb_3$ composition. The TGA thermograph in Figure 4.5(a) shows a great stability of the skutterudite phase up to 644 °C, at which point weight reduction begins to occur as a result of Sb sublimation. The total decomposition of the skutterudite phase was observed at 854 °C. The new resultant phases began to decompose at 921 °C. In Figure 4.5(b), the DSC thermograph contains only one endothermic peak, from which the onset melting point of the skutterudite phase was determined to be over 850 °C. The melting points of the residuals phases were indicated through the sub-endothermic peaks at 887 °C and 962 °C.

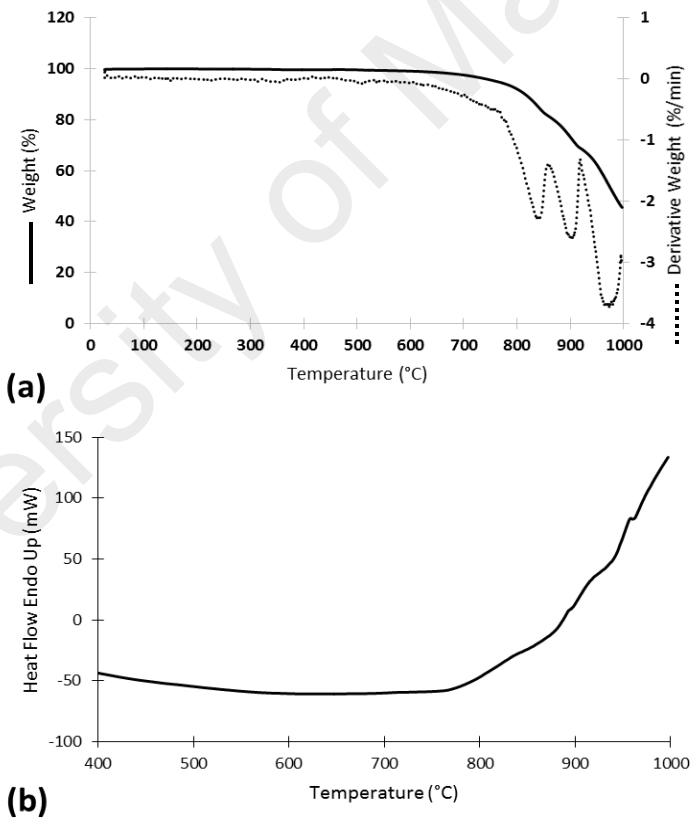

Figure 4.5: (a) TGA, and (b) DSC; thermographs upon heating of the Mn-added Co_4Sb_{12} composition.

4.1.4 Mechanical properties

To assess the homogeneity of the Mn-added $CoSb_3$ sample, micro-hardness was mapped on several cross-sections of the specimen. A homogeneous distribution of $HV_{0.1}$ values in the range of 622-632 was observed with no significant differences between the different regions of the sample's margins and interior area, thus emphasizing the suitability of the SPS process for producing dense samples with a uniform microstructure. Moreover, the addition of Mn to $CoSb_3$ increased the HV value of the binary skutterudite $CoSb_3$, which was reported by Recknagel et al. (2007) to be 608.

4.2 Hf-added $CoSb_3$ composition

Ongoing work to explore new filling species and evaluate their contribution to thermoelectric properties is greatly needed to fill in the knowledge gap for this type of thermoelectric material. Replacing the lanthanum cation by a cation with a smaller ionic radius and higher mass has been predicted to result in skutterudites with a thermal conductivity less than any thermal conductivity of a known thermoelectric material (Hornbostel et al., 1997; Nolas et al., 2005). Therefore, hafnium as a heavy atom element can work as an alternative loosely bonded filler element for the $CoSb_3$ skutterudite thermoelectric material. In this section, filling the voids of $CoSb_3$ skutterudite with Hf will be investigated. However, although the heavy atom elements tend to fill the voids of $CoSb_3$ without making secondary phases, some secondary phase formations are possible as a result of the fabrication process, for example. Yb_2O_3 and YbSb phases were formed in the skutterudite matrix of $Yb_{0.2}In_{0.2}Co_4Sb_{12}$ in the work of Ballikaya et al. (2012).

4.2.1 Microstructural properties

The MAed powders were strongly deformed and thermodynamically metastable as a result of the high impact of mechanical energy (Yang et al., 2006). After the SPS process,

a polycrystalline phase of filled-skutterudite with a small peak for HfO_2 as a secondary phase were obtained and are presented in the as-sintered XRD pattern shown in Figure 4.6. The crystal structure was refined using JANA2006. The lattice parameter was refined to be a = 9.03454(8) angstrom and the occupancy of Hf at 12d site was refined to be 0.0429(11), yielding the composition of $Hf_{0.514(13)}Co_8Sb_{24}$ ($Hf_{0.257}Co_4Sb_{12}$). The mass ratio of skutterudite and HfO_2 is refined to be 93.9(6) % and 6.1(4) %, respectively, as the strongest peak of HfO_2 is only observed at 2 theta = 28.2, as a broad peak.

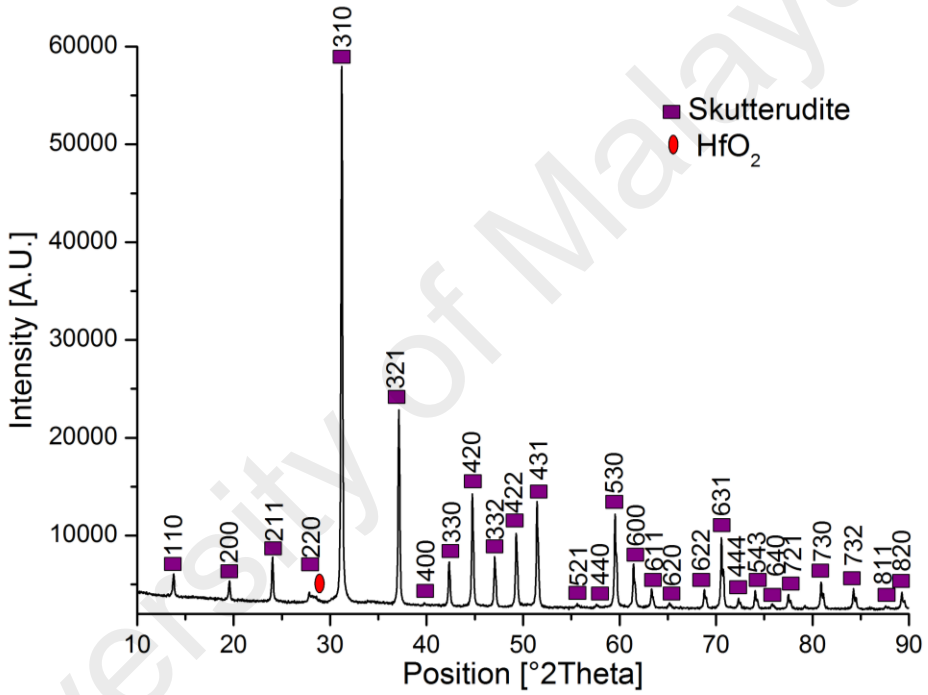

Figure 4.6: XRD pattern of the as-sintered sample of Hf-added Co_4Sb_{12}.

The actual density for the as-sintered sample was more than 99% of the calculated density. This relatively high density agrees with the small number of pores observed in the SEM micrograph image shown in Figure 4.7(a). The grains size was variable. The average size was 7 µm for the majority of the grains, and the presence of a few large grains with sizes up to 45 µm were observed. The composition of the grains and the grain boundaries were investigated by EDX. The atomic percent indicated that the Hf atoms

might partially fill the skutterudite voids inside the grains, whereas an excess amount of Hf atoms was detected in the grain boundaries. Furthermore, the elemental mapping shown in Figures 4.7(c,d,e) indicates that Hf takes on two microstructural modification roles within the skutterudite. Specifically, Hf distributes equally in the whole region of the grains and also agglomerates as Hf-rich regions at the edges of the grains or along the grain boundaries. This behavior agrees with that of the Pr-filling $CoSb_3$ discussed in the work of (Graff et al. (2014) and of the Bi-filling $CoSb_3$ discussed in the work by Mallik et al. (2013). However, the tendency of Hf to fill the voids of $CoSb_3$ has been confirmed in this study, although an excess amount of Hf was found to agglomerate in the grain boundaries. Therefore, a single phase of Hf-filled skutterudite could be obtained if the suitable fraction was used.

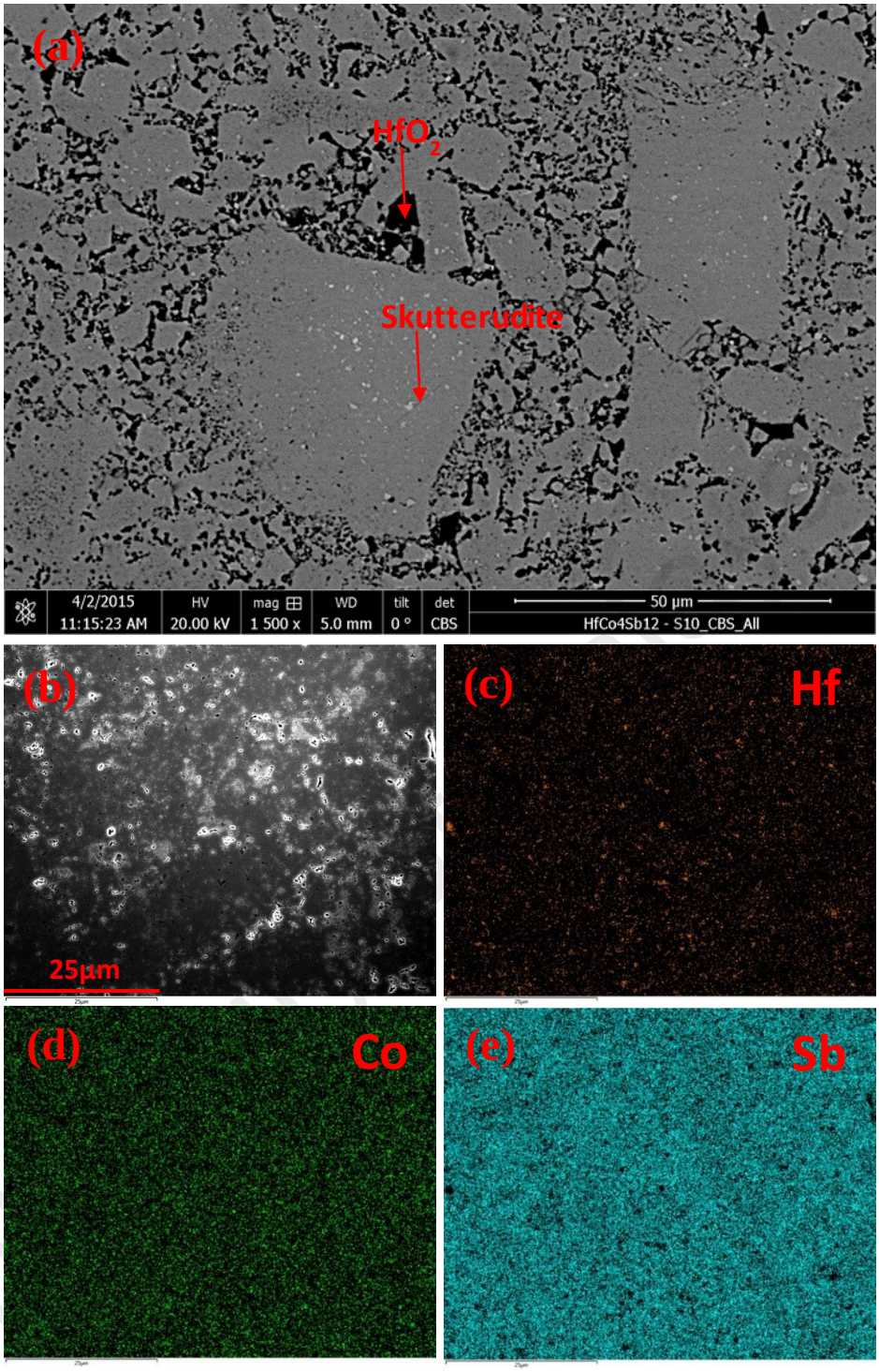

Figure 4.7: The SEM images of Hf-filled $CoSb_3$; (a) a micrograph of an SPS-compacted sample, and (b) a SEM/EDX micrograph; the elemental mapping of (c), (d), and (e) show Hf, Co, and Sb, respectively, extracted from (b) using EDX.

4.2.2 Thermoelectric properties

The electrical resistivity of the Hf-filled $CoSb_3$, at the measured temperature region (RT – 577 °C) shown in Figure 4.8(a) indicated a slight reduction from the electrical resistivity of the binary skutterudite $CoSb_3$ (Kawaharada et al., 2001). Essentially, due to its electronic structure in the composition, HfO_2 has less of an impact on the carrier concentration; therefore, the electrical resistivity remained high. The electrical resistivity decreased with increasing temperature, displaying a semiconducting behavior, which is a result of increasing the carrier concentration and excitation of the carriers across the band gap (Laufek et al., 2009).

Figure 4.8(b) shows the temperature dependence of the Seebeck coefficient (α) for the Hf-filled $CoSb_3$. A positive Seebeck coefficient was observed, indicating a p-type thermoelectric material. A tiny increase in value of α can be realized from RT to 150 °C, at which point there is a peak with a value of 153 μVK^{-1}; there is then a dramatic decrease from 150 °C to 550 °C, when the intrinsic effect of hafnium becomes active. The absolute value of the Seebeck coefficient of Hf-filled $CoSb_3$ is less than that of $CoSb_3$ (~225 μVK^{-1}) (Kawaharada et al., 2001). The power factor (*PF*) exhibits a parabola-like behavior (see Figure 4.8(c)) due to the reverse interrelationship between the Seebeck coefficient and the electrical conductivity. A maximum *PF* of 0.143×10^{-3} $Wm^{-1}K^{-2}$ was obtained at 300 °C.

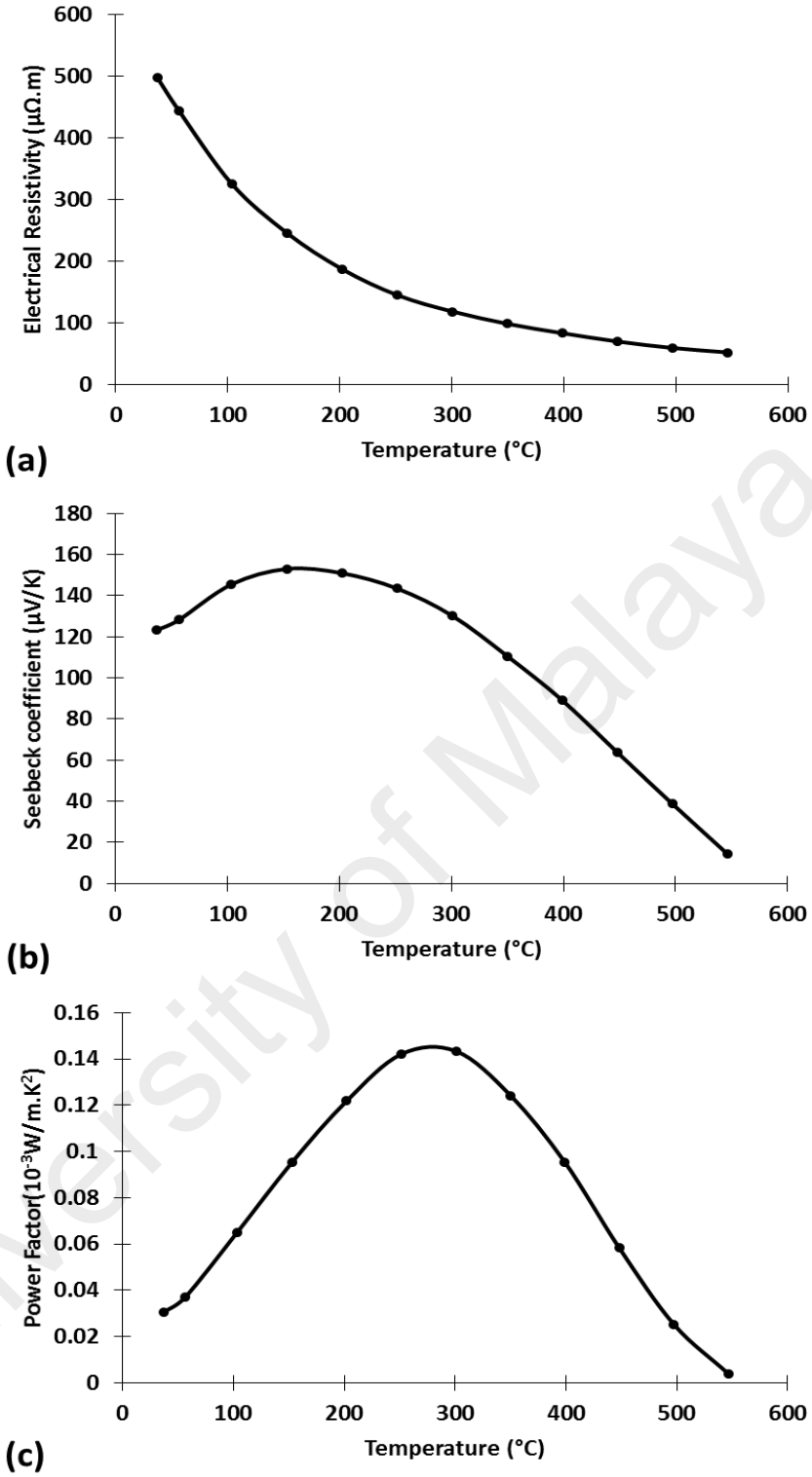

Figure 4.8: Temperature dependence of the (a) electrical resistivity, (b) Seebeck coefficient, and (c) power factor (PF).

Figure 4.9(a) shows the temperature dependence of the thermal conductivity (K). As illustrated, the thermal conductivity decreased with an increase in temperature up to 500 K, at which point K = 1.8 W/m.K (the minimum thermal conductivity of the $CoSb_3$ binary skutterudite is ~4.5 W/mK (Kawaharada et al., 2001)). For the most part, the phonon scattering tended to be forceful with the rise in temperature. However, the thermal conductivity increased gradually from 500 K to 850 K, indicating less phonon scattering from the rattling modes of the filling atoms.

The lattice thermal conductivity, K_L, can be estimated by subtracting the electronic contribution, $K_e = LT/\rho$, from the total thermal conductivity, where $L = 2.45 \times 10^{-8}$ V^2K^2 is the Lorenz number (Park & Kim, 2010). As shown in Figure 4.9(b), K_L is extremely suppressed compared with the lattice thermal conductivity of $CoSb_3$ reported by Zhang et al. (2015). The dramatic reduction of the thermal conductivity in the Hf-added skutterudite sample mainly comes from the oscillation of the loose bond. Principally, due to the anharmonicity of the oscillation of the guest atom, the phonon scattering could be increased. Likewise, the point defects on the lattice microstructure caused by nano-scale aggregations of Hf atoms and the large area fraction of the grain boundaries might be the reasons for the significant drop in the thermal conductivity of Hf-filled $CoSb_3$. Therefore, the disorder in the lattice structure caused by the addition of Hf was the reason for the increase in phonon scattering, hence decreasing the lattice thermal conductivity. Furthermore, the relative contribution of the electron thermal conductivity to the total thermal conductivity was negligible. It is therefore perceptible that Hf atoms are effective in reducing heat-carrying phonons. Consequently, Hf is a promising candidate for the multi-filling of $CoSb_3$ skutterudite, if used with one or more rare earth elements. However, a low ZT of 0.04 at 577 K, as shown in Figure 4.9(c), was found as a result of the high electrical resistivity, although the thermal conductivity was significantly reduced.

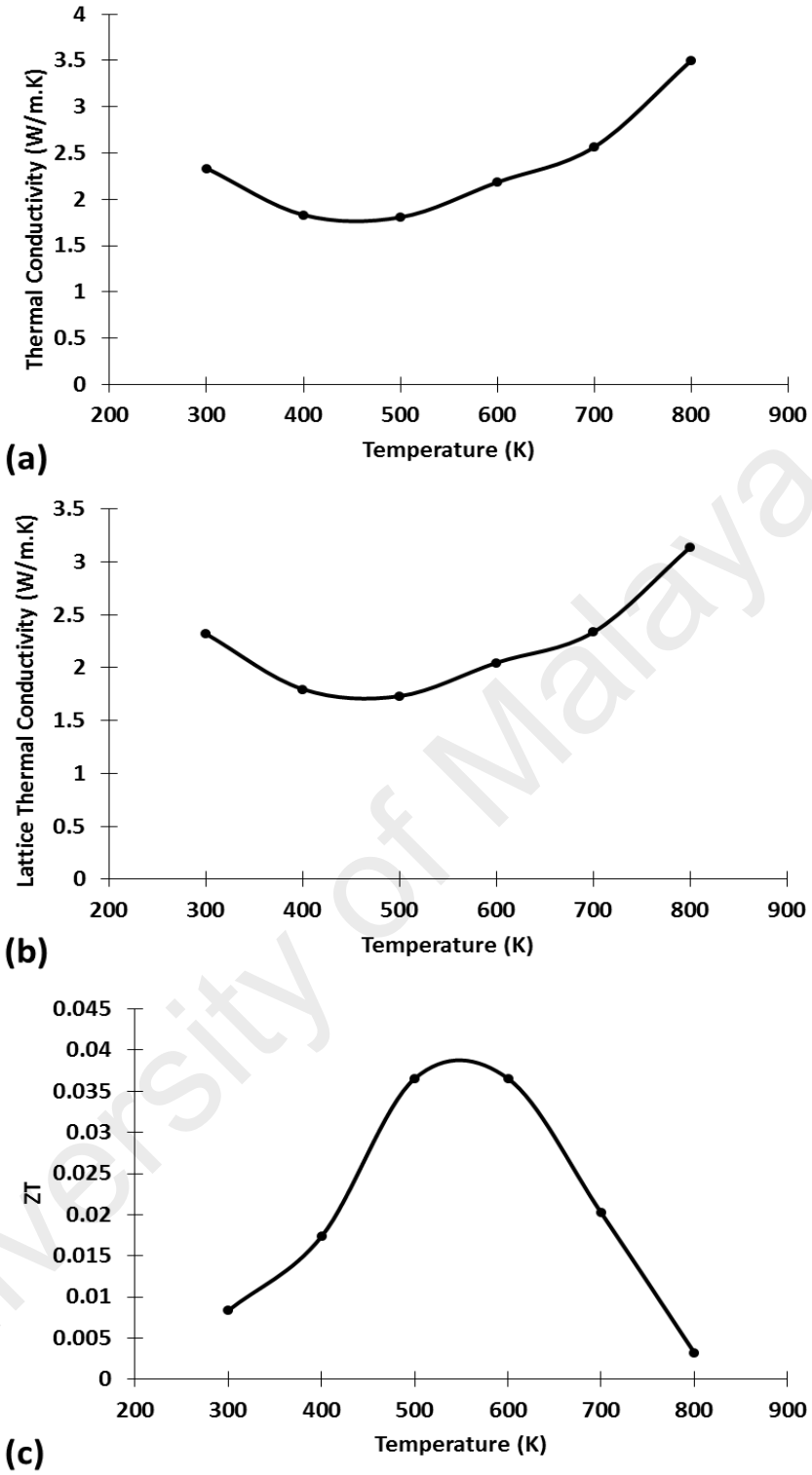

Figure 4.9: Temperature dependence of the (a) thermal conductivity, (b) lattice thermal conductivity, and (c) Figure of merit *ZT*.

4.2.3 Thermal behavior

Figure 4.10 shows the thermal stability of the Hf-added $CoSb_3$ composition. The TGA thermograph in Figure 4.10(a) shows the great stability of the skutterudite phase up to 645 °C, at which point weight reduction begins to occur as a result of Sb sublimation. The total decomposition of the skutterudite phase was observed at 866 °C. The new resultant phases began to decompose at 945 °C. From Figure 4.10(b), the DSC thermograph shows only one endothermic peak, from which the onset melting point of the skutterudite phase was determined to be over 800 °C. The melting point of the residual phase was indicated through the sub-endothermic peak at 910 °C.

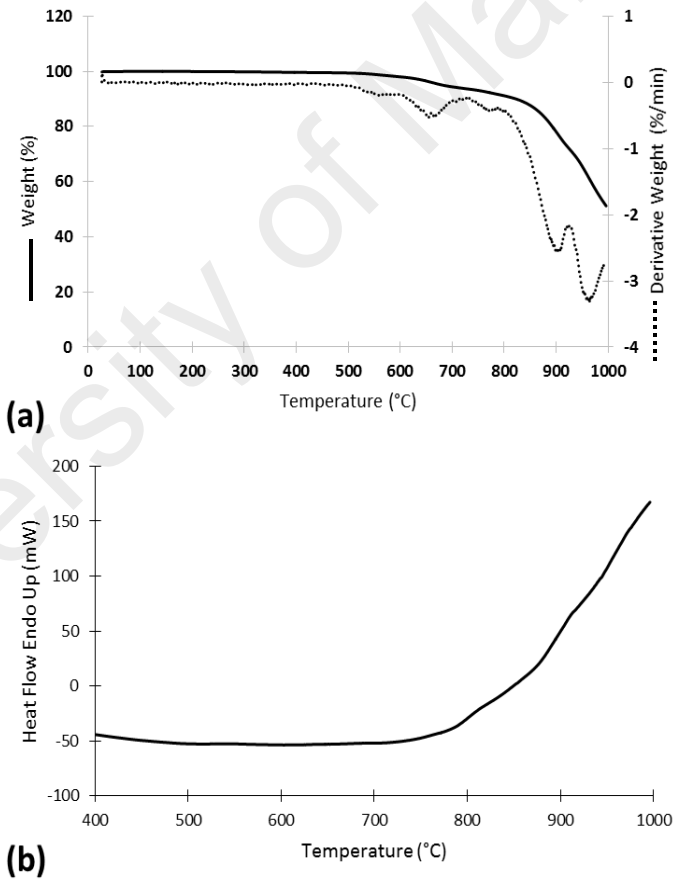

Figure 4.10: (a) TGA, and (b) DSC; thermographs upon heating of the Hf-added Co_4Sb_{12} composition.

4.2.4 Mechanical properties

To assess the homogeneity of the Hf-added $CoSb_3$ sample, micro-hardness was mapped on several cross-sections of the specimen. A homogeneous distribution of $HV_{0.1}$ values in the range of 362-366 was observed, with no significant differences between the different regions of the sample's margins and interior area, thus emphasizing the suitability of the SPS process for producing dense samples with a uniform microstructure. However, the addition of Hf to $CoSb_3$ significantly decreased the HV value of the binary skutterudite $CoSb_3$, which was reported by Recknagel et al. (2007) to be 608. This may be attributed to the increase in the area fraction of the grain boundaries from the addition of Hf.

4.3 Al_x-added $CoSb_3$ compositions (x = 0.3, 0.6, 2)

From the previous sections, transition elements were found to be very effective in reducing the thermal conductivity. Thus, in this work, the search for elements other than the alkaline earth metal and lanthanide elements to reduce the thermal conductivity of $CoSb_3$ skutterudite was extended to cover other metal elements such as Al. In this section, an excess amount of Al-doping was used to modify the grain boundary of the formulation. The accumulation of Al in the grain boundaries will serve to reduce the thermal conductivity of $CoSb_3$ skutterudite without affecting the electrical conductivity or Seebeck coefficient. Therefore, it is interesting to discuss the influence of dopants other than the alkaline earth metal and lanthanide elements on the structure of $CoSb_3$ skutterudite for a complete understanding of the crystal formation of this type of composition.

However, there are many factors affecting the formations of the ternary skutterudite matrix, such as the fabrication process, the stoichiometry of the elements in the

composition, and the ionic radius and atomic mass of the dopant. For example, the Te-doped $CoSb_3$ matrix in the work of Wojciechowski (2002) resulted in a Te-containing secondary phase. Later, Kim and Kim (2010) were able to obtain a single phase of skutterudite for Te-doped $CoSb_3$ with a slight modification of the fabrication process. Sn has been determined to fill the lattice voids of $CoSb_3$ and form a single phase of skutterudite in the work of Mallik et al. (2007), while, in a previous study by Kim et al. (2007) from same year, Sn was shown to occupy the Sb site and form a single phase of skutterudite that contained Sn in the mixture up to $CoSb_{2.6}Sn_{0.4}$; otherwise, Sn-containing secondary phases have been detected. Indium has shown promise as a skutterudite filler, which can form a single phase (Mallik et al., 2008) or in some cases a secondary phase of InSb (G. Li et al., 2012).

4.3.1 Microstructural properties

The XRD for as-sintered samples shown in Figure 4.11 indicates that the influence of the spark plasma sintering process on the metastable MA powders was very efficient. As a result, the MA powders were highly compacted to a polycrystalline skutterudite phase with different amounts of an AlSb secondary phase. The presence of AlSb was found to vary according to the amount of Al added to the Co_4Sb_{12} ($CoSb_3$) binary skutterudite system. The sharp peak of AlSb that appeared in the $Al_2Co_4Sb_{12}$ sample decreased with the decrease in aluminum addition. The lattice parameters fluctuated with the change in the amount of the Al addition in the structure of $Al_xCo_4Sb_{12}$ (x = 0.3, 0.6, 2), which were reported as 9.0385 Å, 9.0375 Å and 9.0394 Å, respectively. However, two alternative models can be predicted for Al-doped binary skutterudite: A: Al substituted for Sb in the 24g (0, y, z) site or B: Al filled the voids in the 2a (0, 0, 0) site.

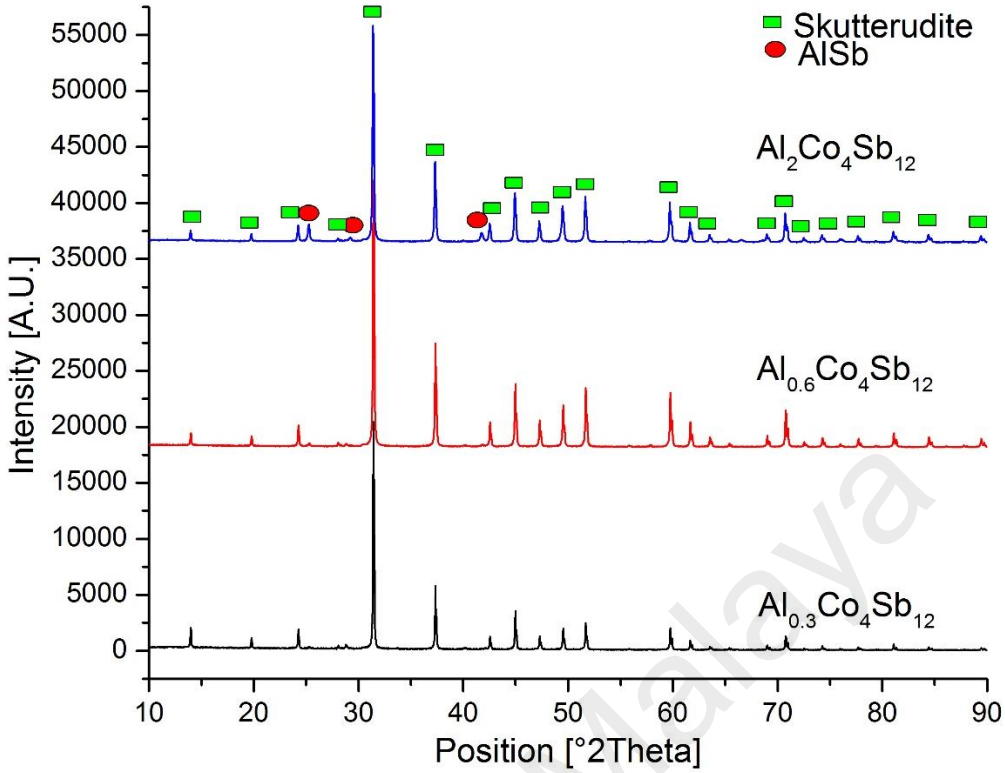

Figure 4.11: XRD patterns of the as-sintered sample of Al_x-added Co_4Sb_{12} (x = 0.3, 0.6, 2)

The SEM micrographs of the as-sintered samples of $Al_xCo_4Sb_{12}$ (x = 0.3, 0.6, 2) shown in Figure 4.12(a), Figure 4.13(a) and Figure 4.14(a), respectively, indicated very interesting surface topographies. The topographical feature of the $Al_{0.3}Co_4Sb_{12}$ sample was the formation of small grains with non-uniform grain boundaries. This feature was altered in the $Al_{0.6}Co_4Sb_{12}$ sample, which contained large grains surrounded by well-defined grain boundaries. In the $Al_2Co_4Sb_{12}$ sample, a combination of large and small grains was indicated. The shrinkage in the size of some grains can be attributed to the large grain boundaries that formed as a result of an excess amount of added Al. Generally, the size of the grain boundaries was proportional to the amount of Al added.

We verified the presence of the AlSb phase in the grain boundaries of all samples using SEM/EDX, and further investigation was performed on the $Al_{0.3}Co_4Sb_{12}$ sample using FIB/TEM. Moreover, elemental mapping was utilized to further investigate the microstructure and actual composition of the samples. The elemental mapping of the as-

sintered samples of $Al_xCo_4Sb_{12}$ (x = 0.3, 0.6, 2) shown in Figures 4.12(c, d, e), Figures 4.13(c, d, e), and Figures 4.14(c, d, e), respectively, clearly illustrates the distribution of the ternary system elements. The Co and Sb elements were distributed in a systematic order in the surface of the grains of the as-sintered samples, whereas the existence of Al inside the grains was shown to be less than 2 *wt* %. A strong presence of Al next to Sb in the grain boundaries was obtained. The presence of Al beside Sb in the grain boundaries agrees with the AlSb peak indicated in the XRD graph. The Al atoms appeared as rich spots in the grain boundaries of $Al_{0.3}Co_4Sb_{12}$ in Figure 4.12(c), which increased with the increasing amount of Al doping in $Al_{0.6}Co_4Sb_{12}$ in Figure 4.13(c). The clustering of the Al dopant at the edge of the grains and in the grain boundaries of the $Al_2Co_4Sb_{12}$ sample became very solid and almost fully enclosed the skutterudite grains (see Figure 4.14(c)).

If we look closer at the microstructure of the Al-doped $CoSb_3$ in Figure 4.15(a), we can realize that the grain boundaries contain of two types of small grains. The majority of these grains are shown to be skutterudite, as investigated by TEM/EDX, and these skutterudite grains have some small AlSb grains in between them, which gives an overview of the growth of AlSb in the grain boundaries. By increasing the Al doping, the small skutterudite grains in the grain boundaries could be replaced by AlSb grains. Figure 4.15(b) shows that different types of skutterudite small grains could be obtained in the grain boundary areas, such as fully crystallite grains (region A), polycrystalline grains (region B) and almost amorphous grains (region C). This can be attributed to the Al contained in the grain microstructure. As the amount of Al in the grain increased, the disorder of the lattice structure became higher. To determine the elemental distribution, EDX and elemental mapping were performed to extract the Al, Co and Sb from the area illustrated in the box frame of the image shown in Figure 4.15(c). The EDX result in Figure 4.15(d) showed an excess amount of Al with a satisfactory percentage of Co:Sb. The Cu indicated in the sample came from the cupper grid finger attached to the lamella.

The mapping of the elements shown in Figures 4.15(e, f, g) confirmed the presence of the AlSb phase, as expected. However, in recent studies, InSb clusters have appeared as a secondary phase in In-doped $CoSb_3$, rather than entering the Sb icosahedral voids, with demonstrated improvements in electrical performance and consequently TE efficiencies (Graff et al., 2011; Li et al., 2009; Peng et al., 2009). Therefore, we can conclude that Al doping is very effective in the lattice disorder of the skutterudite matrix and can be used to improve the thermoelectric properties of the skutterudite system, as well as other open structure systems.

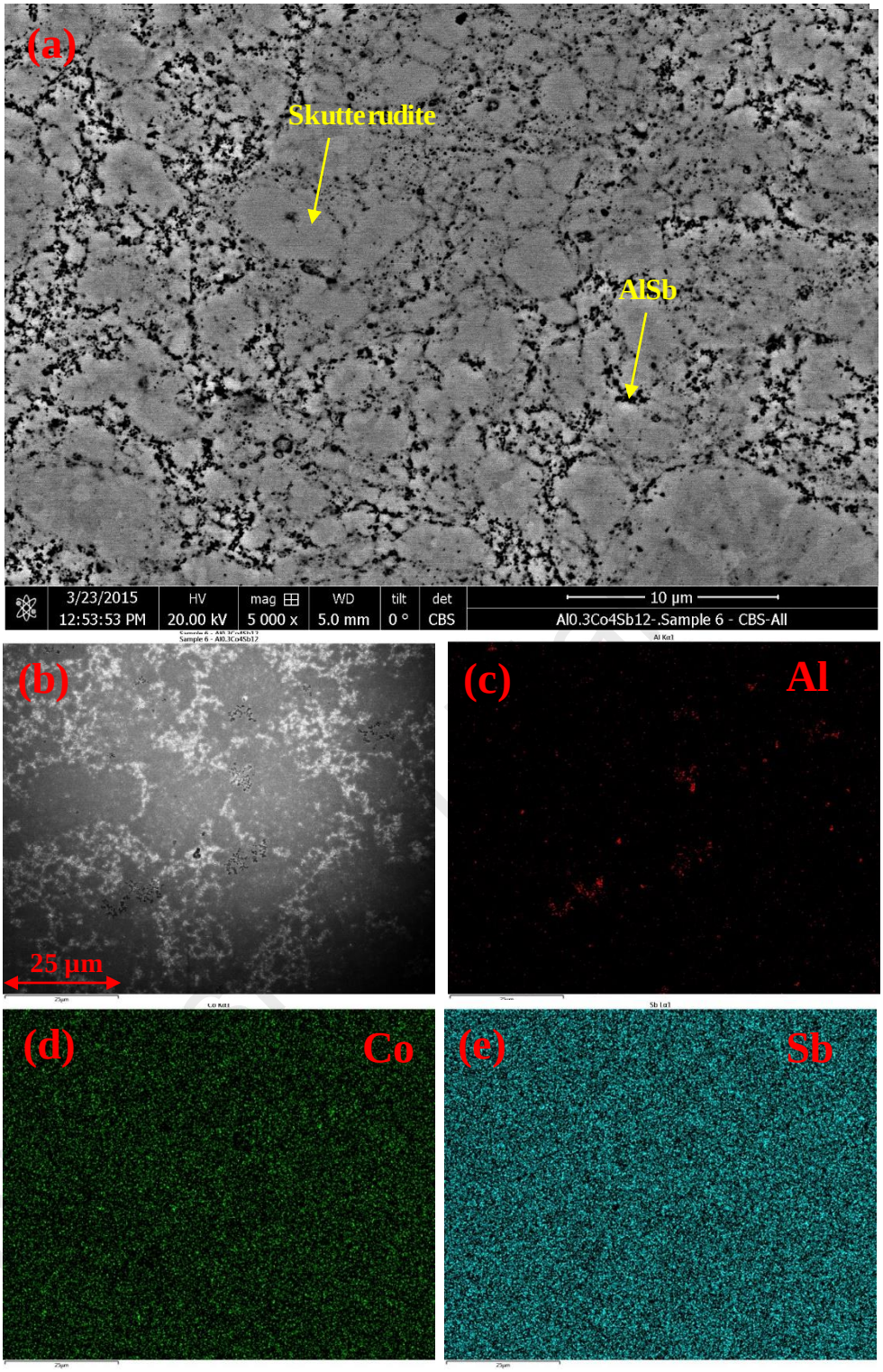

Figure 4.12: SEM images of $Al_{0.3}Co_4Sb_{12}$, (a) a micrograph of an SPS-compacted sample, and (b) an SEM/EDX micrograph; the elemental mapping of (c), (d), and (e) show Al, Co, and Sb, respectively, extracted from (b) using EDX.

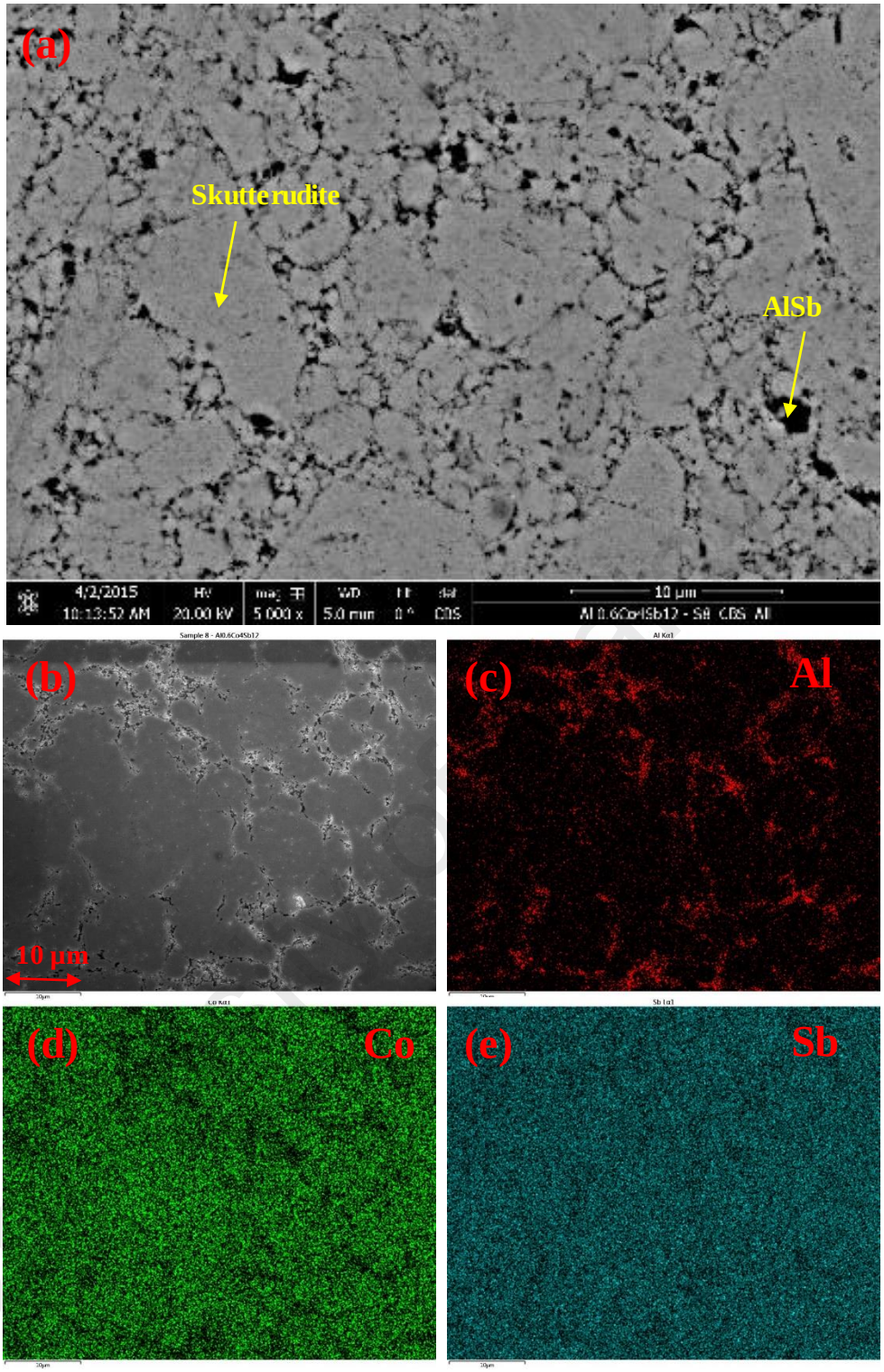

Figure 4.13: SEM images of $Al_{0.6}Co_4Sb_{12}$, (a) a micrograph of an SPS-compacted sample, and (b) an SEM/EDX micrograph; the elemental mapping of (c), (d), and (e) show Al, Co, and Sb, respectively, extracted from (b) using EDX.

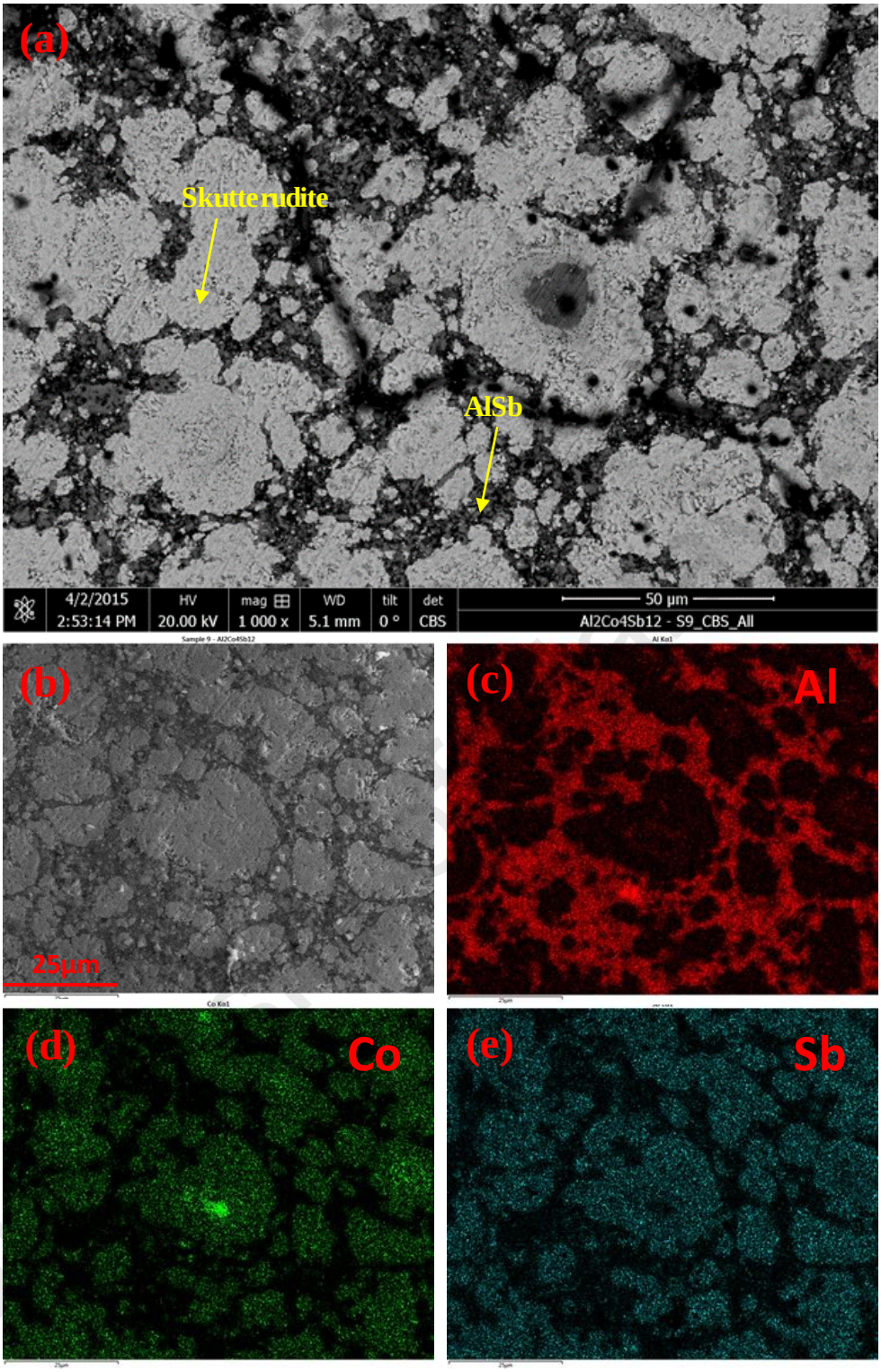

Figure 4.14: SEM images of $Al_2Co_4Sb_{12}$, (a) a micrograph of an SPS-compacted sample, and (b)an SEM/EDX micrograph; the elemental mapping of (c), (d), and (e) show Al, Co, and Sb, respectively, extracted from (b) using EDX.

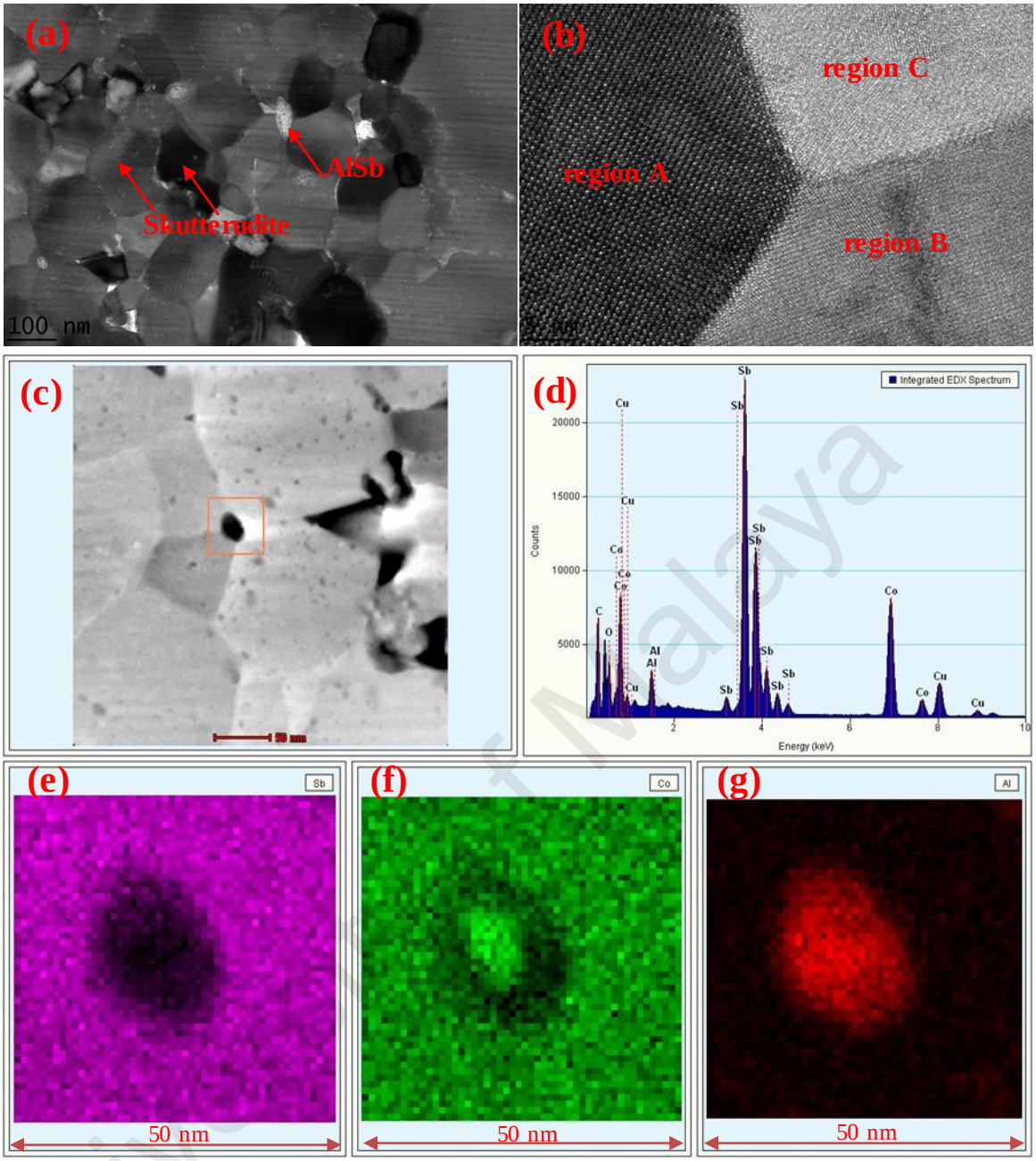

Figure 4.15: TEM images of $Al_{0.3}Co_4Sb_{12}$; (a) micrograph of an SPS-compacted sample at a magnification of 26.5KX; (b) micrograph of an SPS-compacted sample at a magnification of 530KX showing fully crystallite grains (region A), polycrystalline grains (region B) and almost amorphous grain (region C); (c) a TEM/EDX micrograph; (d) integrated EDX spectrum extracted from the box frame area in (c); the elemental mapping of (e), (f), and (g) show Sb, Co, and Al, respectively, extracted from the box frame area in (c) using the EDX.

4.3.2 Thermoelectric properties

The temperature dependence of electrical resistivity for the $Al_xCo_4Sb_{12}$ (x = 0.3, 0.6, 2) samples shown in Figure 4.16(a) demonstrated high electrical resistivity at room temperature for all compositions in comparison with the skutterudite system filled with heavy atoms, such as Yb (Li et al., 2009). The electrical resistivity of the compositions decreased with increasing temperature, indicating a semiconductor behavior over the entire temperature range for all samples. The most stable sample with the narrowest electrical resistivity range was the one with the highest amount of AlSb nano-inclusions in its composition, which was $Al_2Co_4Sb_{12}$. However, the high amount of impurities and defects that can be produced by nano-inclusions in the crystal lattice of the skutterudite matrix may cause new additional electronic states within the bandgap and act to trap the charge carriers. Therefore, most previous research has shown an increase in the average electrical resistivity as a result of introducing nano-inclusions in skutterudite compositions. Thus, this finding is novel in that is demonstrates a reversed and desirable behavior.

Figure 4.16(b) shows the temperature dependence of the Seebeck coefficient for $Al_xCo_4Sb_{12}$ (x = 0.3, 0.6, 2). Almost, similar pattern of temperature dependence of the Seebeck coefficient was recorded for the $Al_{0.6}Co_4Sb_{12}$ and $Al_2Co_4Sb_{12}$ samples. The highest Seebeck coefficient recorded for both of these samples was 218 µV/K and 198 µV/K at 127 °C, respectively. The positive sign that appeared in the Seebeck coefficient values for these two samples indicates p-type behavior. Unusual behavior of the temperature dependence of the Seebeck coefficient was observed for the $Al_{0.3}Co_4Sb_{12}$ sample. Thus, Seebeck coefficient crossover (n- to p-type) at a reverse point of 200 °C was recorded. The tiny deviation of the cooling curve from the heating curve at lower temperatures can be attributed to the relaxation time. Similar behavior was obtained by Kawaharada et al. (2001) for the ternary skutterudite $CoSb_3$ with added Bi. The nature of

p-type or n-type in misleading $CoSb_3$ can be attributed to the chemical purity of the starting material, as contaminations may introduce dopants. A slight lack of Sb leads to n-type conductivity, while a lack of Co leads to p-type conductivity. The transition from negative to positive values of the Seebeck coefficient is usually observed in the $CoSb_3$ samples that are uncompensated at the Sb site. In general, a transition occurs when the carrier type changes from being weakly extrinsic to intrinsic due to an increased temperature (Mallik et al., 2013).

However, regarding the $Al_{0.3}Co_4Sb_{12}$ composition, Table 4.2 shows that the electron concentration (n), as well as the hall mobility (μ_H), decreased with increasing temperature up to 127 °C, and the contribution of holes increased as the sign changed from negative to positive at 177 °C. Therefore, the sample exhibited p-type behavior after 200 °C as a result of the increasing hole concentration with the increase in temperature. In Figure 4.6(b), the Seebeck curves were almost identical upon heating and cooling. Thus, this behavior can be attributed to the change in the spin status of Co(III) from low spin (LS) to high spin (HS). XPS was used to determine the chemical state of Co, and, at room temperature, the composition contained 64% Co(II) and 36% Co(III). In situ HT-XRD was used to determine the change in the bond length of Co-Sb as a function of temperature, and the bond length of Co-Sb increased from 2.519 Å at room temperature to 2.523 Å at 200 °C. Thus, in this SCO composition, an external heat source is proposed to drive the following transition:

$$\xleftrightarrow{\text{RT – 200 °C}} \quad \text{HS Co(II) + LS Co(III)} \underset{\text{Cooling}}{\overset{\text{Heating}}{\rightleftarrows}} \text{HS Co(II) + HS Co(III)} \quad \xleftrightarrow{\text{200 – 527 °C}}$$

Moderate power factors were reported for $Al_xCo_4Sb_{12}$ (x = 0.3, 0.6, 2), as shown in Figure 4.16(c). The highest power factor of 0.41×10^{-3} W/m.K^2 belonged to the $Al_{0.3}Co_4Sb_{12}$ sample at 377 °C. A small reduction of this value was realized at 0.40×10^{-3}

W/m.K^2 for the $Al_{0.6}Co_4Sb_{12}$ sample at a lower temperature of 327 °C . With the increase in the amount of Al added to the $Al_2Co_4Sb_{12}$ sample, the maximum power factor value decreased to 0.34×10^{-3} W/m.K^2 at a medium temperature of 277 °C.

Table 4.2: Temperature dependent transport properties of $Al_xCo_4Sb_{12}$ (x = 0.3, 0.6, 2).

Temperature [°C]	**Carrier Density [1/cm^3]**	**Mobility [cm^2/(V.S)]**
27	-1.20E+18	-1.42E+01
77	-2.27E+17	-2.44E+01
127	-3.80E+14	-8.81E-02
177	1.01E+13	6.87E+00
227	3.99E+13	9.84E-01

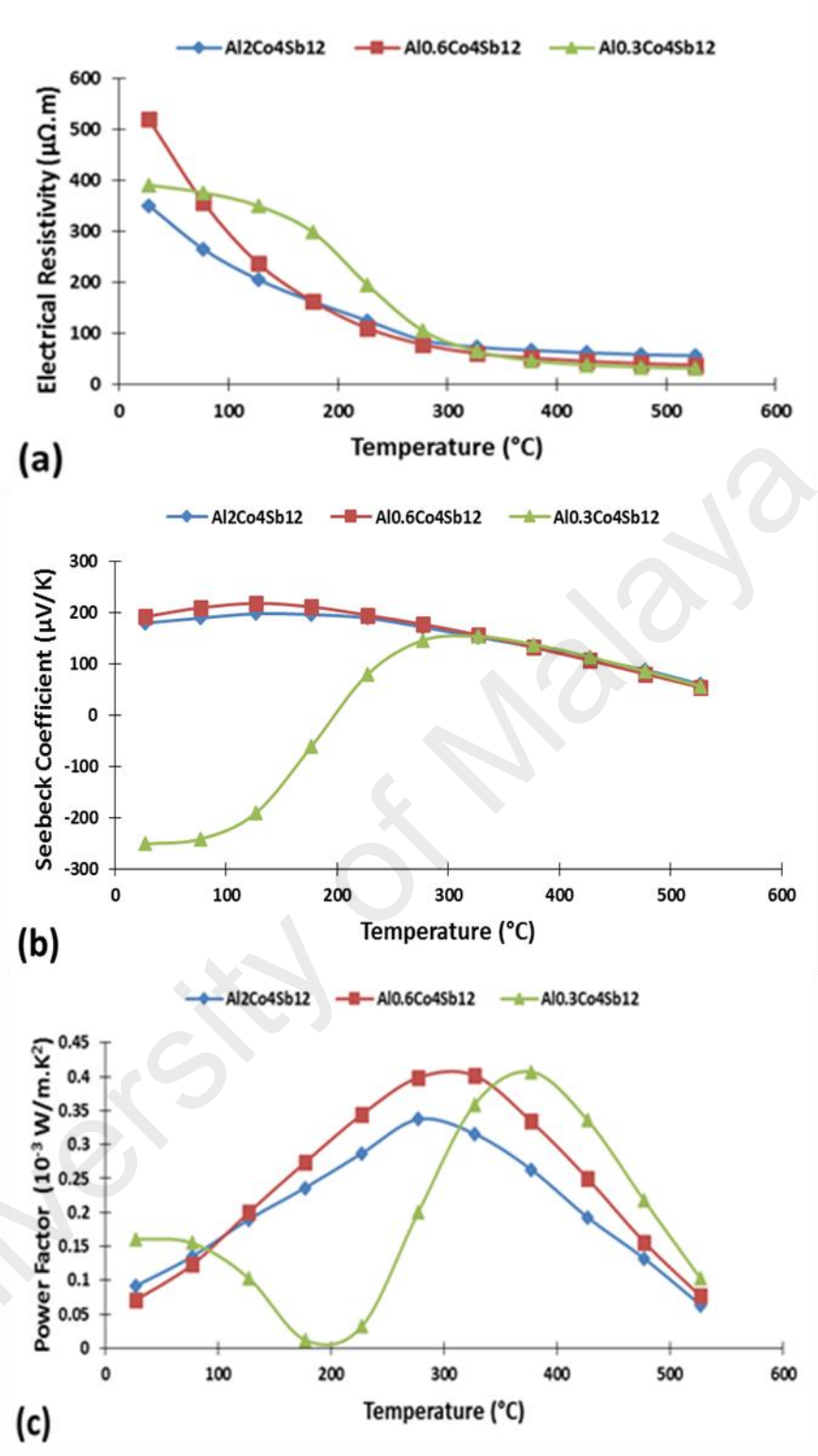

Figure 4.16: Temperature dependence of the (a) electrical resistivity, (b) Seebeck coefficient, and (c) power factor (PF) for $Al_xCo_4Sb_{12}$ (x = 0.3, 0.6, 2) compositions.

In Figure 4.17(a) the temperature dependence of the thermal conductivity (K) was demonstrated for $Al_xCo_4Sb_{12}$ (x = 0.3, 0.6, 2). The minimum thermal conductivity (K_{min} for all samples was recorded at elevated temperatures. The K_{min} for the $Al_{0.3}Co_4Sb_{12}$ sample was found to be 4.6 W/m.K at 600 K, whereas this value decreased significantly for the $Al_{0.6}Co_4Sb_{12}$ sample to 3.3 W/m.K at 500 K. The most significant reduction in K of 2.7 W/m.K was obtained for the sample with a high Al content, which was $Al_2Co_4Sb_{12}$. The lattice thermal conductivity, K_L, can be estimated by subtracting the electronic contribution of the Wiedemann-Franz law, $K_e = LT/\rho$, from the total thermal conductivity, where $L = 2.45 \times 10^{-8}$ V^2K^2 is the Lorenz number (Park & Kim, 2010). As shown in Figure 4.17(b), K_L was suppressed by a tiny amount for all samples compared with the K_L of the skutterudite $CoSb_3$ filled with heavy elements. Therefore, the minimum K_L values were 4.4 W/m.K, 3.2 W/m.K and 2.6 W/m.K at 600 K, 500 K and 500 K for Al_x (x = 0.3, 0.6, 2), respectively. The electronic contribution K_e had a negligible effect on the total thermal conductivity in this system. However, the addition of Al to the binary skutterudite $CoSb_3$ resulted in a decrease in the thermal conductivity of ~45% for the $Al_2Co_4Sb_{12}$ composition compared with the binary skutterudite $CoSb_3$ discussed in the work of Kawaharada et al. (2001).

Composites of $Al_xCo_4Sb_{12}$/AlSb demonstrated a high electrical resistivity, a high Seebeck coefficient and a relatively low lattice thermal conductivity. Therefore, the high electrical resistivity contributed to low figures of merit ZTs of 0.047, 0.066 and 0.061 at one operating temperature of 600 K (see Figure 4c) for $Al_xCo_4Sb_{12}$ (x = 0.3, 0.6, 2), respectively.

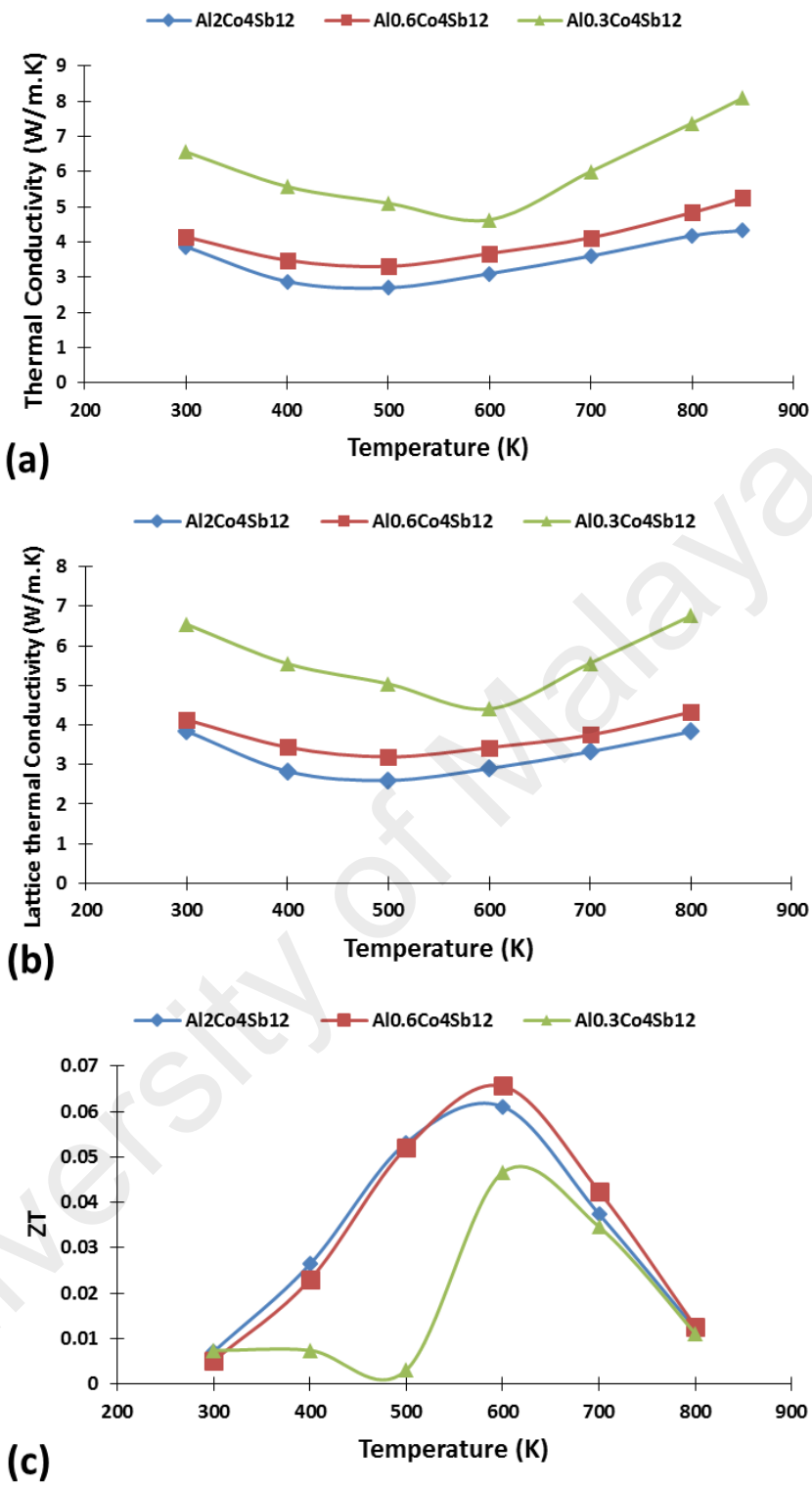

Figure 4.17: Temperature dependence of the (a) thermal conductivity, (b) lattice thermal conductivity, and (c) Figure of merit *ZT* for $Al_xCo_4Sb_{12}$ (x = 0.3, 0.6, 2) compositions.

4.3.3 Thermal behavior

Figures 4.18 and 4.19 show the thermal stability of Al_x-added $CoSb_3$ compositions (x = 0.3, 0.6, 2). The TGA thermograph in Figure 4.18(a) shows the great stability of the x = 0.3 composition up to 400 °C, at which point weight gain began up to 534 °C as a result of oxidation. Then, a rapid weight loss can be observed from 534°C to 600 °C, attributed to the sublimation of impurities in the starting materials and/or the evaporation of moisture gained during sample preparation for STA. The sublimation of Sb began to occur from 644 °C and was associated with weight reduction until 827 °C, at which point the decomposition of the skutterudite phase was observed. The new resultant phases began to decompose immediately at 854 °C. From Figure 4.18(b), no oxidation behavior was observed up to 520 °C for the x = 0.6 composition. From 520 °C to 564 °C, a small decrease in weight can be observed, attributed to the sublimation of impurities in the starting materials and/or the evaporation of the moisture gained during sample preparation for STA. At 634 °C, the sublimation of Sb began to occur and was associated with weight reduction until 839 °C, at which point the decomposition of the skutterudite phase was observed. In the x = 2 composition shown in Figure 4.18(c), great thermal stability was realized up to 647 °C, at which point the sublimation of Sb began to occur, leading to gradual weight loss up to 847 °C. Above 847 °C, rapid weight loss was indicated and attributed to decomposition of the skutterudite phase. It can be concluded that the thermal stability increased significantly with increasing amounts of added Al.

In Figure 4.19, the DSC thermograph shows one endothermic peak, which indicates the melting points for the x = 0.3, 0.6 and 2 compositions. The onset melting point of x = 0.3 and 0.6 was observed to be over 800 °C (see Figures 4.19(a) and 4.19(b)), which can be attributed to the skutterudite phase. However, in the x = 2 composition (see Figure 4.19(c)), there is no indication of a clear onset melting point of the skutterudite phase, although a small endothermic peak was observed at 911 °C for the AlSb phase.

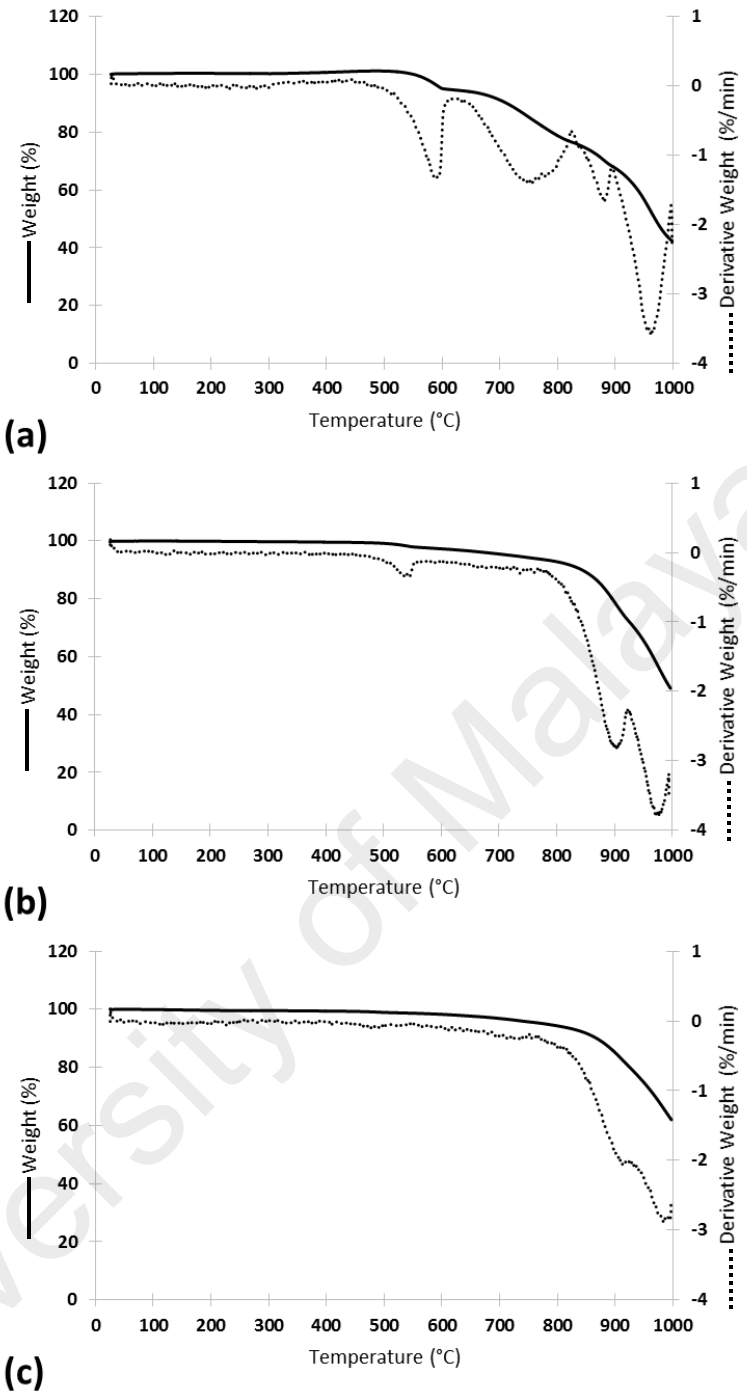

Figure 4.18: TGA thermographs upon heating of Al_x-added Co_4Sb_{12} compositions: (a) x = 0.3, (b) x = 0.6, and (c) x = 2.

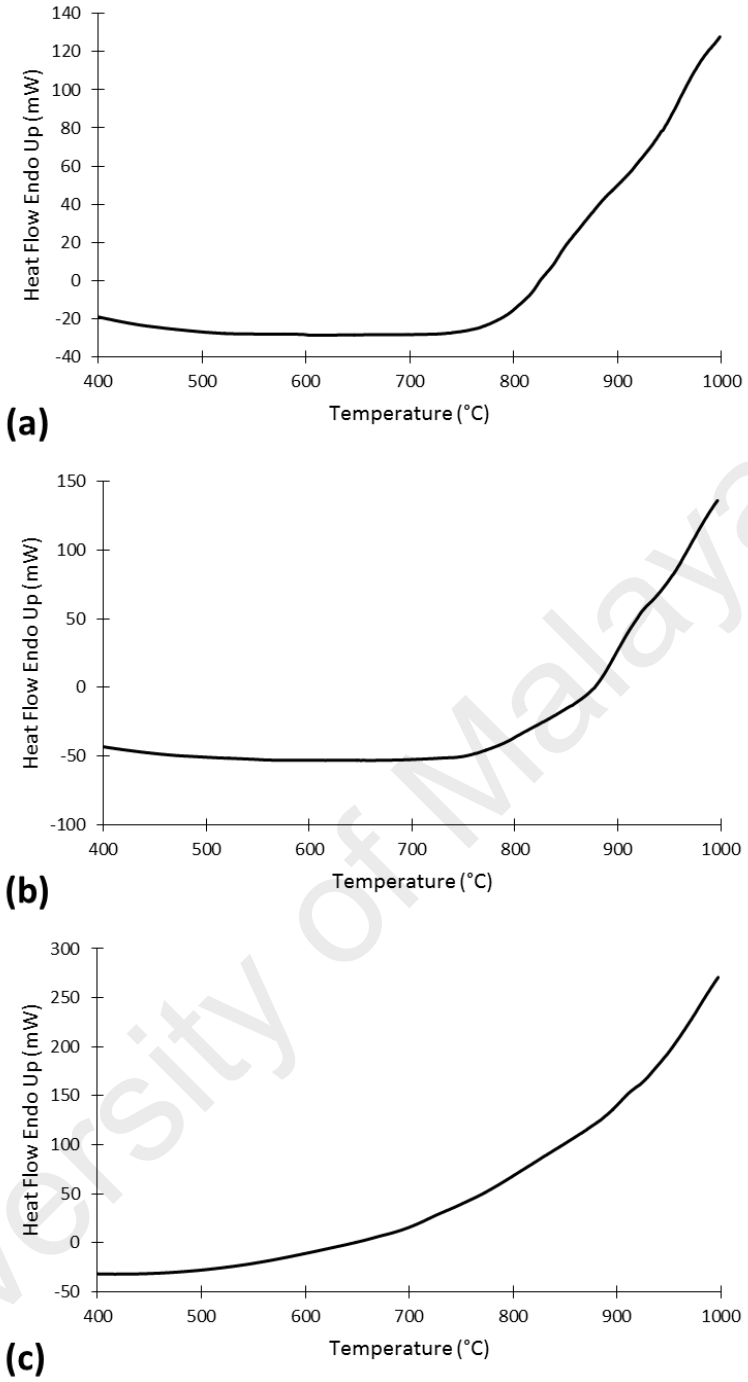

Figure 4.19: DSC thermographs upon heating of the Al_x-added Co_4Sb_{12} compositions: (a) x = 0.3, (b) x = 0.6, and (c) x = 2.

4.3.4 Mechanical properties

To assess the homogeneity of the Al_x-added $CoSb_3$ samples (x = 0.3, 0.6, 2), micro-hardness was mapped on several cross-sections of the specimens. A homogeneous distribution of $HV_{0.1}$ with average values of 499, 469, and 436 was observed for the Al_x-

added $CoSb_3$ compositions (x = 0.3, 0.6, 2), respectively. There were no significant differences between the different regions of the samples' margins and interior areas, thus emphasizing the suitability of the SPS process for producing dense samples with a uniform microstructure. However, the addition of Al to $CoSb_3$ significantly decreased the HV value of the binary skutterudite $CoSb_3$, which was reported by Recknagel et al. (2007) to be 608. Furthermore, with the increase in the amount of added Al, the value of $HV_{0.1}$ decreased. This may be attributed to the increase in the area fraction of the grain boundaries with the increase in the added Al.

4.4 Al_x-added $Yb_{0.}25Co4Sb12$ compositions (x = 0.1, 0.2, 0.3)

From the previous section, the excess amount of Al in the grain boundaries of the $CoSb_3$ binary skutterudite has shown promise in improving the thermoelectric performance by reducing the thermal conductivity without any major effects on the electrical conductivity or the Seebeck coefficient. Therefore, the doping of $CoSb_3$ with Al beside heavy atom elements from lanthanide group to improve the transport properties is expected to significantly improve the thermoelectric performance of the skutterudite system. Thus, in this section, Al addition to the $Yb_{0.25}Co_4Sb_{12}$ ternary skutterudite matrix will be investigated.

It is interesting to discuss other similar structures for a deep understanding of the crystal formation of this type of composition. However, there are many possibilities of forming secondary phases in the skutterudite samples in relation to either the fabrication process or to the non-stoichiometric ratios of the elements in the composition. For example, $Yb_{0.2}Co_4Sb_{12}$ sintered by SPS and discussed by Li et al. (2009) showed a small amount of $CoSb_2$ impurity, as a result of the short sintering time (5 min), in which the phase transition was not completely accomplished. The same composition investigated

by Peng et al. (2009) showed a single phase of skutterudite when sintered for 20 min. However, the pre-sintering process plays an important role in the purity of the skutterudite phase; for example, the mechanical alloying process may cause some elements in the composition to form an oxidized secondary phase. Moreover, sublimation of some elements during the melting or sintering processes and the formation of secondary phases in the skutterudite matrix are possible causes of deviations in the nominal and actual stoichiometry; i.e., Yb_2O_3, YbSb and InSb phases were formed in the skutterudite matrix of $Yb_{0.2}In_{0.2}Co_4Sb_{12}$ in the work of Ballikaya et al. (2012).

4.4.1 Microstructural properties

The XRD of the as-sintered samples shown in Figure 4.20 indicates that the influence of the spark plasma sintering process on the metastable MA powders was very efficient. As a result, the MA powders were highly compacted to a polycrystalline skutterudite phase with a very small amount of an AlSb secondary phase. The presence of AlSb was found to vary according to the amount of Al added to the $Yb_{0.25}Co_4Sb_{12}$ ternary skutterudite system. The AlSb peak that appeared in the $Al_{0.1}Yb_{0.25}Co_4Sb_{12}$ sample increased in the $Al_{0.2}Y_{0.25}Co_4Sb_{12}$ sample to record a higher AlSb content among all samples. However, increasing the amount of Al added in the $Al_{0.3}Yb_{0.25}Co_4Sb_{12}$ sample caused the peak of the AlSb secondary phase to almost disappear. This result might be attributed to the microstructure of the samples that formed during the SPS process, which can be further elucidated by the SEM and EDX characterizations. However, the small diffraction peak of AlSb indicates that a solid solution of Al in the lattice could be present. Therefore, the lattice parameters were changed accordingly with the change in the amount of the AlSb phase in the structure of $Al_xY_{0.25}Co_4Sb_{12}$ (x = 0.1, 0.2 and 0.3), which was 9.0471 Å, 9.0506 Å and 9.0475 Å, respectively. The volume fractions of AlSb in the lattice were estimated using HighScore Plus software. The software indicated that less than 0.1 *wt*. % of AlSb formed in all samples and the major phase was skutterudite.

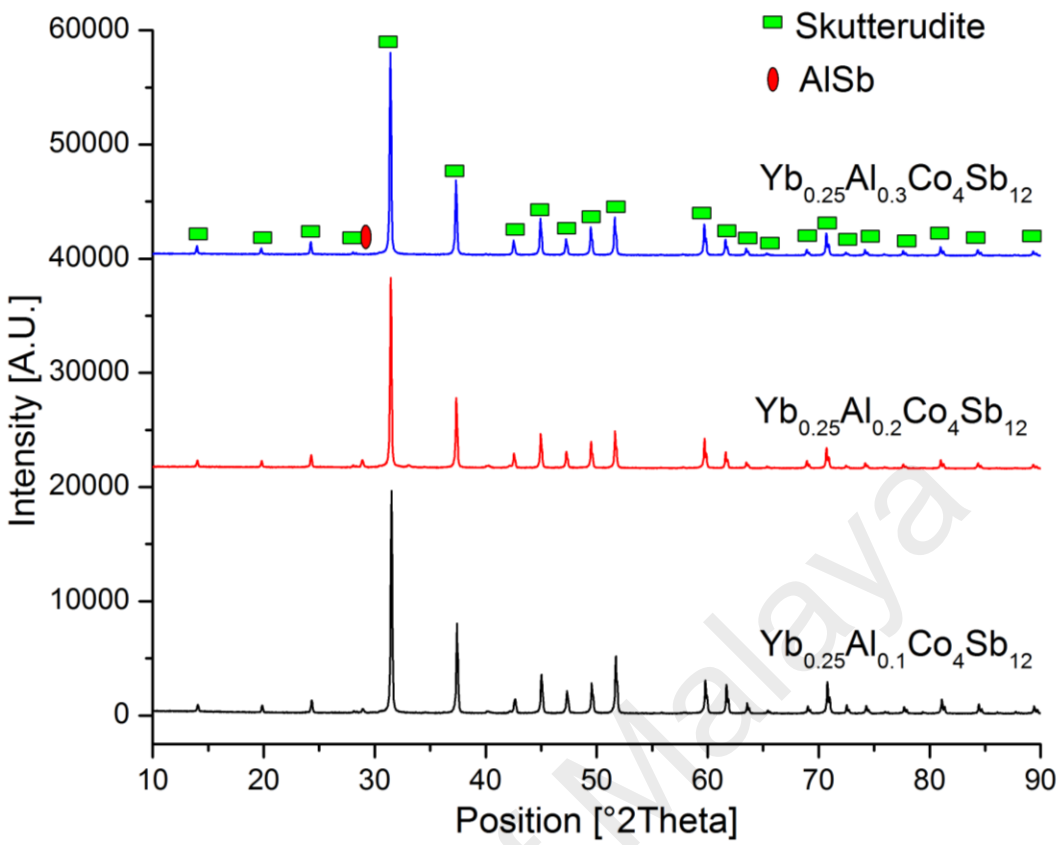

Figure 4.20: XRD patterns of the as-sintered sample of Al_x-added $Yb_{0.25}Co_4Sb_{12}$ (x = 0.1, 0.2, 0.3).

The SEM micrographs of the as-sintered samples of $Al_xYb_{0.25}Co_4Sb_{12}$ (x = 0.1, 0.2 and 0.3) shown in Figure 4.21(a), Figure 4.22(a) and Figure 4.23(a), respectively, indicate two types of surface topographies. The first topography involves an aggregation of grains in the form of solid islands with very narrow grain boundaries. The second topography involves the formation of individual grains surrounded by relatively wide grain boundaries. These grain islands varied in terms of quantity and size according to the amount of Al added. The number of grain islands decreased with the increase in the amount of Al added associated with a shrinkage in size. Therefore, the presence of more individual grains was realized. Moreover, the average size of the individual grains decreased linearly with the evolution of new individual grains caused by the addition of Al. Thus, small grains with a large area fraction of grain boundaries might lead to a

scattering of the Al atoms among the grain boundaries and hence reduce the possibility of the formation an AlSb phase. This phenomenon could be the reason behind the reduction of the AlSb peak observed in the XRD analysis of $Al_{0.3}Yb_{0.25}Co_4Sb_{12}$.

The presence of an AlSb phase was verified in the grain boundaries of all samples using SEM/EDS. Moreover, elemental mapping was utilized to further investigate the microstructure and actual composition of the samples. The elemental mapping of the as-sintered samples of $Al_xYb_{0.25}Co_4Sb_{12}$ (x = 0.1, 0.2 and 0.3) shown in Figures 4.21(c, d, e, f), Figures 4.22(c, d, e, f) and Figures 4.23(c, d, e, f), respectively, clearly illustrates the distribution of the quaternary system elements. Yb, Co and Sb were distributed in a systematic order in the surface of the grains of the as-sintered samples, whereas Al was less present inside the grains but had a strong presence in the grain boundaries beside Sb. This result may confirm that the skutterudite phase indicated by XRD belongs to the formation of a filled-skutterudite phase in the grains partially filled by Yb atoms. Moreover, the presence of Al beside Sb in the grain boundaries agrees with the AlSb peak indicated in the XRD graph. The Al atoms that appeared as rich spots in the grain boundaries of $Al_{0.1}Yb_{0.25}Co_4Sb_{12}$ in Figure 4.21(c) tend to scatter among the wide grain boundaries of $Al_{0.2}Yb_{0.25}Co_4Sb_{12}$ in Figure 4.22(c). The scattering of Al atoms reached their maximum mode in $Al_{0.3}Yb_{0.25}Co_4Sb_{12}$ in Figure 4.23(a), when the area fraction of the grain boundaries increased as a result of the production of new grains associated with the shrinkage of the average grain size. Thus, a very tiny amount of Al-rich aggregates in the grain boundaries of $Al_{0.3}Yb_{0.25}Co_4Sb_{12}$ in Figure 4.23(c) were detected. However, in recent studies, InSb clusters have appeared as a secondary phase in In-doped $CoSb_3$, rather than entering the Sb-icosahedral voids, with demonstrated improvements in electrical performance and consequently TE efficiencies (Graff et al., 2011; Li et al., 2009; Peng et al., 2009).

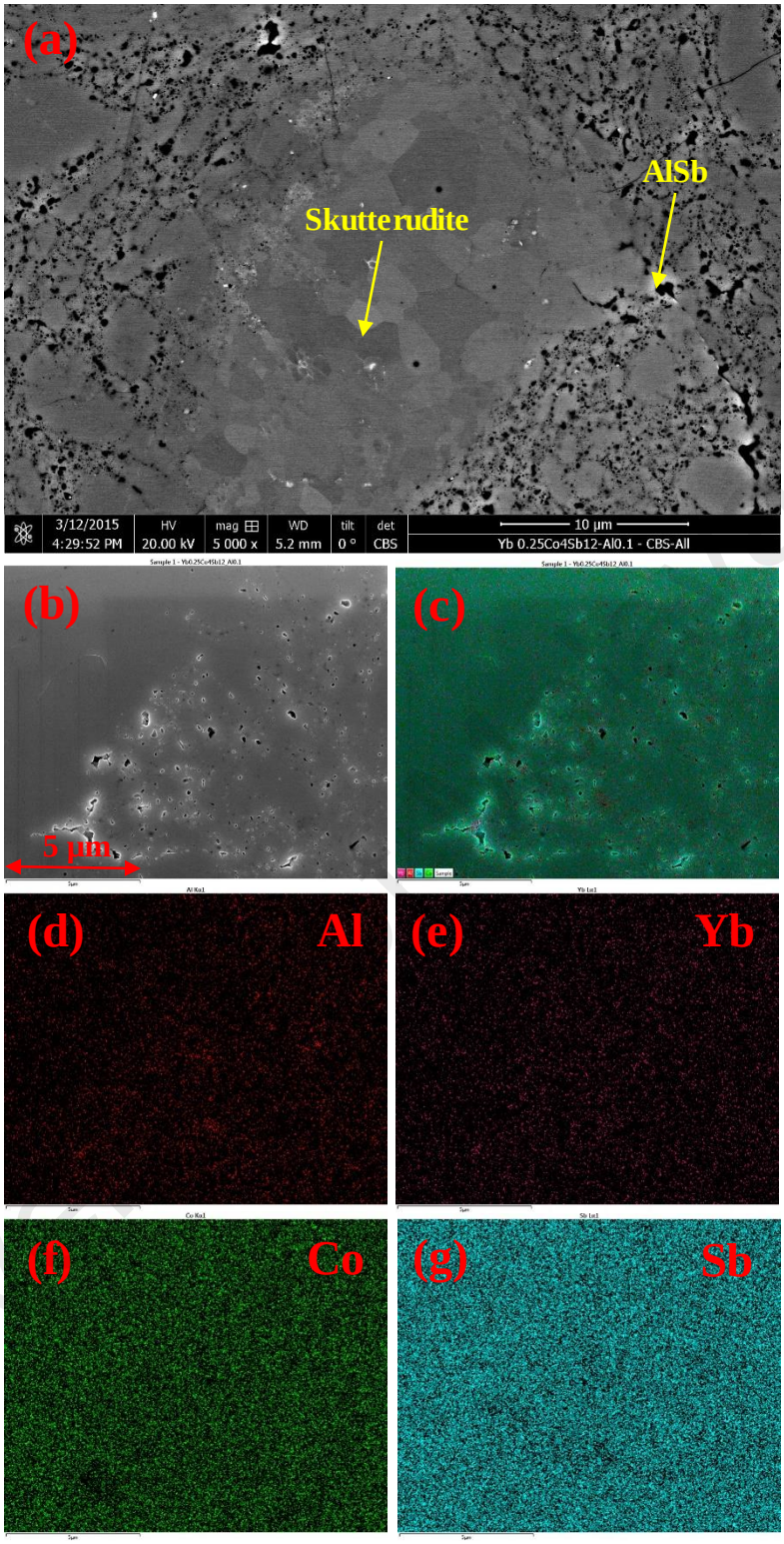

Figure 4.21: SEM images of $Al_{0.1}Yb_{0.25}Co_4Sb_{12}$, (a) a micrograph of an SPS-compacted sample, (b) an SEM/EDX micrograph, and (c) integrated elemental mapping; the elemental mapping of (d), (e), (f) and (g) show Al, Yb, Co, and Sb, respectively, extracted from (b) using EDX.

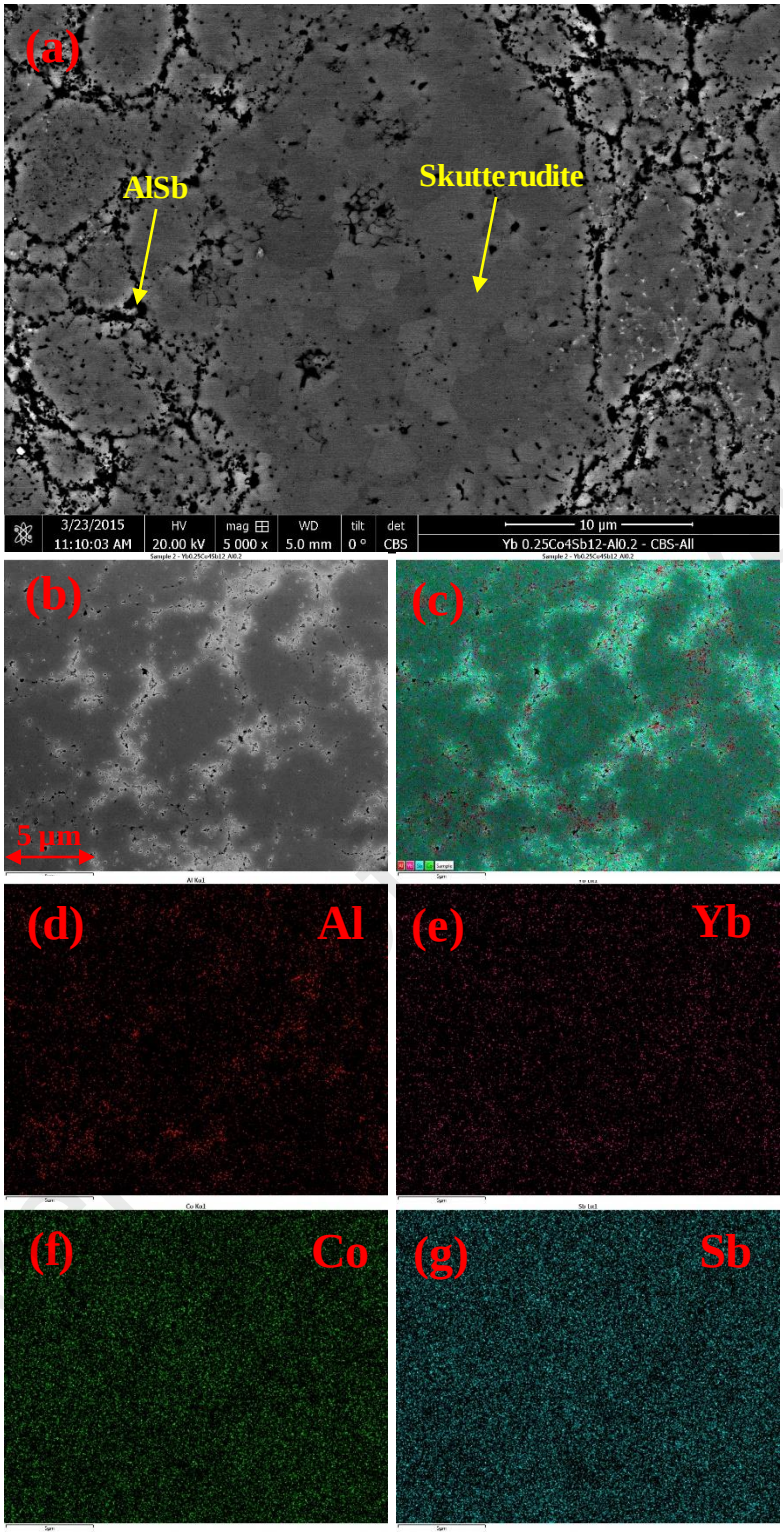

Figure 4.22: SEM images of $Al_{0.2}Yb_{0.25}Co_4Sb_{12}$; (a) a micrograph of an SPS-compacted sample, (b) an SEM/EDX micrograph, and (c) integrated elemental mapping; the elemental mapping of (d), (e), (f) and (g) show Al, Yb, Co, and Sb, respectively, extracted from (b) using EDX.

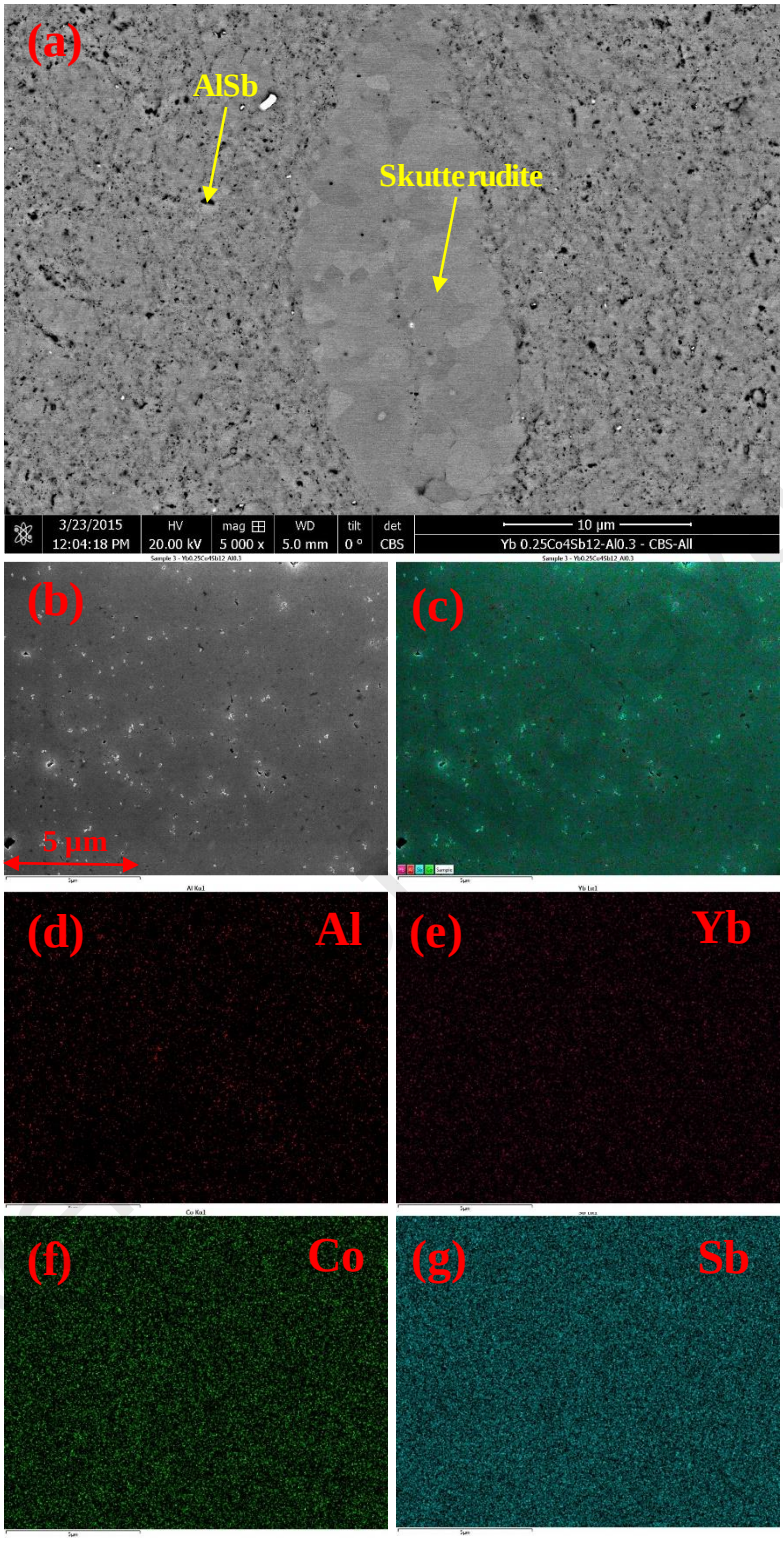

Figure 4.23: SEM images of $Al_{0.3}Yb_{0.25}Co_4Sb_{12}$; (a) a micrograph of an SPS-compacted sample, (b) an SEM/EDX micrograph, and (c) integrated elemental mapping; the elemental mapping of (d), (e), (f) and (g) show Al, Yb, Co, and Sb, respectively, extracted from (b) using EDX.

4.4.2 Thermoelectric properties

The temperature dependence of electrical resistivity for the $Al_xYb_{0.25}Co_4Sb_{12}$ (x = 0.1, 0.2 and 0.3) samples shown in Figure 4.24(a) demonstrate a very low electrical resistivity for all compositions compared with single-phase $Yb_{0.2}Co_4Sb_{12}$ (11.4 μΩm) (Li et al., 2009) at room temperature. The electrical resistivity of the compositions increased with increasing temperature, indicating a metal-like behavior over the entire temperature range for all samples. This behavior is typically similar to the $In_xYb_{0.2}Co_4Sb_{12}$ compositions discussed in the work of Peng et al. (2009). The electrical resistivity range was very narrow for all samples, i.e., minimum electrical resistivities of 5.5 μΩm, 5.3 μΩm and 7.6 μΩm at room temperature and maximum electrical resistivities of 10.9 μΩm, 9.3 μΩm and 10.5 μΩm at 577 °C were recorded for $Al_xYb_{0.25}Co_4Sb_{12}$ (x = 0.1, 0.2 and 0.3), respectively. The average value of electrical resistivity decreased with an increasing amount of AlSb nano-inclusions in the composition. Referring back to section 4.4.1, the maximum AlSb content was found in the $Al_{0.2}Yb_{0.25}Co_4Sb_{12}$ composition, which exhibited the minimum electrical resistivity among all compositions. This correlation disagrees with the result for $Yb_xCo_4Sb_{12}$/yGaSb in the work of Xiong et al. (2010) and $Yb_{0.2}Co_4Sb_{12}$/xPbTe in the work of Liu et al. (2011). in which the nano-inclusions increased the electrical resistivity. However, the high impurities and defects of the Al and AlSb nano-inclusions present in the crystal lattice of $Al_{0.3}Yb_{0.25}Co_4Sb_{12}$ may cause new additional electronic states within the bandgap and trap the charge carriers. Therefore, a suitable and controlled amount of AlSb nano-inclusions in the lattice of filled $CoSb_3$ skutterudite may significantly enhance the electrical conductivity.

Figure 4.24(b) shows the temperature dependence of the Seebeck coefficient for $Al_xYb_{0.25}Co_4Sb_{12}$ (x = 0.1, 0.2 and 0.3). A high Seebeck coefficient of -217 μV/K for the $Al_{0.1}Yb_{0.25}Co_4Sb_{12}$ sample was recorded at 577 °C. This value was reduced at the same temperature to -207 μV/K for the $Al_{0.2}Yb_{0.25}Co_4Sb_{12}$ sample. A small increase in the

Seebeck coefficient value of -212 µV/K was realized with the increase in the addition of Al in the $Al_{0.3}Yb_{0.25}Co_4Sb_{12}$ sample. The negative sign of the Seebeck coefficient values for all samples indicates n-type behavior. The Seebeck coefficient is strongly associated with the mean carrier energy near the Fermi level (Liu et al., 2011). Therefore, although the electrical resistivity is low, a high Seebeck coefficient is speculated for all compositions, attributed to the scattering of low-energy electrons by the grain-boundary potential barrier, which appears to be the dominant scattering mechanism. Martin et al. (2009) proposed that the carrier trapping in the grain boundaries forms energy barriers that impede the conduction of carriers between grains, essentially filtering charge carriers with energy less than the barrier height.

A very high and stable operating range of power factors was obtained for $Al_xYb_{0.25}Co_4Sb_{12}$ (x = 0.1, 0.2 and 0.3), as shown in Figure 4.24(c). The highest power factor of 4.9×10^{-3} W/m.K^2 belonged to the $Al_{0.1}Yb_{0.25}Co_4Sb_{12}$ sample at 377 °C. A small reduction of this value was realized at a lower temperature of 327 °C to be 4.7×10^{-3} W/m.K^2 for the $Al_{0.2}Yb_{0.25}Co_4Sb_{12}$ sample. With the increase in the Al added to the $Al_{0.3}Yb_{0.25}Co_4Sb_{12}$ sample, the maximum power factor value decreased to 4.3×10^{-3} W/m.K^2 at an elevated temperature of 577 °C.

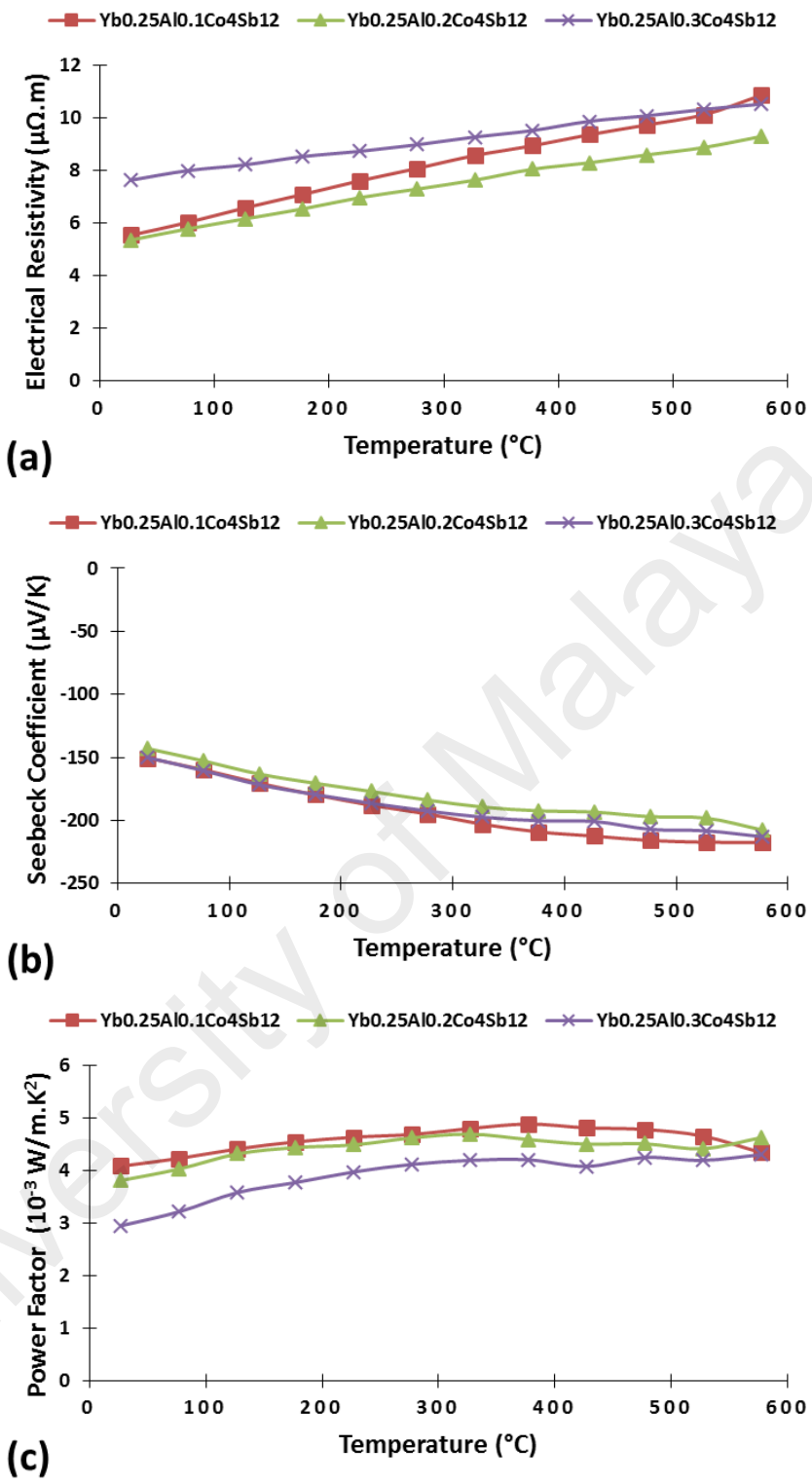

Figure 4.24: Temperature dependence of the (a) electrical resistivity, (b) Seebeck coefficient, and (c) power factor (*PF*) for Al_x-added $Yb_{0.25}Co_4Sb_{12}$ (x = 0.1, 0.2, 0.3) compositions.

In Figure 4.25(a) the temperature dependence of the thermal conductivity (K) is shown for $Al_xYb_{0.25}Co_4Sb_{12}$ (x = 0.1, 0.2 and 0.3). The minimum thermal conductivity (K_{min}) for all samples was recorded at the room temperature. The K_{min} for the $Al_{0.1}Yb_{0.25}Co_4Sb_{12}$ sample was found to be 3.3 W/m.K, and this value decreased to 3.0 W/m.K for the $Al_{0.2}Yb_{0.25}Co_4Sb_{12}$ sample. A significant reduction in K of 1.9 W/m.K was obtained for $Al_{0.3}Yb_{0.25}Co_4Sb_{12}$, the high Al content sample. The gradual increase in the thermal conductivities as a function of temperature for the $Al_{0.1}Yb_{0.25}Co_4Sb_{12}$ and $Al_{0.3}Yb_{0.25}Co_4Sb_{12}$ samples revealed a maximum K of 4.1 W/m.K and 2.7 W/m.k at 850 K, respectively. The increase in the thermal conductivity of the $Al_{0.2}Yb_{0.25}Co_4Sb_{12}$ sample at low temperatures was gradual up to 500 K and became rapid after 500 K, resulting in a relatively high thermal conductivity at elevated temperatures (K_{max} = 4.5 W/m.K at 850 K). The rapid increase in the K value after 500 K can be attributed to the effect of bipolar diffusion. The bipolar diffusion effect of electron thermal conductivity is mainly caused by the difference in the energy range of the electrons determining the electron thermal conductivity from that of electrical conductivity. Conversely, the bipolar diffusion effect may be caused by the diffusion of electron-hole pairs moving toward the same direction due to the temperature gradient of the sample. In this state, the charge of electrons and holes compensate each other, and the heat current occurs without causing an electrical current, which makes the Wiedemann-Franz law invalid.

The lattice thermal conductivity, K_L, can be estimated by subtracting the electronic contribution of the Wiedemann-Franz law, $K_e = LT/\rho$, from the total thermal conductivity, where $L = 2.45 \times 10^{-8}$ V^2K^2 is the Lorenz number (Park & Kim, 2010). As shown in Figure 4.25(b), K_L was significantly suppressed for all samples compared with the K_L of the binary skutterudite $CoSb_3$. Therefore, the minimum K_L values were found to be 1.9 W/m.K, 1.3 W/m.K and 0.6 W/m.K at 400 K, 500 K, and 500 K for $Al_xYb_{0.25}Co_4Sb_{12}$ (x = 0.1, 0.2 and 0.3), respectively. The electronic contribution K_e is more than 60% of the

total thermal conductivity in this system. It is speculated that the low K_L of the $Al_{0.3}Yb_{0.25}Co_4Sb_{12}$ sample might be due to the filling of voids in the skutterudite matrix by some Al atoms in a reciprocal manner as the Yb filler in the skutterudite matrix. The interaction between the localized modes of the two different fillers, which have sufficiently different frequencies, and the heat-carrying acoustic phonon modes might strongly scatter a broader spectrum of heat-carrying phonons.

The composites of $Al_xYb_{0.25}Co_4Sb_{12}$/AlSb demonstrated a low electrical resistivity, a high Seebeck coefficient and a low lattice thermal conductivity, and this can be attributed to the phenomenological properties of the nanometer length scales of AlSb, including enhanced interfacial phonon scattering and charge carrier filtering. Therefore, high figures of merit *ZT*s of 0.93, 0.87 and 1.36 at different operating temperatures of 800 K, 850 K and 850 K were obtained (see Figure 4.25(c)) for $Al_xYb_{0.25}Co_4Sb_{12}$ (x = 0.1, 0.2 and 0.3), respectively. Remarkably, the composites of $Al_xYb_{0.25}Co_4Sb_{12}$ with AlSb nano-inclusions yielded excellent results in terms of a fast fabrication process compared with the composition of $Yb_{0.2}Co_4Sb_{12}$ with PbTe inclusions, which showed a lower ZT value of 0.78 at 700 K when prepared by the ball-milling and hot-pressing process (Liu et al., 2011).

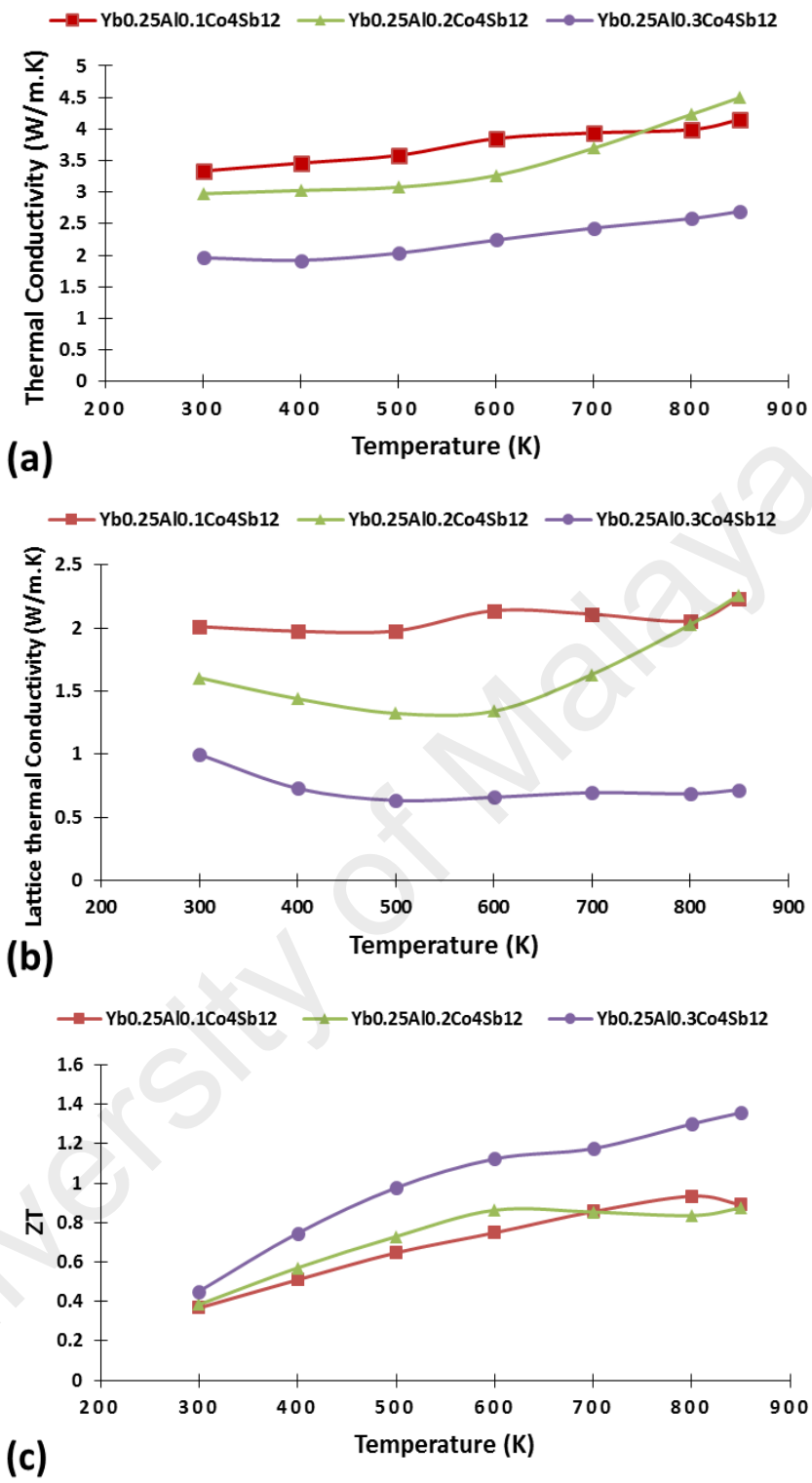

Figure 4.25: Temperature dependence of the (a) thermal conductivity, (b) lattice thermal conductivity, and (c) Figure of merit *ZT* for Al_x-added $Yb_{0.25}Co_4Sb_{12}$ (x = 0.1, 0.2, 0.3) compositions.

4.4.3 Thermal behavior

Figures 4.26 and 4.27 give the thermal stability of the Al_x-added $Yb_{0.25}Co_4Sb_{12}$ compositions (x = 0.1, 0.2, 0.3). The TGA thermographs in Figures 4.26(a), 4.26(b), and 4.26(c) show great stability of the x = 0.1, 0.2, and 0.3 compositions up to 547 °C, 530 °C, and 521 °C, respectively. A small amount of weight loss can be observed from 547 °C to 586 °C, from 530 °C to 554 °C, and from 530 °C to 554 °C for the x = 0.1, 0.2, and 0.3 compositions, respectively, attributed to the sublimation of impurities in the starting materials and/or the evaporation of the moisture gained during sample preparation for STA. Gradual weight loss above 644 °C for all compositions was realized as a result of the sublimation of Sb. Decomposition of the skutterudite phase was observed at 872 °C, 858 °C, and 852 °C for the x = 0.1, 0.2, and 0.3 compositions, respectively.

The DSC thermographs shown in Figures 4.27(a), 4.27(b) and 4.27(c) indicate two endothermic peaks for all compositions corresponding to the skutterudite phase and AlSb phase. The onset melting point was observed to be over 800 °C for all samples, which can be attributed to the skutterudite phase. A clear onset melting point of the AlSb phase was realized at 893 °C, 875 °C, and 867 °C for the x = 0.1, 0.2 and 0.3 compositions, respectively.

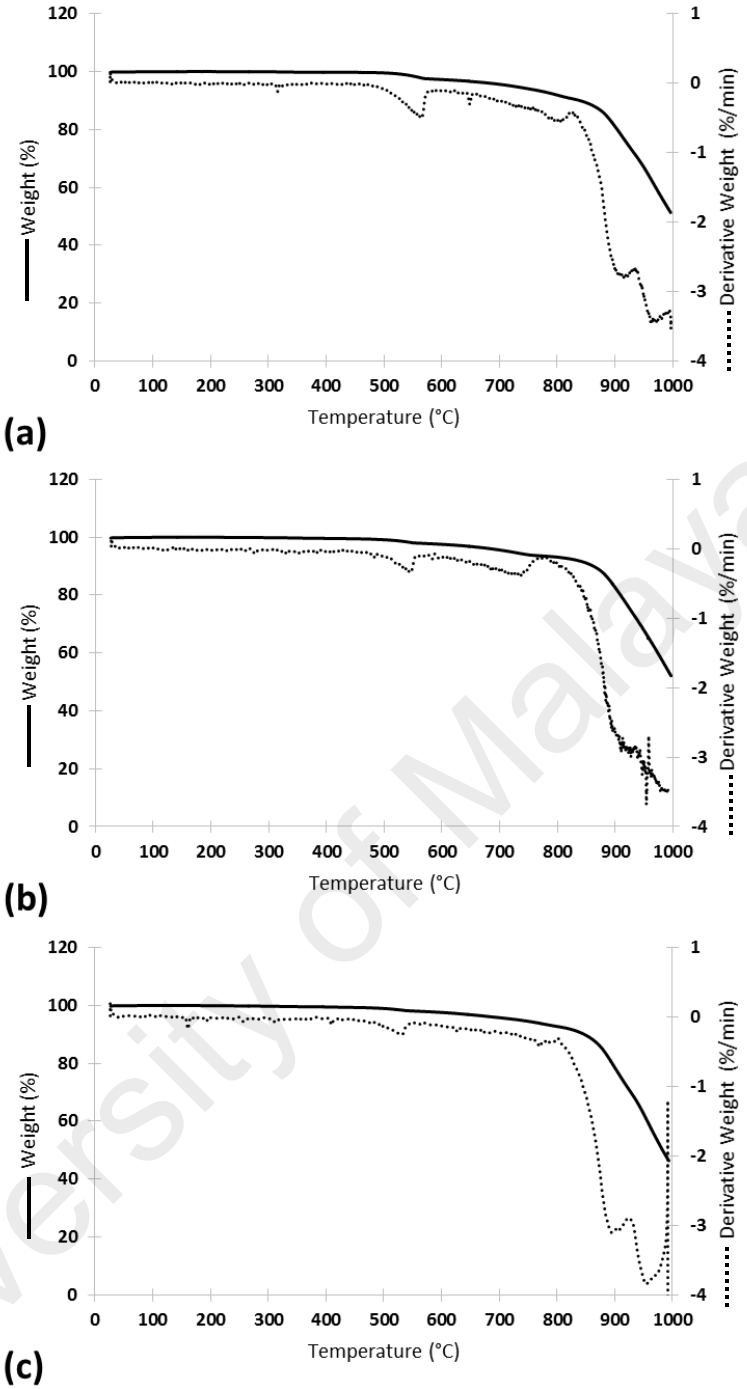

Figure 4.26: TGA thermographs upon heating of Al_x-added $Yb_{0.25}Co_4Sb_{12}$ compositions: (a) x = 0.1, (b) x = 0.2, and (c) x = 0.3.

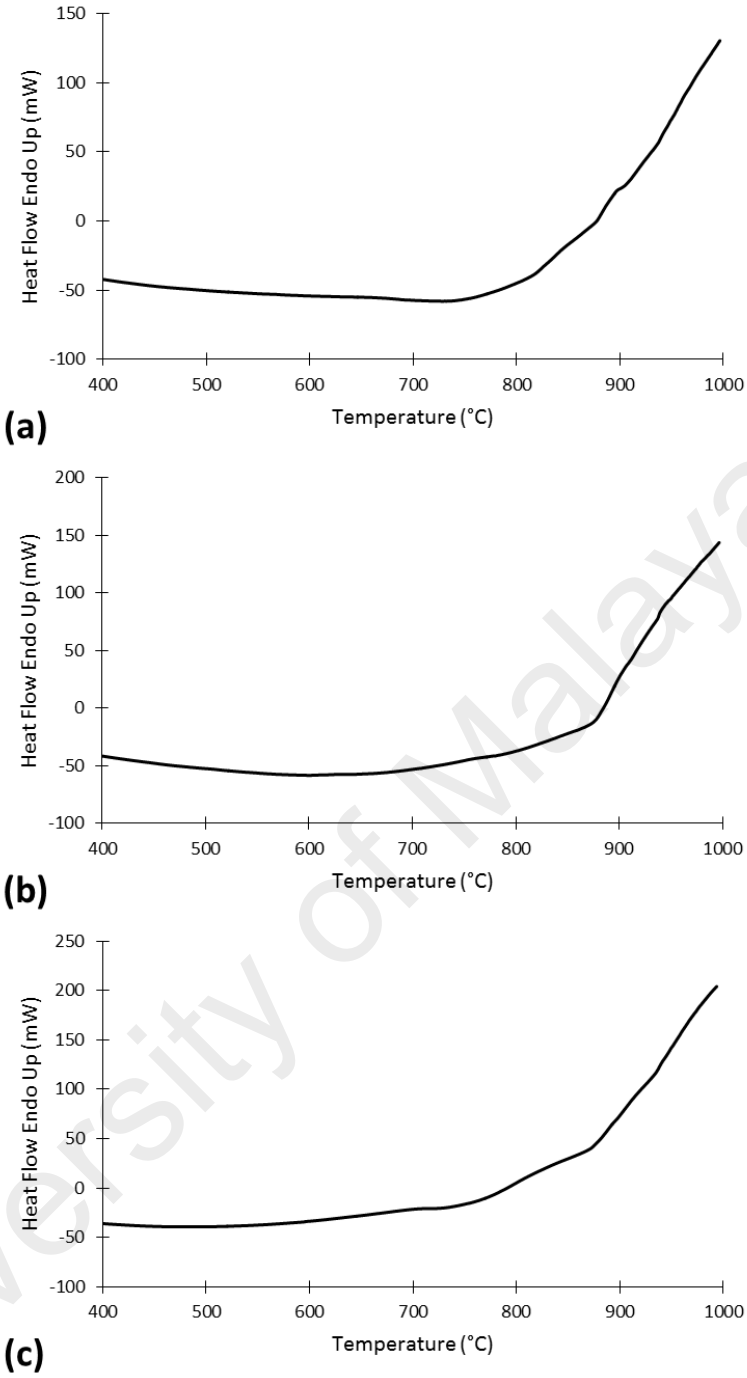

Figure 4.27: DSC thermographs upon heating (red line) and cooling (blue line) of the Al_x-added $Yb_{0.25}Co_4Sb_{12}$ compositions: (a and b) x = 0.1, (c and d) x = 0.2, and (e and f) x = 0.3.

4.4.4 Mechanical properties

To assess the homogeneity of the Al_x-added $Yb_{0.25}Co_4Sb_{12}$ samples (x = 0.1, 0.2, and 0.3), micro-hardness was mapped on several cross-sections of the specimens. A homogeneous distribution of $HV_{0.1}$ with average values of 475, 456, and 441 were observed for Al_x-added $Yb_{0.25}Co_4Sb_{12}$ compositions (x = 0.1, 0.2, and 0.3), respectively. There were no significant differences between the different regions of the samples' margins and interior areas, thus emphasizing the suitability of the SPS process for producing dense samples with a uniform microstructure. Furthermore, with the increase in the amount of added Al, the value of $HV_{0.1}$ decreased. This may be attributed to the increase in the area fraction of the grain boundaries with the increase in the added Al.

4.5 Al_xBi_y-added $Yb_{0.25}Co_4Sb_{12}$ compositions ((x, y) = (0.1,0), (0, 0.1), (0.1,0.05))

From the previous section, the excess amount of light elements from other metal groups (Al) in the grain boundaries of the $Yb_{0.25}Co_4Sb_{12}$ ternary skutterudite matrix greatly improved the thermoelectric performance by reducing the thermal conductivity and electrical resistivity, while maintaining a high Seebeck coefficient value. Therefore, doping a larger and heavier atom from other metal groups, such as Bi, into $CoSb_3$ beside heavy atoms from the lanthanide group is expected to improve the overall thermoelectric parameters. Thus, in this section, the addition of Al to the $Yb_{0.25}Co_4Sb_{12}$ ternary skutterudite matrix will be compared with the addition of Bi and Al-Bi to the same matrix.

4.5.1 Microstructural properties

Figure 4.28 shows the XRD patterns of the Al_xBi_y-added $Yb_{0.25}Co_4Sb_{12}$ compositions of ((x, y) = (0.1, 0), (0, 0.1), (0.1, 0.05)). Sharp peaks were observed for all samples, indicating their crystalline nature. For the sample with (x, y) = (0.1, 0), sharp peaks of the skutterudite phase were indicated with a small peak of the secondary AlSb phase. The

same behavior was observed for the sample with (x, y) = (0, 0.1), which had a polycrystalline of skutterudite phase with a small amount of Bi as a secondary phase. Conversely, the combination of the two dopants in one sample demonstrated a polycrystalline skutterudite phase with AlSb and Bi as secondary phases when (x, y) = (0.1, 0.05). The lattice parameters were 9.0471 Å, 9.0384 Å and 9.0374 Å for Al_xBi_y-added $Yb_{0.25}Co_4Sb_{12}$ compositions of ((x, y) = (0.1, 0), (0, 0.1), (0.1, 0.05)), respectively. The shrinkage of the lattice parameter can be attributed to the point defects caused by the Al and Bi doping. Obviously, the lattice contraction was proportional to the atomic size of the dopant and the amount of the secondary phases. For example, Bi has a relatively larger radii than Al, and, as a result, the sample that containing Bi has a smaller lattice parameter value than the one containing Al. Therefore, the availability of both dopants in one sample might increase the number of point defects and thus lead to more contraction in the lattice parameter, i.e., the (x, y) = (0.1, 0.05) sample. The fractions of AlSb and Bi in the lattice were estimated using HighScore Plus software. The software indicated that less than 0.1 *wt* % of the secondary phase's composition was formed in all samples, while the major phase was skutterudite. Thus, this may indicate that some free Al and Bi were lost in the ball-milling process and/or were squeezed out during the spark plasma sintering process.

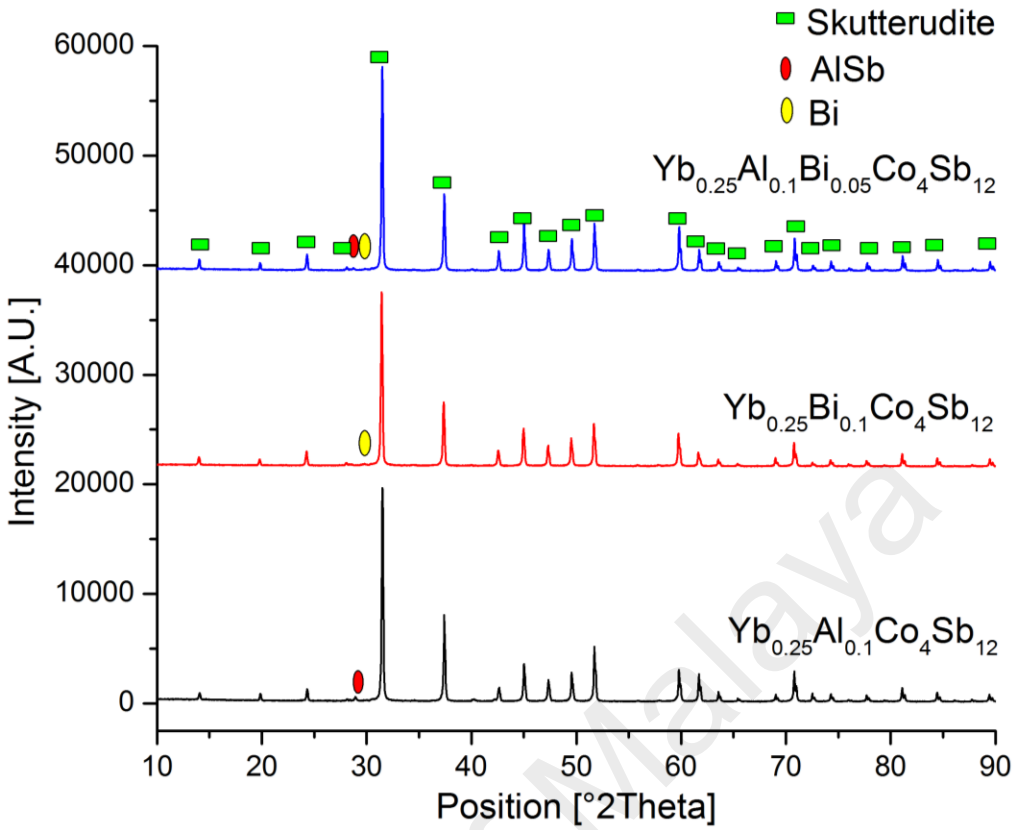

Figure 4.28: XRD patterns of the as-sintered sample of Al_xBi_y-added $Yb_{0.25}Co_4Sb_{12}$ compositions: (a) x = 0.1 and y = 0, (b) x = 0 and y = 0.1, and (c) x = 0.1 and y = 0.05.

Figures 4.21, 4.29 and 4.30 display the microstructures and compositions of the Al_xBi_y-added $Yb_{0.25}Co_4Sb_{12}$ compositions of ((x, y) = (0.1, 0), (0, 0.1), (0.1, 0.05)). Homogenous composites were observed in the backscattered electron image, as shown in Figures 4.21(a), 4.29(a) and 4.30(a). As in Figure 4.21(a) for (x, y) = (0.1, 0), an agglomeration of large grains in the form of islands was distributed over the entire sample region with small individual grains in between. In the (x, y) = (0, 0.1) sample, as shown in Figure 4.29(a), large grains were detected, and some point defects were observed inside the grains. The texture changed significantly, as shown in Figure 4.30(a), when two dopants were used in the (x, y) = (0.1, 0.05) sample. Small grains with several point defects were found to be the main feature of the Al-Bi-doped sample. However, light

atoms such as Al had less of an impact on the surface microstructure than did heavy atom such as Bi.

The elemental mapping of Al, Yb, Co and Sb shown in Figures 4.21(c, d, e, f, g) for the (x, y) = (0.1, 0) sample shows a highly uniform dispersion of Yb, Co and Sb, while an Al-rich spot was detected in the grain boundaries. A highly uniform dispersion of Yb, Co and Sb was also recorded for the (x, y) = (0, 0.1) sample inside the grains, as shown in Figures 4.29(c, d, e, f, g). Conversely, the absence of these ternary system elements was observed at some points in the grain boundaries to be occupied by Bi. In the quintuple system of (x, y) = (0.1, 0.05), the composition of which is shown in Figures 4.30(c, d, e, f, g), the elemental mapping shows a highly uniform dispersion of Yb, Co and Sb inside the grains. Conversely, Bi agglomerated along the grain boundaries and distributed evenly in the form of small spots inside the grains, while less agglomeration was detected for Al, which appeared as small Al-rich spots in the grain boundaries as well as inside the grains. In comparison, the addition of Bi to $CoSb_3$ in the work of Mallik et al. (2013) demonstrated that the Bi atom was found neither as a filler of the voids in the 2a sites nor as a substitute for Sb sites in the 24g sites of the skutterudite matrix; it was only found as a secondary phase.

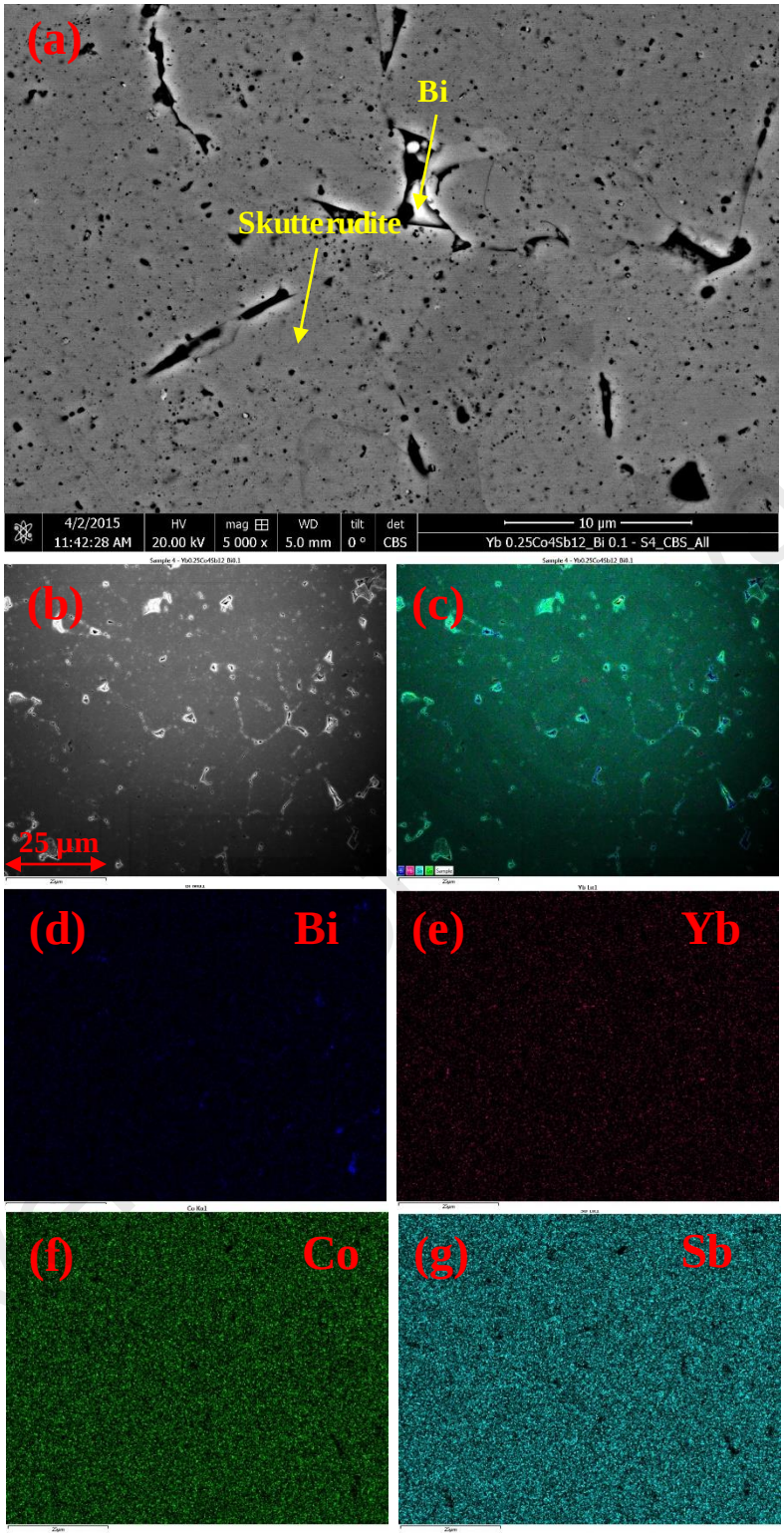

Figure 4.29: SEM images of $Bi_{0.1}Yb_{0.25}Co_4Sb_{12}$, (a) a micrograph of SPS-compacted sample, (b) an SEM/EDX micrograph, and (c) integrated elemental mapping; the elemental mapping of (d), (e), (f) and (g) show Bi, Yb, Co, and Sb, respectively, extracted from (b) using EDX.

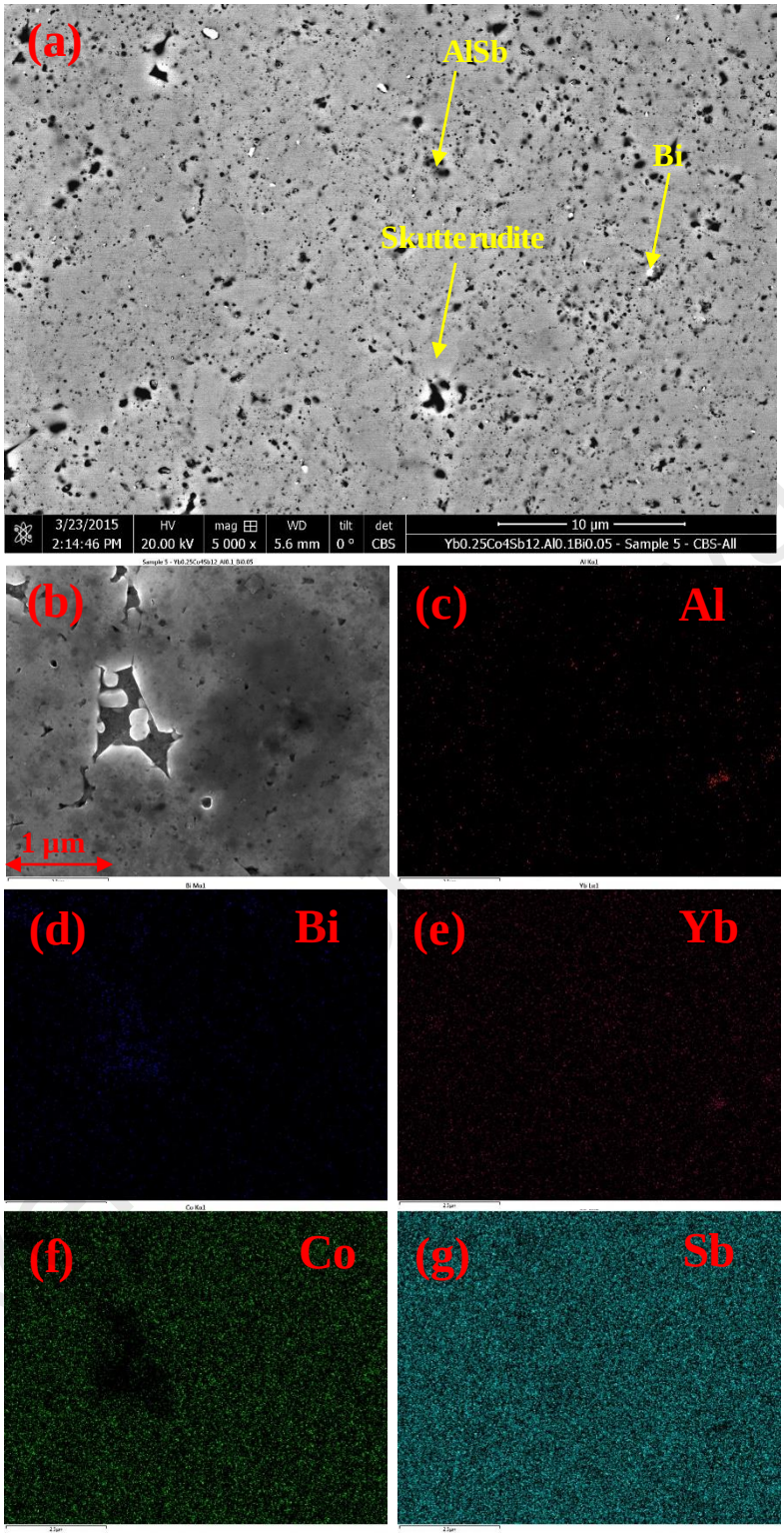

Figure 4.30: SEM images of $Al_{0.1}Bi_{0.05}Yb_{0.25}Co_4Sb_{12}$, (a) a micrograph of an SPS-compacted sample, (b) SEM/EDX micrograph; the elemental mapping of (c), (d), (e), (f) and (g) show Al, Bi, Yb, Co, and Sb, respectively, extracted from (b) using EDX.

4.5.2 Thermoelectric properties

The temperature dependence of the electrical resistivity of the Al_xBi_y-added $Yb_{0.25}Co_4Sb_{12}$ compositions of ((x, y) = (0.1, 0), (0, 0.1), (0.1, 0.05)) are shown in Figure 4.31(a). Generally, the addition of Al resulted in a very low electrical resistivity at room temperature compared with the addition of Bi. Moreover, the electrical resistivity of the composition with Al doping increased with increasing temperature, indicating a metallic behavior over the entire temperature range. The electrical resistivity of the composition with Bi doping decreased with increasing temperature, indicating a semiconductor behavior over the entire temperature range.

In addition, the range of the electrical resistivity was very narrow for the Al-doped sample, i.e., a minimum electrical resistivity of 5.5 μΩm at room temperature and a maximum electrical resistivity of 10.9 μΩm at 577 °C was recorded for $Al_{0.1}Yb_{0.25}Co_4Sb_{12}$. The range of the electrical resistivity was relatively wide for the Bi-doped sample, i.e., a minimum electrical resistivity of 30 μΩm at 427 °C and a maximum electrical resistivity of 122 μΩm at room temperature was recorded for $Bi_{0.1}Yb_{0.25}Co_4Sb_{12}$. However, a narrow range of electrical resistivity for the $Al_{0.1}Bi_{0.05}Yb_{0.25}Co_4Sb_{12}$ composition was demonstrated, i.e., a minimum electrical resistivity of 22 μΩm at room temperature and a maximum electrical resistivity of 35 μΩm at 377 °C. This sample exhibited semiconductor behavior from room temperature until 377 °C, at which point the behavior changed to a metal-like behavior. The presence of an electrically active impurity such as Bi would offset the carrier balance; thus, the formation of impurity levels might cause the structure to turn into a degenerate semiconductor with a metal-like electrical resistivity with a rise in temperature.

Figure 4.31(b) shows the temperature dependence of the Seebeck coefficient for Al_xBi_y-added $Yb_{0.25}Co_4Sb_{12}$ compositions of ((x, y) = (0.1, 0), (0, 0.1), (0.1, 0.05)). A

high Seebeck coefficient of -217 µV/K was demonstrated for the $Al_{0.1}Y_{0.25}Co_4Sb_{12}$ sample at 577 °C. The negative sign that appeared in the Seebeck coefficient values indicates n-type behavior. The Bi-doping in the $Bi_{0.1}Yb_{0.25}Co_4Sb_{12}$ composition demonstrated a higher Seebeck coefficient value of 307 µV/K at 77 °C, with a positive sign for all values over the entire temperature range, indicating p-type behavior. Thus, addition of Al increased the electron concentration, while the addition of Bi increased the concentration of holes. The Seebeck coefficient value was boosted to 409 µV/K at 277 °C for the $Al_{0.1}Bi_{0.05}Yb_{0.25}Co_4Sb_{12}$ composition. A negative sign accompanied all values over the entire temperature range, reflecting n-type behavior. A Seebeck coefficient value of -248 µV/K at 127 °C was demonstrated for $Bi_{0.05}Co_4Sb_{12}$ in Mallik et al. (2013). Therefore, the addition of Al and Bi together in the ternary skutterudite system would significantly boost the Seebeck value rather compared to using only one of these elements. Martin et al. (2009) suggested that the availability of the secondary phases may result in an increased trapping of carriers at grain boundaries, which would form energy barriers that shackle the conduction of carriers between grains. A potential barrier in the grain boundary might lead to a high Seebeck coefficient.

In Figure 4.31(c), the power factors for Al_xBi_y-added $Yb_{0.25}Co_4Sb_{12}$ compositions of ((x, y) = (0.1,0), (0, 0.1), (0.1,0.05)) are highlighted. A stable power factor operating range was obtained for $Al_{0.1}Y_{0.25}Co_4Sb_{12}$, with a maximum PF of 4.9×10^{-3} W/m.K^2 at 377 °C. A relatively low power factor of 1.3×10^{-3} W/m.K^2 at a lower temperature of 277 °C was obtained for the $Bi_{0.1}Y_{0.25}Co_4Sb_{12}$ sample. A very high power factor of 5×10^{-3} W/m.K^2 was obtained at 227 °C for $Al_{0.1}Bi_{0.05}Y_{0.25}Co_4Sb_{12}$.

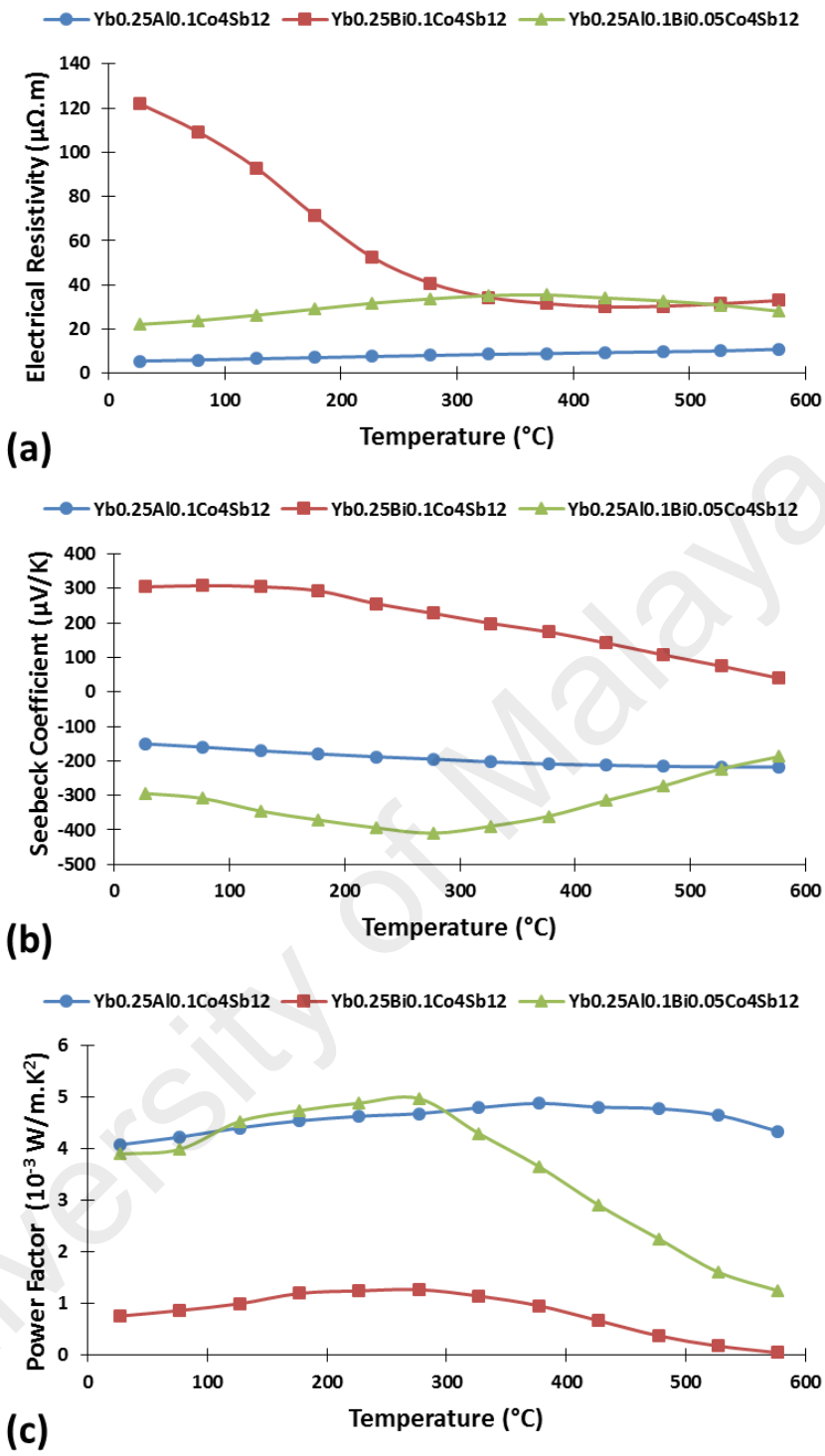

Figure 4.31: Temperature dependence of the (a) electrical resistivity, (b) Seebeck coefficient, and (c) power factor (PF) for Al_xBi_y-added $Yb_{0.25}Co_4Sb_{12}$ compositions: (a) x = 0.1 and y = 0, (b) x = 0 and y = 0.1, and (c) x = 0.1 and y = 0.05.

In Figure 4.32(a), the temperature dependence of the thermal conductivity (K) is demonstrated for Al_xBi_y-added $Yb_{0.25}Co_4Sb_{12}$ compositions of ((x, y) = (0.1, 0), (0, 0.1), (0.1, 0.05)). The minimum thermal conductivity (K_{min}) for the compositions was recorded at different temperatures. The K_{min} for the $Al_{0.1}Yb_{0.25}Co_4Sb_{12}$ sample was found to be 3.3 W/m.K at room temperature, while this value significantly decreased for the $Bi_{0.1}Yb_{0.25}Co_4Sb_{12}$ sample to 2.4 W/m.K at an elevated temperature of 850 K. The minimum K value of 2.8 W/m.K at 500 K was obtained for $Al_{0.1}Bi_{0.05}Yb_{0.25}Co_4Sb_{12}$. Over the entire temperature range, the sample with Al and Bi together had a K value that was almost average among the samples with a single dopant of either Al or Bi.

Starting from room temperature, the gradual increase in the thermal conductivity as a function of temperature was indicated for the $Al_{0.1}Yb_{0.25}Co_4Sb_{12}$ composition to a K_{max} of 4.1 W/m.K at 850 K. The opposite behavior of temperature-dependent thermal conductivity was detected for $Bi_{0.1}Yb_{0.25}Co_4Sb_{12}$. A K_{max} of 4.9 W/m.K was recorded at room temperature, and a linear drop in the K value with the increase in temperature was then demonstrated until an elevated temperature of 850 K. A combination of the two different behaviors was observed for the $Al_{0.1}Bi_{0.05}Y_{0.25}Co_4Sb_{12}$ composition. The sample exhibited a decrease in thermal conductivity until 500 K, at which point the reverse behavior occurred; a gradual increase in the K value was observed to a K_{max} of 3.7 W/m.K at 850 K. The same behavior of increasing thermal conductivity was observed above 650 K in the triple-filled skutterudites ($Ba_xYb_yIn_zCo_4Sb_{12}$) studied by Ballikaya et al. (2010) and was attributed to the electronic term.

The lattice thermal conductivity, K_L, can be estimated by subtracting the electronic contribution of the Wiedemann-Franz law, $K_e = LT/\rho$, from the total thermal conductivity, where $L = 2.45 \times 10^{-8}$ V^2K^2 is the Lorenz number (Park & Kim, 2010). As shown in Figure 4.32(b), K_L was significantly suppressed for all samples compared with the K_L of

the binary skutterudite $CoSb_3$. The effect of K_e was significant in the $Al_{0.1}Yb_{0.25}Co_4Sb_{12}$ sample, where a minimum K_L value of 1.9 W/m.K was observed at 400 K. However, a significant effect of K_L was observed for the $Bi_{0.1}Yb_{0.25}Co_4Sb_{12}$ composition, with a minimum K_L value of 1.7 W/m.K at an elevated temperature of 850 K. In the $Al_{0.1}Bi_{0.05}Yb_{0.25}Co_4Sb_{12}$ composition, the K_L was relatively high at 2.4 W/m.K at 600 K as a minimum lattice thermal conductivity.

As observed in Figure 4.32(c), the $Al_{0.1}Yb_{0.25}Co_4Sb_{12}$ composition demonstrated a low electrical resistivity, high Seebeck coefficient and low lattice thermal conductivity. Therefore, a high figure of merit *ZT* of 0.93 at 800 K was obtained. $Bi_{0.1}Yb_{0.25}Co_4Sb_{12}$ demonstrated a relatively high electrical resistivity, high Seebeck coefficient and moderated lattice thermal conductivity. Therefore, a relatively low Figure of merit *ZT*s of 0.4 at 850 K was obtained.$Al_{0.1}Bi_{0.05}Yb_{0.25}Co_4Sb_{12}$ demonstrated a moderate electrical resistivity, very high Seebeck coefficient and relatively high lattice thermal conductivity, Therefore, a Figure of merit *ZT* of 0.9 at 600 K was obtained.

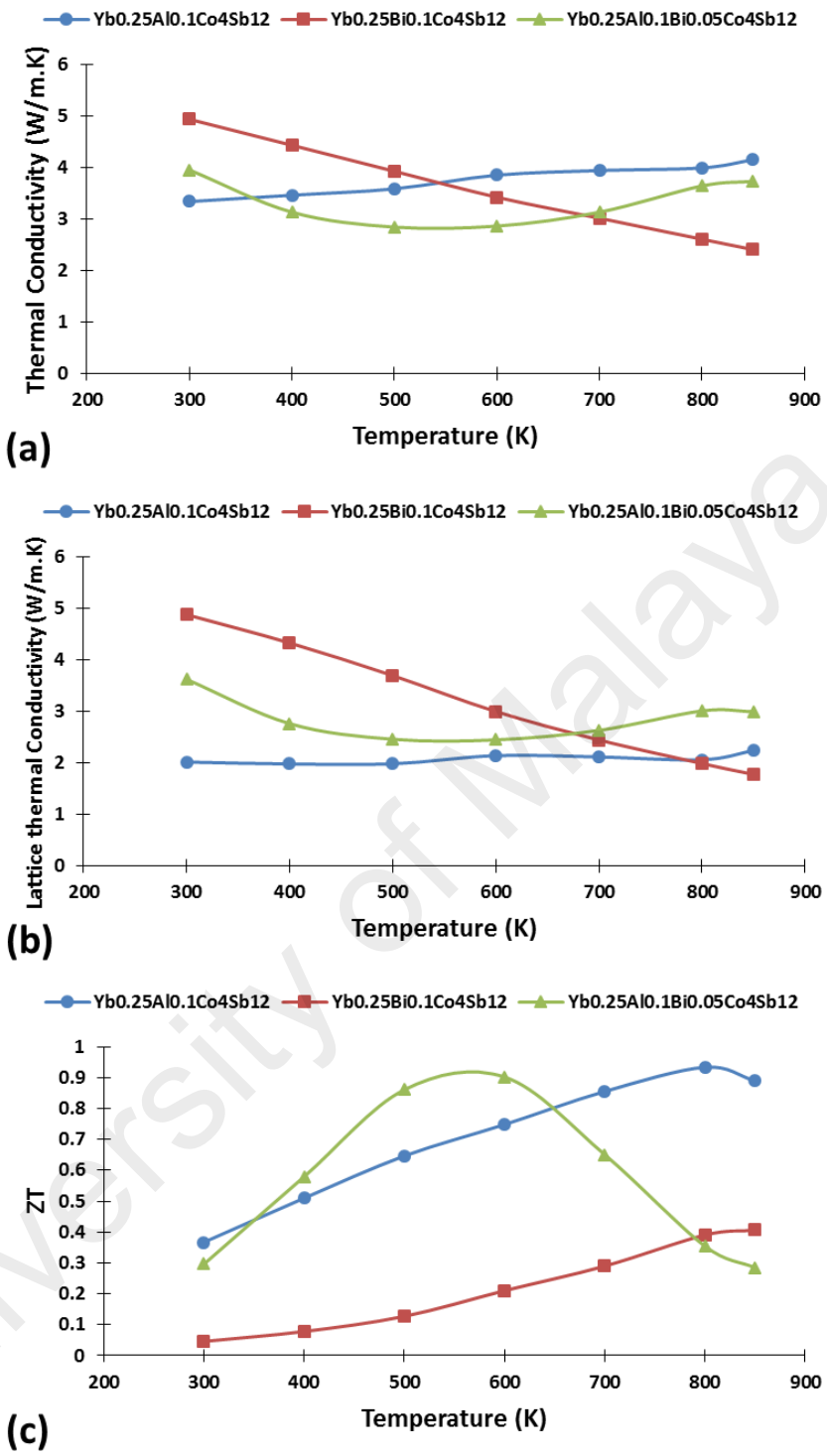

Figure 4.32: Temperature dependence of the (a) thermal conductivity, (b) lattice thermal conductivity, and (c) Figure of merit *ZT* for Al_xBi_y-added $Yb_{0.25}Co_4Sb_{12}$ compositions: (a) x = 0.1 and y = 0, (b) x = 0 and y = 0.1, and (c) x = 0.1 and y = 0.05.

4.5.3 Thermal behavior

Figures 4.33 and 4.34 indicate the thermal stability of Al_xBi_y-added $Yb_{0.25}Co_4Sb_{12}$ compositions of (x, y) = (0.1, 0), (0, 0.1), and (0.1, 0.05). The TGA thermograph in Figures 4.33(a), 4.33(b), and 4.33(c) shows great stability of the (x, y) = (0.1, 0), (0, 0.1), and (0.1, 0.05) compositions up to 547 °C, 533 °C, and 533 °C, respectively. A small amount of weight loss can be observed from 547 °C to 586 °C, from 533 °C to 561 °C, and from 533 °C to 553 °C for the (x, y) = (0.1, 0), (0, 0.1), and (0.1, 0.05) compositions, respectively, attributed to the sublimation of impurities in the starting materials and/or the evaporation of the moisture gained during sample preparation for STA. Gradual weight loss above 644 °C was realized for all compositions as a result of the sublimation of Sb. Decomposition of the skutterudite phase was observed at 872 °C, 865 °C, and 872 °C for the (x, y) = (0.1,0), (0, 0.1), and (0.1,0.05) compositions, respectively.

The DSC thermographs of Al_xBi_y-added $Yb_{0.25}Co_4Sb_{12}$ compositions of (x, y) = (0.1,0), (0, 0.1), and (0.1,0.05) are shown in Figure 4.34. Figure 4.34(a) indicates two endothermic peaks for the (x, y) = (0.1, 0) composition, corresponding to onset melting points of the skutterudite phase and AlSb phase at over 800 °C and 890 °C, respectively. From Figure 4.34(b), an onset melting point of over 800 °C was obtained for (x, y) = (0, 0.1), which can be attributed to the skutterudite phase. In addition, there were other sub-endothermic peaks for the melting of the residual phases after decomposition. From Figure 4.34(c), an onset melting point at over 800 °C was obtained for (x, y) = (0.1, 0.05), which can be attributed to the skutterudite phase. In addition, there were other sub-endothermic peaks for the melting of the residual phases after decomposition.

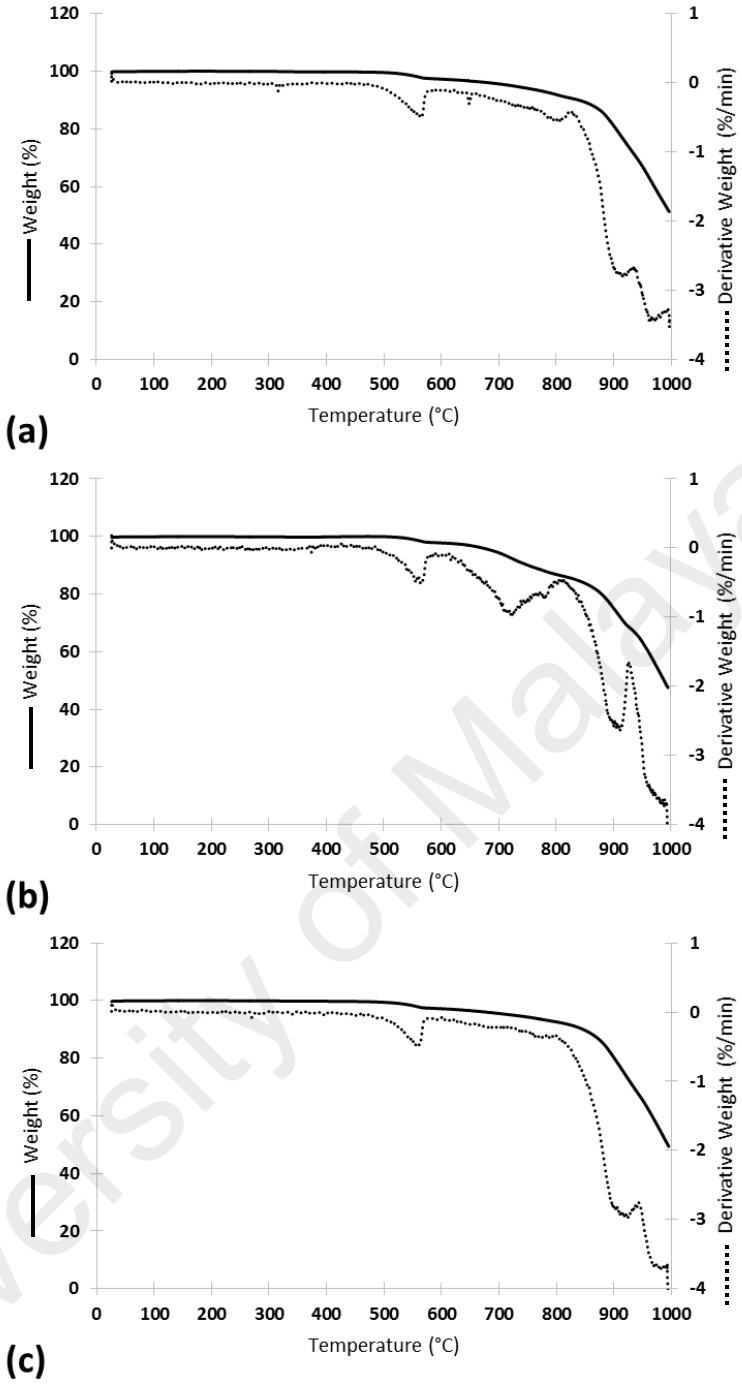

Figure 4.33: TGA thermographs upon heating (red line) and cooling (blue line) of the Al_xBi_y-added $Yb_{0.25}Co_4Sb_{12}$ compositions: (a) x = 0.1 and y = 0, (b) x = 0 and y = 0.1, and (c) x = 0.1 and y = 0.05.

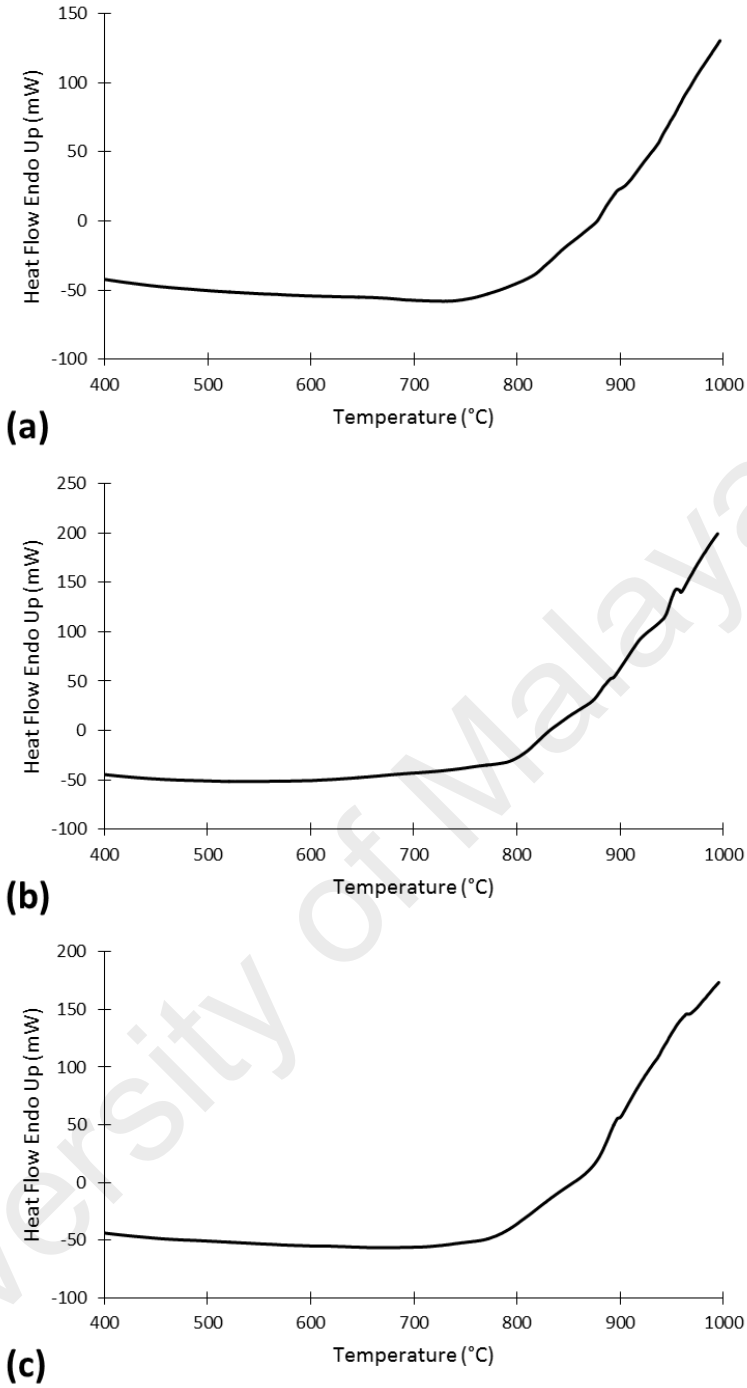

Figure 4.34: DSC thermographs upon heating (red line) and cooling (blue line) of the Al_xBi_y-added $Yb_{0.25}Co_4Sb_{12}$ compositions: (a and b) x = 0.1 and y = 0, (c and d) x = 0 and y = 0.1, and (e and f) x = 0.1

4.5.4 Mechanical properties

To assess the homogeneity of the Al_xBi_y-added $Yb_{0.25}Co_4Sb_{12}$ samples (x, y) = (0.1, 0), (0, 0.1), (0.1, 0.05), micro-hardness was mapped on several cross-sections of the specimens. A homogeneous distribution of $HV_{0.1}$ with average values of 475, 430, and 442 was observed for the Al_xBi_y-added $Yb_{0.25}Co_4Sb_{12}$ compositions of (x, y) = (0.1, 0), (0, 0.1), (0.1, 0.05), respectively. There were no significant differences between the different regions of the samples' margins and interior areas, thus emphasizing the suitability of the SPS process for producing dense samples with a uniform microstructure. Furthermore, the addition of Bi had a greater impact on the microstructure of the ternary skutterudite system than did the addition of Al. The sample with added Bi had a lower $HV_{0.1}$ value than the sample with added Al. This may be attributed to the higher number of point defects in the Bi-added sample than in the Al-added sample.

CHAPTER 5: CONCLUSIONS AND RECOMMENDATIONS

5.1 Conclusions

Thermoelectric materials for waste-heat recovery, refrigeration and other applications are of great interest because they can serve as a secondary heat generation technology, which leads to a reduction in the global dependency on fossil fuels. Therefore, in this work, novel skutterudite thermoelectric materials which can be used for waste-heat recovery in the aerospace and automobile applications were synthesized and examined in terms of their microstructural, thermoelectric, charge transport, and mechanical properties, as well as the thermal stability of the final products. The following formulations were explored with conclusions that indicate a strategy to increase the thermoelectric figure of merit:

1. A formulation of Mn-added $CoSb_3$ was studied. The fabrication process involved mechanical alloying followed by spark plasma sintering to produce a fully dense sample. Polycrystalline phases of skutterudite with Mn-rich spots in the grain boundaries were obtained. By using small transition metal atoms such as Mn, we were optimistic in significantly decreasing the electrical resistivity as well as the thermal conductivity. However, a tiny reduction in the electrical resistivity from the binary skutterudite $CoSb_3$ was obtained. However, a moderate decrease in the lattice thermal conductivity was observed. Through this work, useful strategies in the modification of binary skutterudites using light elements were initiated.
2. A fully dense sample of Hf-added CoSb3 was synthesized using the mechanical alloying technique followed by spark plasma sintering. Polycrystalline phases of skutterudite were obtained in addition to Hf-rich regions in the grain boundaries. By using relatively small and heavy transition metal cations such as Hf, a similar effect to that of the lanthanide elements was expected. However, a tiny reduction in the electrical resistivity, from the binary skutterudite $CoSb_3$ was obtained.

However, a significant decrease (up to 60%) in the lattice thermal conductivity was observed.

3. Excess doping of Al into $CoSb_3$ was investigated to examine the effect of excess doping on the skutterudite morphology and ultimately the thermoelectric performance. Fully dense samples of a modified skutterudite compound, by addition of Alx (0.3, 0.6, 2), were obtained using mechanical alloying followed by spark plasma sintering. The XRD result showed that the addition of Alx (0.3, 0.6, 2) resulted in the formation of a skutterudite phase with AlSb as a secondary phase. However, EDX indicated islands of a skutterudite phase surrounded by Al-rich spots located in the grain boundaries. Moreover, the addition of Al had a significant effect on the lattice thermal conductivity of $CoSb_3$, which was reduced by ~45% in the case of x = 2. It is believed that grain boundary phonon scattering plays a key role in reducing the thermal conductivity. However, a low figure of merit *ZT* was obtained as a consequence of a high electrical resistivity. Thus, this work is useful in deriving a pathway for improvement in thermoelectrics through microstructural modification.

   More interestingly, for the formulation of $Al_{0.3}Co_4Sb_{12}$, a spin crossover behavior was observed; this is suggested to occur through the transition from low-spin Co(III) to high-spin Co (III), which results in a reversible conversion from n-type to p-type at temperature of 200 °C. Although the current *ZT* (= 0.06) is low for this formulation, it might be an interesting pathway to manipulate the p- and n-type properties of a particular skutterudite formulation.

4. Al was doped into the $Yb_{0.25}Co_4Sb_{12}$ skutterudite system. This formulation was the most successful in achieving the highest *ZT* (= 1.36) in this work for $Al_{0.3}Yb_{0.25}Co_4Sb_{12}$. Fully dense samples of $Al_xYb_{0.25}Co_4Sb_{12}$ (x = 0.1, 0.2 and 0.3)

were obtained using the mechanical alloying technique followed by spark plasma sintering. A polycrystalline skutterudite phase was obtained in addition to a small amount of an AlSb secondary phase located in the grain boundaries. The increase in Al doping was correlated to a reduction in thermal conductivity, reaching a maximum reduction of 58% from pure $CoSb_3$ with $Al_{0.3}$ addition. Furthermore, the electrical conductivity was maximal with the $Al_{0.2}Yb_{0.25}Co_4Sb_{12}$ formulation due to the presence of AlSb nano-inclusions. Overall, the key driver of the performance in achieving the maximum *ZT* for $Al_{0.3}Yb_{0.25}Co_4Sb_{12}$ was through the significant reduction in thermal conductivity and a relatively high magnitude of electrical conductivity.

5. Al and Bi were added to the $Yb_{0.25}Co_4Sb_{12}$ skutterudite system. Fully dense samples of Al_xBi_y-added $Yb_{0.25}Co_4Sb_{12}$ compositions ((x, y) = (0.1,0), (0, 0.1), (0.1,0.05)) were obtained by mechanical alloying followed by spark plasma sintering. A polycrystalline skutterudite phase was obtained in addition to a small amount of AlSb and Bi as secondary phases located in the grain boundaries. The effect of Bi addition on the lattice thermal conductivity was much more significant that the effect Al addition. This significant effect was reflected negatively in the power factor, as the sample with added Bi demonstrated a relatively low PF, whereas a significant PF was realized for the Al-added sample. Therefore, the combination of free Bi atoms to serve as phonon scatterers with AlSb to serve as carrier traps in the grain boundaries resulted in a very high power factor (5 μV/K) and a relatively low lattice thermal conductivity (3.2) for the composition of $Al_{0.1}Bi_{0.05}$-added $Yb_{0.25}Co_4Sb_{12}$, yielding a *ZT* of 0.9.

The overall thermoelectric performance of the individual formulations is presented in table 5.1. We hope that with the different strategies of doping, either through substitution or filling, and grain boundary modification, a way forward in optimizing the figures of merit for $CoSb_3$ skutterudite systems can be realized based on this work.

Table 5.1: Summary of the results

No.	Composition	ρ_{min} (μΩ.m)	α_{max} (μV/K)	PF (10^{-3} W/m.K^2)	κ_{min} (W/m.K)	κ_{Lmin} (W/m.K)	ZT	HV
1	Mn-added $CoSb_3$	33.2 @ 577 °C	242 @ 127 °C	0.39 @ 277 °C	3.3 @ 500 K	3.3 @ 500 K	0.06 @ 600 K	639
2	Hf-added $CoSb_3$	52.1 @ 546 °C	153 @ 153 °C	0.14 @ 300 °C	1.8 @ 400 K	1.8 @ 400 K	0.04 @ 500 K	331
3	$Al_{0.3}$-added $CoSb_3$	31.5 @ 527 °C	-251 @ 27 °C	0.4 @377 °C	4.6 @ 600 K	4.4 @ 600 K	0.05 @ 600 K	499
4	$Al_{0.6}$-added $CoSb_3$	38.4 @ 527 °C	218 @ 127 °C	0.4 @ 327 °C	3.3 @ 500 K	3.2 @ 500 K	0.07 @ 600 K	469
5	Al_2-added $CoSb_3$	56.5 @ 527 °C	218 @ 127 °C	0.34 @ 277 °C	2.7 @ 500 K	2.6 @ 500 K	0.06 @ 600 K	436
6	$Al_{0.1}$-added $Yb_{0.25}Co_4Sb_{12}$	5.5 @ 27 °C	-217 @ 577 °C	4.9 @ 377 °C	3.3 @ 300 K	2 @ 400 K	0.93 @ 800 K	475
7	$Al_{0.2}$-added $Yb_{0.25}Co_4Sb_{12}$	5.4 @ 27 °C	-208 @ 577 °C	4.7 @ 327 °C	3 @ 300 K	1.3 @ 500 K	0.87 @ 850 K	456
8	$Al_{0.3}$-added $Yb_{0.25}Co_4Sb_{12}$	7.6 @ 27 °C	-213 @ 577 °C	4.3 @ 577 °C	1.9 @ 300 K	0.6 @ 500 K	1.36 @ 850 K	441
9	$Bi_{0.1}$-added $Yb_{0.25}Co_4Sb_{12}$	30 @ 427 °C	307 @ 77 °C	1.3 @ 277 °C	2.4 @ 850 K	1.8 @ 850 K	0.4 @ 850 K	430
10	$Al_{0.1}Bi_{0.05}$-added $Yb_{0.25}Co_4Sb_{12}$	22 @ 27 °C	-409 @ 277 °C	5 @ 277 °C	2.8 @ 500 K	2.4 @ 600 K	0.9 @ 600 K	442

5.2 Recommendations

Optimization of the conditions of the mechanical alloying technique and spark plasma sintering process could lead to improved figures of merit, the amount of dopants that serve as phonon scatterers or that serve as carrier traps in the grain boundaries could be optimized, Hafnium can be doped into binary skutterudite with other elements that are compatible with the skutterudite matrix to insure improvement of the overall parameters, Aluminum addition can be introduced into other ternary skutterudite systems, elements such as silver, gold and copper can be used as energy barriers to improve the efficiency of skutterudite thermoelectric materials, and the final products of this project can be incorporated and integrated into thermoelectric modules for the realization of thermoelectric devices for waste thermal energy harvesting.

REFERENCES

Abdul-Wahab, S. A., Elkamel, A., Al-Damkhi, A. M., Al-Habsi, I. A., Al-Rubai'ey', H. S., Al-Battashi, A. K., Al-Tamimi, A. R., Al-Mamari, K. H. and Chutani, M. U. (2009). Design and experimental investigation of portable solar thermoelectric refrigerator. *Renewable Energy, 34*(1): 30-34.

Adachi, H., Uchida, K., Saitoh, E. and Maekawa, S. (2013). Theory of the spin Seebeck effect. *Reports on progress in physics. Physical Society, 76*(3): 036501.

Afshar, O., Saidur, R., Hasanuzzaman, M. and Jameel, M. (2012). A review of thermodynamics and heat transfer in solar refrigeration system. *Renewable & Sustainable Energy Reviews, 16*(8): 5639-5648.

Ahamat, M. A. and Tierney, M. J. (2011). Timewise temperature control with heat metering using a thermoelectric module. *Applied Thermal Engineering, 31*(8-9): 1421-1426.

Ahiska, R., Dislitas, S. and Omer, G. (2012). A new method and computer-controlled system for measuring the time constant of real thermoelectric modules. *Energy Conversion and Management, 53*(1): 314-321.

Al-Merbati, A. S., Yilbas, B. S. and Sahin, A. Z. (2013). Thermodynamics and thermal stress analysis of thermoelectric power generator: Influence of pin geometry on device performance. *Applied Thermal Engineering, 50*(1): 683-692.

Alam, H. and Ramakrishna, S. (2013). A review on the enhancement of figure of merit from bulk to nano-thermoelectric materials. *Nano Energy, 2*(2): 190-212.

Alboni, P. N., Ji, X., He, J., Gothard, N., Hubbard, J. and Tritt, T. M. (2007). Synthesis and thermoelectric properties of "nano-engineered" $CoSb_3$ skutterudite materials. *Journal of Electronic Materials, 36*(7): 711-715.

Alleno, E., Berardan, D., Godart, C., Puyet, M., Lenoir, B., Lackner, R., Bauer, E., Girard, L. and Ravot, D. (2006). Double filling in skutterudites: A promising path to improved thermoelectric properties. *Physica B-Condensed Matter, 383*(1): 103-106.

Anno, H., Yamada, H., Nakabayashi, T., Hokazono, M. and Shirataki, R. (2012). Gallium composition dependence of crystallographic and thermoelectric properties in polycrystalline type-I $Ba_8Ga_xSi_{46-x}$ (nominal x=14–18) clathrates prepared by combining arc melting and spark plasma sintering methods. *Journal of Solid State Chemistry, 193*: 94-104.

Asenath-Smith, E., Misture, S. T. and Edwards, D. D. (2011). Structural behavior and thermoelectric properties of the brownmillerite system $Ca_2(Zn_xFe_{2-x})O_5$. *Journal of Solid State Chemistry, 184*(8): 2167-2177.

Bae, N. H., Han, S., Lee, K. E., Kim, B. and Kim, S. T. (2011). Diffusion at interfaces of micro thermoelectric devices. *Current Applied Physics, 11*(5): S40-S44.

Bai, S. Q., Pei, Y. Z., Chen, L. D., Zhang, W. Q., Zhao, X. Y. and Yang, J. (2009). Enhanced thermoelectric performance of dual-element-filled skutterudites BaxCeyCo4Sb12. *Acta Materialia, 57*(11): 3135-3139.

Ballikaya, S., Uzar, N., Yildirim, S., Salvador, J. R. and Uher, C. (2012). High thermoelectric performance of In, Yb, Ce multiple filled $CoSb_3$ based skutterudite compounds. *Journal of Solid State Chemistry, 193*: 31-35.

Ballikaya, S., Wang, G., Sun, K. and Uher, C. (2010). Thermoelectric Properties of Triple-Filled $Ba_xYb_yIn_zCo_4Sb_{12}$ Skutterudites. *Journal of Electronic Materials, 40*(5): 570-576.

Bennett, G. L. , Hemler, R. J. and Schock, A. . (1996). Status Report on the U.S. Space Nuclear Program. *Acta Astronautica, 38*(4-9): 551-560.

Bian, Z. X. and Shakouri, A. (2006). Enhanced solid-state thermionic emission in nonplanar heterostructures. *Applied Physics Letters, 88*(1): 012102.

Bracht, H. A., Silvestri, H. H. and Haller, E. E. (2005). Advanced diffusion studies with isotopically controlled materials. *Solid State Communications, 133*(11): 727-735.

Bulusu, A. and Walker, D. G. (2008). Review of electronic transport models for thermoelectric materials. *Superlattices and Microstructures, 44*(1): 1-36.

Cadoff, Irving B. and Miller, Edward. (1960). *Thermoelecteric Materials and Devices*. New York: Reinhold Publishing Corporation.

Cai, K. F., Mueller, E., Drasar, C. and Stiewe, C. (2004). The effect of titanium diboride addition on the thermoelectric properties of β-$FeSi_2$ semiconductors. *Solid State Communications, 131*(5): 325-329.

Carreon, H. (2013). On the exploitation of thermoelectric coupling for characterization of elliptical inclusions in metals. *Experimental Thermal and Fluid Science, 44*: 673-679.

Chakoumakos, B. C. and Sales, B. C. (2006). Skutterudites: Their structural response to filling. *Journal of Alloys and Compounds, 407*(1-2): 87-93.

Chang, Y. W., Chang, C. C., Ke, M. T. and Chen, S. L. (2009). Thermoelectric air-cooling module for electronic devices. *Applied Thermal Engineering, 29*(13): 2731-2737.

Chatterjee, K., Suresh, A., Ganguly, S., Kargupta, K. and Banerjee, D. (2009). Synthesis and characterization of an electro-deposited polyaniline-bismuth telluride nanocomposite - A novel thermoelectric material. *Materials Characterization, 60*(12): 1597-1601.

Chein, R. and Huang, G. M. (2004). Thermoelectric cooler application in electronic cooling. *Applied Thermal Engineering, 24*(14-15): 2207-2217.

Chen, L. G., Li, J., Sun, F. R. and Wu, C. (2005). Performance optimization of a two-stage semiconductor thermoelectric-generator. *Applied Energy, 82*(4): 300-312.

Chen, L. G., Meng, F. K. and Sun, F. R. (2012). Effect of heat transfer on the performance of thermoelectric generator-driven thermoelectric refrigerator system. *Cryogenics, 52*(1): 58-65.

Cherkez, R. (2012). Theoretical studies on the efficiency of air conditioner based on permeable thermoelectric converter. *Applied Thermal Engineering, 38*: 7-13.

Choi, Y., Kim, Y., Park, S. G., Kim, Y. G., Sung, B. J., Jang, S. Y. and Kim, W. (2011). Effect of the carbon nanotube type on the thermoelectric properties of CNT/Nafion nanocomposites. *Organic Electronics, 12*(12): 2120-2125.

Christensen, M., Juranyi, F. and Iversen, B. B. (2006). The rattler effect in thermoelectric clathrates studied by inelastic neutron scattering. *Physica B-Condensed Matter, 385*: 505-507.

Constantinescu, G., Rasekh, S., Torres, M. A., Madre, M. A., Diez, J. C. and Sotelo, A. (2013). Enhancement of the high-temperature thermoelectric performance of $Bi_2Ba_2Co_2O_x$ ceramics. *Scripta Materialia, 68*(1): 75-78.

Cui, J. L., Zhao, X. B., Zhao, W. M. and Lu, Y. P. (2002). Preparation, thermoelectric properties and interface analysis of n-type graded material $FeSi_2/Bi_2Te_3$. *Materials Science and Engineering B-Solid State Materials for Advanced Technology, 94*(2-3): 223-228.

Dai, D., Zhou, Y. X. and Liu, J. (2011). Liquid metal based thermoelectric generation system for waste heat recovery. *Renewable Energy, 36*(12): 3530-3536.

Dai, Y. J., Wang, R. Z. and Ni, L. (2003). Experimental investigation on a thermoelectric refrigerator driven by solar cells. *Renewable Energy, 28* 949–959.

Das, V. D. and Ganesan, P. G. (1998). Thickness and temperature effects on thermoelectric power and electrical resistivity of $(Bi_{0.25}Sb_{0.75})_2Te_3$ thin films. *Materials Chemistry and Physics, 57*: 57-66.

Delaizir, G., Bernard-Granger, G., Monnier, J., Grodzki, R., Kim-Hak, O., Szkutnik, P. D., Soulier, M., Saunier, S., Goeuriot, D., Rouleau, O., Simon, J., Godart, C. and Navone, C. (2012). A comparative study of Spark Plasma Sintering (SPS), Hot Isostatic Pressing (HIP) and microwaves sintering techniques on p-type Bi_2Te_3 thermoelectric properties. *Materials Research Bulletin, 47*(8): 1954-1960.

Delorme, F., Martin, C. F., Marudhachalam, P., Ovono, D. O. and Guzman, G. (2011). Effect of Ca substitution by Sr on the thermoelectric properties of $Ca_3Co_4O_9$ ceramics. *Journal of Alloys and Compounds, 509*(5): 2311-2315.

Deng, L., Jia, X. P., Su, T. C., Jiang, Y. P., Zheng, S. Z., Guo, X. and Ma, H. A. (2011). The thermoelectric properties of $Co_4Sb_{12-x}Te_x$ synthesized at different pressure. *Materials Letters, 65*(6): 1057-1059.

Deng, Y., Zhu, W., Wang, Y. and Shi, Y. M. (2013). Enhanced performance of solar-driven photovoltaic-thermoelectric hybrid system in an integrated design. *Solar Energy, 88*: 182-191.

Dmitriev, A. V. and Zvyagin, I. P. (2010). Current trends in the physics of thermoelectric materials. *Physics-Uspekhi, 53*(8): 789-803.

Drasar, C., Kucek, V., Benes, L., Lostak, P. and Vlcek, M. b. (2012). Thermoelectric properties and nonstoichiometry of GaGeTe. *Journal of Solid State Chemistry, 193*: 42–46.

Du, Y., Shen, S. Z., Cai, K. F. and Casey, P. S. (2012). Research progress on polymer-inorganic thermoelectric nanocomposite materials. *Progress in Polymer Science, 37*(6): 820-841.

Dughaish, Z. H. (2005). Lead telluride as a thermoelectric material for thermoelectric power generation. *Physica B, 322* 205–223.

Dyck J. S., Chen W., Uher C., Chen L., Tang X. and T., Hirai. (2002). Thermoelectric properties of the n-type filled skutterudite $Ba_{0.3}Co_4Sb_{12}$ doped with Ni. *Journal of Applied Physics, 91*(6): 3698-3705.

El-Genk, M. S. and Saber, H. H. (2005). Performance analysis of cascaded thermoelectric converters for advanced radioisotope power systems. *Energy Conversion and Management, 46*(7-8): 1083-1105.

El-Genk, M. S. and Saber, H. H. (2006). Thermal and performance analyses of efficient radioisotope power systems. *Energy Conversion and Management, 47*(15-16): 2290-2307.

El-Genk, M. S., Saber, H. H. and Caillat, T. (2003). Efficient segmented thermoelectric unicouples for space power applications. *Energy Conversion and Management, 44*(11): 1755-1772.

El-Genk, M. S., Saber, H. H., Caillat, T. and Sakamoto, J. (2006). Tests results and performance comparisons of coated and un-coated skutterudite based segmented unicouples. *Energy Conversion and Management, 47*(2): 174-200.

Escriba, C., Campo, E., Esteve, D. and Fourniols, J. Y. (2005). Complete analytical modeling and analysis of micromachined thermoelectric uncooled IR sensors. *Sensors and Actuators a-Physical, 120*(1): 267-276.

Faid, F., Romdhane, M., Gourdon, C., Wilhelm, A. M. and Delmas, H. (1998). A comparative study of local sensors of power ultrasound effects: electrochemical, thermoelectrical and chemical probes. *Ultrason Sonochem, 5*(2): 63-68.

Fan, X., Case, E. D., Ren, F., Shu, Y. and Baumann, M. J. (2012). Part II: Fracture strength and elastic modulus as a function of porosity for hydroxyapatite and other brittle materials. *Journal of the Mechanical Behavior of Biomedical Materials, 8*: 99-110.

Ferreira, N. M., Rasekh, S., Costa, F. M., Madre, M. A., Sotelo, A., Diez, J. C. and Torres, M. A. (2012). New method to improve the grain alignment and performance of thermoelectric ceramics. *Materials Letters, 83*: 144-147.

Fthenakis, V. and Kim, H. C. (2010). Life-cycle uses of water in U.S. electricity generation. *Renewable and Sustainable Energy Reviews, 14*(7): 2039-2048.

Fu, C. G., Xie, H. H., Liu, Y. T., Zhu, T. J., Xie, J. and Zhao, X. B. (2013). Thermoelectric properties of FeVSb half-Heusler compounds by levitation melting and spark plasma sintering. *Intermetallics, 32*: 39-43.

Gao, X., Uehara, K., Klug, D. D. and Tse, J. S. (2006). Rational design of high-efficiency thermoelectric materials with low band gap conductive polymers. *Computational Materials Science, 36*(1-2): 49-53.

Gao, Y., Ying, P., Cui, J., Chen, S. and Li, Y. (2012). Thermoelectric Properties of Cu and Sb Co-Doped Ga-Te Based Semiconductor with Wide Band Gap. *Procedia Engineering, 27*: 156-162.

Gonçalves, A. P., Lopes, E. B., Delaizir, G., Vaney, J. B., Lenoir, B., Piarristeguy, A., Pradel, A., Monnier, J., Ochin, P. and Godart, C. (2012). Semiconducting glasses: A new class of thermoelectric materials? *Journal of Solid State Chemistry, 193*: 26-30.

Gonçalves, A. P., Lopes, E. B., Rouleau, O. and Godart, C. (2010). Conducting glasses as new potential thermoelectric materials: the Cu–Ge–Te case. *Journal of Materials Chemistry, 20*(8): 1516.

Gou, X. L., Yang, S. W., Xiao, H. and Ou, Q. (2013). A dynamic model for thermoelectric generator applied in waste heat recovery. *Energy, 52*: 201-209.

Graff, J. W., Zeng, X., Dehkordi, A. M., He, J. and Tritt, T. M. (2014). Exceeding the filling fraction limit in CoSb3 skutterudite: multi-role chemistry of praseodymium leading to promising thermoelectric performance. *Journal of Materials Chemistry A, 2*(23): 8933.

Graff, J., Zhu, S., Holgate, T., Peng, J., He, J. and Tritt, T. M. (2011). High-Temperature Thermoelectric Properties of Co_4Sb_{12}-Based Skutterudites with Multiple Filler Atoms: $Ce_{0.1}In_xYb_yCo_4Sb_{12}$. *Journal of Electronic Materials, 40*(5): 696-701.

Group, Ad-hoc Working. (2010). Critical Raw Materials for the EU: European Commission.

Grytsiv, A., Rogl, P., Berger, S., Paul, C., Michor, H., Bauer, E., Hilscher, G., Lottermoser, W., Saccone, A., Ferro, R. and Noel, H. (2003). Novel thermoelectric skutterudites $Sn_yNi_4Sb_{12-x}Sn_x$. *Physica B-Condensed Matter, 328*(1-2): 71-73.

Harman, T. C., Taylor, P. J., Walsh, M. P. and LaForge, B. E. (2002). Quantum dot superlattice thermoelectric materials and devices. *Science, 297*(5590): 2229-2232.

He, W., Su, Y. H., Wang, Y. Q., Riffat, S. B. and Ji, J. (2012). A study on incorporation of thermoelectric modules with evacuated-tube heat-pipe solar collectors. *Renewable Energy, 37*(1): 142-149.

Hirota, M., Nakajima, Y., Saito, M. and Uchiyama, M. (2007). 120×90 element thermoelectric infrared focal plane array with precisely patterned Au-black absorber. *Sensors and Actuators A: Physical, 135*(1): 146-151.

Hochbaum, A. I., Chen, R., Delgado, R. D., Liang, W., Garnett, E. C., Najarian, M., Majumdar, A. and Yang, P. (2008). Enhanced thermoelectric performance of rough silicon nanowires. *Nature, 451*(7175): 163-167.

Hong, S. J., Lee, S. H. and Chun, B. S. (2003). Thermoelectric properties of newly fabricated n-type 95%Bi_2Te_2-5%Bi_2Se_3 alloys by gas atomizing and extrusion process. *Materials Science and Engineering B-Solid State Materials for Advanced Technology, 98*(3): 232-238.

Hornbostel, M. D., Hyer, E. J., Thiel, J. and Johnson, D. C. (1997). Rational synthesis of metastable skutterudite compounds using multilayer precursors. *Journal of the American Chemical Society, 119*(11): 2665-2668.

Hsu, C. T., Huang, G. Y., Chu, H. S., Yu, B. and Yao, D. J. (2011). Experiments and simulations on low-temperature waste heat harvesting system by thermoelectric power generators. *Applied Energy, 88*(4): 1291-1297.

Huang, H. S., Weng, Y. C., Chang, Y. W., Chen, S. L. and Ke, M. T. (2010). Thermoelectric water-cooling device applied to electronic equipment. *International Communications in Heat and Mass Transfer, 37*(2): 140-146.

Huang, J. . (2009). Aerospace and Aircraft Thermoelectric Applications, The Boeing Company, Thermoelectrics Applications Workshop. San Diego, CA.

Huang, M. J., Chou, P. K. and Lin, M. C. (2006). Thermal and thermal stress analysis of a thin-film thermoelectric cooler under the influence of the Thomson effect. *Sensors and Actuators a-Physical, 126*(1): 122-128.

Hummel, R. E. . (2011). *Electronic Properties of Materials*

Ihring, A., Kessler, E., Dillner, U., Haenschke, F., Schinkel, U. and Meyer, H. G. (2011). Surface-micromachined thermoelectric infrared focal-plane array with high detectivity for room temperature operation. *Microelectronic Engineering, 88*(8): 2267-2271.

Ito, M. and Furumoto, D. (2008). Effects of noble metal addition on microstructure and thermoelectric properties of $Na_xCo_2O_4$. *Journal of Alloys and Compounds, 450*(1-2): 494-498.

Iversen, B. B., Palmqvist, A. E. C., Cox, D. E., Nolas, G. S., Stucky, G. D., Blake, N. P. and Metiu, H. (2000). Why are Clathrates Good Candidates for Thermoelectric Materials? *Journal of Solid State Chemistry, 149*(2): 455-458.

Jacobs, T., Kutzner, C., Kropp, M., Brokmann, G., Lang, W., Steinke, A., Kienle, A. and Hauptmann, P. (2009). Combination of a novel perforated thermoelectric flow and impedimetric sensor for monitoring chemical conversion in micro fluidic channels. *Proceedings of the Eurosensors Xxiii Conference, 1*(1): 1127-1130.

Jacobs, T., Kutzner, C., Kropp, M., Lang, W., Kienle, A. and Hauptmann, P. (2009). Novel pressure stable thermoelectric flow sensor in non-steady state operation mode for inline process analysis in micro reactors. *Proceedings of the Eurosensors Xxiii Conference, 1*(1): 148-151.

Joshi, G., Lee, H., Lan, Y., Wang, X., Zhu, G., Wang, D., Gould, R. W., Cuff, D. C., Tang, M. Y., Dresselhaus, M. S., Chen, G. and Ren, Z. (2008). Enhanced thermoelectric figure-of-merit in nanostructured p-type silicon germanium bulk alloys. *Nano Lett, 8*(12): 4670-4674.

Jung, D. Y., Kurosaki, K., Kim, C. E., Muta, H. and Yamanaka, S. (2010). Thermal expansion and melting temperature of the half-Heusler compounds: MNiSn (M=Ti, Zr, Hf). *Journal of Alloys and Compounds, 489*(2): 328-331.

Jung, J. Y., Ur, S. C. and Kim, I. H. (2008). Thermoelectric properties of $In_zCo_4Sb_{12-y}Te_y$ skutterudites. *Materials Chemistry and Physics, 108*(2-3): 431-434.

Kalkan, N., Young, E. A. and Celiktas, A. (2012). Solar thermal air conditioning technology reducing the footprint of solar thermal air conditioning. *Renewable & Sustainable Energy Reviews, 16*(8): 6352-6383.

Karl, N. (2003). Charge carrier transport in organic semiconductors. *Synthetic Metals, 133*: 649-657.

Karri, M. A., Thacher, E. F. and Helenbrook, B. T. (2011). Exhaust energy conversion by thermoelectric generator: Two case studies. *Energy Conversion and Management, 52*(3): 1596-1611.

Kawaharada, Y., Kuroaski, K., Uno, M. and Yamanaka, S. (2001). Thermoelectric properties of $CoSb_3$. *Journal of Alloys and Compounds, 315*(1-2): 193-197.

Kawaharada, Y., Kurosaki, K., Muta, H., Uno, M. and Yamanaka, S. (2004). High temperature thermoelectric properties of $CoNb_{1-x}Hf_xSn_{1-y}Sb_y$ half-Heusler compounds. *Journal of Alloys and Compounds, 377*(1-2): 312-315.

Kenfaui, D., Chateigner, D., Gomina, M. and Noudem, J. G. (2010). Texture, mechanical and thermoelectric properties of $Ca_3Co_4O_9$ ceramics. *Journal of Alloys and Compounds, 490*(1-2): 472-479.

Khan, A., Saleemi, M., Johnsson, M., Han, L., Nong, N. V., Muhammed, M. and Toprak, M. S. (2014). Fabrication, spark plasma consolidation, and thermoelectric evaluation of nanostructured CoSb3. *Journal of Alloys and Compounds, 612*: 293-300.

Kim, I. H., Park, K. H. and Ur, S. C. (2007). Thermoelectric properties of Sn-doped $CoSb_3$ prepared by encapsulated induction melting. *Journal of Alloys and Compounds, 442*(1-2): 351-354.

Kim, M. J. and Kim, I. H. (2010). Electronic transport properties of Te-doped $CoSb_3$ skutterudites prepared by hot pressing. *Metals and Materials International, 16*(3): 459-463.

Kim, S. W., Kimura, Y. and Mishima, Y. (2003). Effects of doping on the high-temperature thermoelectric properties of $IrSb_3$ skutterudite compounds. *Journal of Electronic Materials, 32*(11): 1141-1147.

Kim, S. W., Kimura, Y. and Mishima, Y. (2004). Effect of partial La filling on high-temperature thermoelectric properties of $IrSb_3$-based skutterudite compounds. *Journal of Electronic Materials, 33*(10): 1156-1160.

Kim, T. S. and Chun, B. S. (2007). Microstructure and thermoelectric properties of n- and p-type Bi_2Te_3 alloys by rapid solidification processes. *Journal of Alloys and Compounds, 437*(1-2): 225-230.

Kitagawa, H., Wakatsuki, M., Nagaoka, H., Noguchi, H., Isoda, Y., Hasezaki, K. and Noda, Y. (2005). Temperature dependence of thermoelectric properties of Ni-doped $CoSb_3$. *Journal of Physics and Chemistry of Solids, 66*(10): 1635-1639.

Kleinke, H. (2010). New bulk Materials for Thermoelectric Power Generation: Clathrates and Complex Antimonides. *Chemistry of Materials, 22*(3): 604-611.

Kopparthy, V. L., Tangutooru, S. M., Nestorova, G. G. and Guilbeau, E. J. (2012). Thermoelectric microfluidic sensor for bio-chemical applications. *Sensors and Actuators B-Chemical, 166*: 608-615.

Kousksou, T., Bedecarrats, J. P., Champier, D., Pignolet, P. and Brillet, C. (2011). Numerical study of thermoelectric power generation for an helicopter conical nozzle. *Journal of Power Sources, 196*(8): 4026-4032.

Kowalczyk, A., Falkowski, M., Tolinski, T., Tran, V. H., Miiller, W., Reiffers, M. and Timko, M. (2008). Specific heat, electrical resistivity and thermoelectric power of $YbNi_4Si$. *Materials Research Bulletin, 43*(1): 185-190.

Kozlov, A. G. (1999). Optimization of thin-film thermoelectric radiation sensor with comb thermoelectric transducer. *Sensors and Actuators a-Physical, 75*(2): 139-150.

Kozlov, A. G. (2000). Optimization of thin-film thermoelectric radiation sensor with separate disposition of absorbing layer and comb thermoelectric transducer. *Sensors and Actuators a-Physical, 84*(3): 259-269.

Kraemer, D., McEnaney, K., Chiesa, M. and Chen, G. (2012). Modeling and optimization of solar thermoelectric generators for terrestrial applications. *Solar Energy, 86*(5): 1338-1350.

Lange, R. G. and Carroll, W. P. (2008). Review of recent advances of radioisotope power systems. *Energy Conversion and Management, 49*(3): 393-401.

Laufek, F., Navratil, J., Plasil, J., Plechacek, T. and Drasar, C. (2009). Synthesis, crystal structure and transport properties of skutterudite-related $CoSn_{1.5}Se_{1.5}$. *Journal of Alloys and Compounds, 479*(1-2): 102-106.

Lee, P. J. and Chao, L. S. (2010). High-temperature thermoelectric properties of $Ti_{0.5}(ZrHf)_{0.5-x}Nb_xNi_{0.9}Pd_{0.1}Sn_{0.98}Sb_{0.02}$ half-Heusler alloys. *Journal of Alloys and Compounds, 504*(1): 192-196.

Li, F. and Li, J. F. (2011). Effect of Ni substitution on electrical and thermoelectric properties of $LaCoO_3$ ceramics. *Ceramics International, 37*(1): 105-110.

Li, F. M., Waddingham, R., Milne, W. I., Flewitt, A. J., Speakman, S., Dutson, J., Wakeham, S. and Thwaites, M. (2011). Low temperature (<100°C) deposited P-type cuprous oxide thin films: Importance of controlled oxygen and deposition energy. *Thin Solid Films, 520*(4): 1278-1284.

Li, G., Kurosaki, K., Ohishi, Y., Muta, H. and Yamanaka, S. (2012). Thermoelectric Properties of Indium-Added Skutterudites $In_xCo_4Sb_{12}$. *Journal of Electronic Materials, 42*(7): 1463-1468.

Li, H., Tang, X. and Zhang, Q. (2009). Microstructure and Thermoelectric Properties of Yb-Filled Skutterudites Prepared by Rapid Solidification. *Journal of Electronic Materials, 38*(7): 1224-1228.

Liu, D., Zhao, F. Y. and Tang, G. F. (2010). Active low-grade energy recovery potential for building energy conservation. *Renewable & Sustainable Energy Reviews, 14*(9): 2736-2747.

Liu, H. J., Song, C. M., Wu, S. T. and Li, L. F. (2007). Processing method dependency of thermoelectric properties of $Bi_{85}Sb_{15}$ alloys in low temperature. *Cryogenics, 47*(1): 56-60.

Liu, H. Q., Zhou, G., Sun, Q., Gu, Y. J. and Zhao, X. B. (2011). Thermoelectric Properties of $xPbTe/Yb_{0.2}Co_4Sb_{12}$ Hot-Pressed Samples. *Journal of Inorganic and Organometallic Polymers and Materials, 21*(4): 858-861.

Liu, J., Wang, C. L., Su, W. B., Wang, H. C., Li, J. C., Zhang, J. L. and Mei, L. M. (2010). Thermoelectric properties of $Sr_{1-x}Nd_xTiO_3$ ceramics. *Journal of Alloys and Compounds, 492*(1-2): L54-L56.

Liu, K. G., Dong, X. and Zhang, J. X. (2006). The effects of La on thermoelectric properties of $La_xCo_4Sb_{12}$ prepared by MA-SPS. *Materials Chemistry and Physics, 96*(2-3): 371-375.

Liu, S. H., Wang, J., Jia, J. F., Hu, X. and Liu, S. J. (2012). Synthesis and thermoelectric performance of Li-doped NiO ceramics. *Ceramics International, 38*(6): 5023-5026.

Lu, P. X., Wu, F., Han, H. L., Wang, Q. A., Shen, Z. G. and Hu, X. (2010). Thermoelectric properties of rare earths filled $CoSb_3$ based nanostructure skutterudite. *Journal of Alloys and Compounds, 505*(1): 255-258.

Luo, T. T., Wang, S. Y., Li, H. and Tang, X. F. (2013). Low temperature thermoelectric properties of melt spun $Bi_{85}Sb_{15}$ alloys. *Intermetallics, 32*: 96-102.

Luo, Wenhui, Li, Han, Yan, Yonggao, Lin, Zebing, Tang, Xinfeng, Zhang, Qinjie and Uher, Ctirad. (2011). Rapid synthesis of high thermoelectric performance higher manganese silicide with in-situ formed nano-phase of MnSi. *Intermetallics, 19*(3): 404-408.

Ma, Y., Hao, Q., Poudel, B., Lan, Y. C., Yu, B., Wang, D. Z., Chen, G. and Ren, Z. F. (2008). Enhanced thermoelectric figure-of-merit in p-type nanostructured bismuth antimony tellurium alloys made from elemental chunks. *Nano Letters, 8*(8): 2580-2584.

Maji, P., Takas, N. J., Misra, D. K., Gabrisch, H., Stokes, K. and Poudeu, P. F. P. (2010). Effects of Rh on the thermoelectric performance of the p-type $Zr_{0.5}Hf_{0.5}Co_{1-x}Rh_xSb_{0.99}Sn_{0.01}$ half-Heusler alloys. *Journal of Solid State Chemistry, 183*(5): 1120-1126.

Majumdar, A. (2004). Materials science. Thermoelectricity in semiconductor nanostructures. *Science, 303*(5659): 777-778.

Mallik, R. C., Anbalagan, R., Raut, K. K., Bali, A., Royanian, E., Bauer, E., Rogl, G. and Rogl, P. (2013). Thermoelectric properties of Bi-added Co4Sb12 skutterudites. *J Phys Condens Matter, 25*(10): 105701.

Mallik, R. C., Jung, J. Y., Das, V. D., Ur, S. C. and Kim, I. H. (2007). Thermoelectric properties of $Sn_zCo_8Sb_{24}$ skutterudites. *Solid State Communications, 141*(4): 233-237.

Mallik, R. C., Jung, J. Y., Ur, S. C. and Kim, I. H. (2008). Thermoelectric properties of $In_zCo_4Sb_{12}$ skutterudites. *Metals and Materials International, 14*(2): 223-228.

Mallik, R. C., Stiewe, C., Karpinski, G., Hassdorf, R. and Muller, E. (2009). Thermoelectric Properties of Co_4Sb_{12} Skutterudite Materials with Partial In Filling and Excess In Additions. *Journal of Electronic Materials, 38*(7): 1337-1343

Martín-González, M., Caballero-Calero, O. and Díaz-Chao, P. (2013). Nanoengineering thermoelectrics for 21st century: Energy harvesting and other trends in the field. *Renewable and Sustainable Energy Reviews, 24*: 288-305.

Martin, J., Wang, Li, Chen, Lidong and Nolas, G. S. (2009). Enhanced Seebeck coefficient through energy-barrier scattering in PbTe nanocomposites. *Physical Review B, 79*(11).

Matsuoka, E., Morimoto, S., Tanaka, K., Sasakawa, T. and Takabatake, T. (2006). Magnetic and thermoelectric properties of $Ba_yFe_{4-x}Co_xSb_{12}$. *Physica B-Condensed Matter, 383*(1): 132-133.

Meng, F., Chen, L. and Sun, F. (2011). Performance Prediction and Irreversibility Analysis of a Thermoelectric Refrigerator with Finned Heat Exchanger. *Acta Physica Polonica A, 120*(3): 397-406.

Mi, J. L., Zhao, X. B., Zhu, T. J., Tu, J. P. and Cao, G. S. (2006). Solvothermal synthesis and electrical transport properties of skutterudite $CoSb_3$. *Journal of Alloys and Compounds, 417*(1-2): 269-272.

Mikhnovich Jr., V. V. (2001). Scattering of charge carriers in semiconductors: models and their criteria. *Physica, B 308–310*: 1023–1026.

Miljkovic, N. and Wang, E. N. (2011). Modeling and optimization of hybrid solar thermoelectric systems with thermosyphons. *Solar Energy, 85*(11): 2843-2855.

Moon, C., Shin, S., Kim, D. and Kim, T. S. (2010). Microstructure and thermoelectric properties of p-type Bi_2Te_3-Sb_2Te_3 alloys produced by rapid solidification and spark plasma sintering. *Journal of Alloys and Compounds, 504*: S504-S507.

Mülller, M., Budde, W., Gotffried-Gottfried, R., Hübel, A., Jähne, R. and Kück, H. (1996). A thermoelectric infrared radiation sensor with monolithically integrated amplifier stage and temperature sensor. *Sensors and Aaualors A, 54* 601-605.

Nag, B. R. (1995). Direct-Band-Gap Energy of Semiconductors. *Infrared Physics & Technology, 36*(5): 831-835.

Nakagawa, T., Sakaguchi, I., Matsunaga, K., Yamamoto, T., Haneda, H. and Ikuhara, Y. (2005). Control of point defects and grain boundaries in advanced materials optical properties and diffusion induced by Li doping in ZnO. *Nuclear Instruments & Methods in Physics Research Section B-Beam Interactions with Materials and Atoms, 232*(1-4): 343-347.

Niu, X., Yu, J. L. and Wang, S. Z. (2009). Experimental study on low-temperature waste heat thermoelectric generator. *Journal of Power Sources, 188*(2): 621-626.

Nolas, G. S., Morelli, D. T. and Tritt, T. M. (1999). Skutterudites: A phonon-glass-electron crystal approach to advanced thermoelectric energy conversion applications. *Annual Review of Materials Science, 29*: 89-116.

Nolas, G. S., Yoon, G., Sellinschegg, H., Smalley, A. and Johnson, D. C. (2005). Synthesis and transport properties of HfF_4Sb_{12}. *Applied Physics Letters, 86*(4): 042111.

Noudem, J. G., Lemonnier, S., Prevel, M., Reddy, E. S., Guilmeau, E. and Goupil, C. (2008). Thermoelectric ceramics for generators. *Journal of the European Ceramic Society, 28*(1): 41-48.

Nylén, J., Lidin, S., Andersson, M., Liu, H., Newman, N. and Häussermann, U. (2007). Effect of metal doping on the low-temperature structural behavior of thermoelectric β-Zn_4Sb_3. *Journal of Solid State Chemistry, 180*(9): 2603-2615.

O'Brien, R. C., Ambrosi, R. M., Bannister, N. P., Howe, S. D. and Atkinson, H. V. (2008). Safe radioisotope thermoelectric generators and heat sources for space applications. *Journal of Nuclear Materials, 377*(3): 506-521.

Omar, M. S. and Gorges, F. Y. (2006). The optical energy gap dependence on both carrier concentration and intrinsic energy gap in n-type semiconductors. *Materials Science in Semiconductor Processing, 9*(1-3): 164-167.

Omer, A. M. (2008). Focus on low carbon technologies: The positive solution. *Renewable & Sustainable Energy Reviews, 12*(9): 2331-2357.

Omer, S. A. and Infield, D. G. (1998). Design optimization of thermoelectric devices for solar power generation. *Solar Energy Materials and Solar Cells, 53*(1-2): 67-82.

Omer, S. A. and Infield, D. G. (2000). Design and thermal analysis of a two stage solar concentrator for combined heat and thermoelectric power generation. *Energy Conversion and Management, 41*(7): 737-756.

Ozpineci, B. and Tolbert, L. M. . (2003). Comparison of wide-bandgap semiconductors for power electronics applications: Oak Ridge National Laboratory.

Park, K-H., Seo, W-S., Choi, S-M. and Kim, I-H. (2014). Thermal stability of the thermoelectric skutterudite $In_{0.25}Co_3MnSb_{12}$. *Journal of the Korean Physical Society, 64*(1): 79-83.

Park, Kwan-Ho and Kim, Il-Ho. (2010). Thermoelectric Properties of Ca-Filled $CoSb_3$-Based Skutterudites Synthesized by Mechanical Alloying. *Journal of Electronic Materials, 40*(5): 493-498.

Pei, Y. Z., Bai, S. Q., Zhao, X. Y., Zhang, W. and Chen, L. D. (2008). Thermoelectric properties of $Eu_yCo_4Sb_{12}$ filled skutterudites. *Solid State Sciences, 10*(10): 1422-1428.

Peng, J. Y., He, J., Alboni, P. N. and Tritt, T. M. (2009). Synthesis and Thermoelectric Properties of the Double-Filled Skutterudite $Yb_{0.2}In_{(y)}Co_4Sb_{12}$. *Journal of Electronic Materials, 38*(7): 981-984.

Peng, J. Y., Yang, J. Y., Zhang, T. J., Song, X. L. and Chen, Y. H. (2004). Preparation and characterization of Fe substituted $CoSb_3$ skutterudite by mechanical alloying and annealing. *Journal of Alloys and Compounds, 381*(1-2): 313-316.

Pichanusakorn, P. and Bandaru, P. (2010). Nanostructured thermoelectrics. *Materials Science & Engineering R-Reports, 67*(2-4): 19-63.

Ploteau, J. P., Glouannec, P. and Noel, H. (2007). Conception of thermoelectric flux meters for infrared radiation measurements in industrial furnaces. *Applied Thermal Engineering, 27*(2-3): 674-681.

Ponnambalam, V., Morelli, Donald T., Bhattacharya, S. and Tritt, Terry M. (2013). The role of simultaneous substitution of Cr and Ru on the thermoelectric properties of defect manganese silicides $MnSi_\delta$ ($1.73<\delta<1.75$). *Journal of Alloys and Compounds, 580*: 598-603.

PrezAparicio, J. L., Palma, R. and Taylor, R. L. (2012). Finite element analysis and material sensitivity of Peltier thermoelectric cells coolers. *International Journal of Heat and Mass Transfer, 55*(4): 1363-1374.

Prokhorov, V. M. and Pivovarov, G. I. (2011). Detection of internal cracks and ultrasound characterization of nanostructured Bi(2)Te(3)-based thermoelectrics via acoustic microscopy. *Ultrasonics, 51*(6): 715-718.

Putra, N., Yanuar and Iskandar, F. N. (2011). Application of nanofluids to a heat pipe liquid-block and the thermoelectric cooling of electronic equipment. *Experimental Thermal and Fluid Science, 35*(7): 1274-1281.

Ramdas, A. K., Rodriguez, S., Tsoi, S. and Haller, E. E. (2005). Electronic band gaps of semiconductors as influenced by their isotopic composition. *Solid State Communications, 133*(11): 709-714.

Ravot, D., Lafont, U., Chapon, L., Tedenac, J. C. and Mauger, A. (2001). Anomalous physical properties of cerium-lanthanum filled skutterudites. *Journal of Alloys and Compounds, 323*: 389-391.

Recknagel, C., Reinfried, N., Hohn, P., Schnelle, W., Rosner, H., Grin, Y. and Leithe-Jasper, A. (2007). Application of spark plasma sintering to the fabrication of binary and ternary skutterudites. *Science and Technology of Advanced Materials, 8*(5): 357-363.

Ren, F., Case, E. D., Timm, E. J. and Schock, H. J. (2008). Hardness as a function of composition for n-type LAST thermoelectric material. *Journal of Alloys and Compounds, 455*(1-2): 340-345.

Riffat, S. B. and Ma, X. L. (2003). Thermoelectrics: a review of present and potential applications. *Applied Thermal Engineering, 23*(8): 913-935.

Riffat, S. B. and Qiu, G. Q. (2004). Comparative investigation of thermoelectric air-conditioners versus vapour compression and absorption air-conditioners. *Applied Thermal Engineering, 24*(14-15): 1979-1993.

Rinehart, G. H. (2001). Design characteristics and fabrication of radioisotope heat sources for space missions. *Progress in Nuclear Energy, 39*(3-4): 305-319.

Rogl, G., Aabdin, Z., Schafler, E., Horky, J., Setman, D., Zehetbauer, M., Kriegisch, M., Eibl, O., Grytsiv, A., Bauer, E., Reinecker, M., Schranz, W. and Rogl, P. (2012). Effect of HPT processing on the structure, thermoelectric and mechanical properties of $Sr_{0.07}Ba_{0.07}Yb_{0.07}Co_4Sb_{12}$. *Journal of Alloys and Compounds, 537*: 183-189.

Rogl, G., Grytsiv, A., Rogl, P., Bauer, E. and Zehetbauer, M. (2011). A new generation of p-type didymium skutterudites with high ZT. *Intermetallics, 19*(4): 546-555.

Roudebush, J. H., Toberer, E. S., Hope, H., Snyder, G. J. and Kauzlarich, S. M. (2011). Crystal structure, characterization and thermoelectric properties of the type-I clathrate $Ba_{8-y}Sr_yAl_{14}Si_{32}$ ($0.6 <= y <= 1.3$) prepared by aluminum flux. *Journal of Solid State Chemistry, 184*(5): 1176-1185.

Saidur, R., Rezaei, M., Muzammil, W. K., Hassan, M. H., Paria, S. and Hasanuzzaman, M. (2012). Technologies to recover exhaust heat from internal combustion engines. *Renewable & Sustainable Energy Reviews, 16*(8): 5649-5659.

Saleemi, M., Famengo, A., Fiameni, S., Boldrini, S., Battiston, S., Johnsson, M., Muhammed, M. and Toprak, M. S. (2015). Thermoelectric performance of higher manganese silicide nanocomposites. *Journal of Alloys and Compounds, 619*: 31-37.

Sano, S. , Mizukami, H. and Kaibe, H. (2003). Development of High-Efficiency Thermoelectric Power Generation System (Vol. 49): KOMAT'SU.

Sawaguchi, N., Shin, W., Izu, N., Matsubara, I. and Murayama, N. (2005). Effect of humidity on the sensing property of thermoelectric hydrogen sensor. *Sensors and Actuators B-Chemical, 108*(1-2): 461-466.

Shen, L. M., Xiao, F., Chen, H. X. and Wang, S. W. (2013). Investigation of a novel thermoelectric radiant air-conditioning system. *Energy and Buildings, 59*: 123-132.

Shi, X., Salvador, J. R., Yang, J. and Wang, H. (2009). Thermoelectric Properties of n-Type Multiple-Filled Skutterudites. *Journal of Electronic Materials, 38*(7): 930-933.

Shi, X., Yang, J., Salvador, J. R., Chi, M., Cho, J. Y., Wang, H., Bai, S., Yang, J., Zhang, W. and Chen, L. (2011). Multiple-filled skutterudites: high thermoelectric figure of merit through separately optimizing electrical and thermal transports. *J Am Chem Soc, 133*(20): 7837-7846.

Shu, G. Q., Liang, Y. C., Wei, H. Q., Tian, H., Zhao, J. and Liu, L. N. (2013). A review of waste heat recovery on two-stroke IC engine aboard ships. *Renewable & Sustainable Energy Reviews, 19*: 385-401.

Shutoh, N. and Sakurada, S. (2005). Thermoelectric properties of the $Ti_x(Zr_{0.5}Hf_{0.5})_{1-x}NiSn$ half-Heusler compounds. *Journal of Alloys and Compounds, 389*(1-2): 204-208.

Sion, C., Godts, P., Ziouche, K., Bougrioua, Z., Lasri, T. and Leclercq, D. (2012). Unpackaged infrared thermoelectric microsensor realised on suspended membrane by silicon technology. *Sensors and Actuators a-Physical, 175*: 78-86.

Sklad, A. C., Gaultois, M. W. and Grosvenor, A. P. (2010). Examination of $CeFe_4Sb_{12}$ upon exposure to air: Is this material appropriate for use in terrestrial, high-temperature thermoelectric devices? *Journal of Alloys and Compounds, 505*(1): L6-L9.

Snyder, G. J. (Fall 2008). *Small Thermoelectric Generators*. Paper presented at the Interface.

Snyder, G. J. and Toberer, E. S. (2008). Complex thermoelectric materials. *Nature materials, 7*(2): 105-114.

Song, X. L., Yang, J. Y., Peng, J. Y., Chen, Y. H., Zhu, W. and Zhang, T. J. (2005). Thermoelectric properties of La filled skutterudite prepared by mechanical alloying and hot pressing. *Journal of Alloys and Compounds, 399*(1-2): 276-279.

Sootsman, J. R., Chung, D. Y. and Kanatzidis, M. G. (2009). New and old concepts in thermoelectric materials. *Angew Chem Int Ed Engl, 48*(46): 8616-8639.

Stachowiak, H., Lassue, S., Dubernard, A. and Gaviot, E. (1998). A thermoelectric sensor for fluid flow measurement. principles, calibration and solution for self temperature compensation. *Flow Measurement and Instrumentation, 9*(3): 135-141.

Suter, C., Tomes, P., Weidenkaff, A. and Steinfeld, A. (2010). Heat Transfer and Geometrical Analysis of Thermoelectric Converters Driven by Concentrated Solar Radiation. *Materials, 3*(4): 2735-2752.

Tachibana, M. and Fang, J. (2012). An Estimation of Thermal Stress of Thermoelectric Devices in the Temperature Cycling Test. *Procedia Engineering, 27*: 177-185.

Tajima, S., Tani, T., Isobe, S. and Koumoto, K. (2001). Thermoelectric properties of highly textured $NaCo_2O_4$ ceramics processed by the reactive templated grain growth (RTGG) method. *Materials Science and Engineering B-Solid State Materials for Advanced Technology, 86*(1): 20-25.

Tan, G. J., Wang, S. Y., Yan, Y. G., Li, H. and Tang, X. F. (2012). Enhanced thermoelectric performance in p-type $Ca_{0.5}Ce_{0.5}Fe_{4-x}Ni_xSb_{12}$ skutterudites by adjusting the carrier concentration. *Journal of Alloys and Compounds, 513*: 328-333.

Tani, J. and Kido, H. (2005). Thermoelectric properties of Bi-doped Mg_2Si semiconductors. *Physica B-Condensed Matter, 364*(1-4): 218-224.

TE Technology, Inc. (2010). Peltier - Thermoelectric Modules. Retrieved 11.09, 2013, from http://www.tetech.com/FAQ-Technical-Information.html

Terasaki, I. (2003). Transport properties and electronic states of the thermoelectric oxide $NaCo_2O_4$. *Physica B-Condensed Matter, 328*(1-2): 63-67.

Thirugnanasambandam, M., Iniyan, S. and Goic, R. (2010). A review of solar thermal technologies. *Renewable & Sustainable Energy Reviews, 14*(1): 312-322.

Tie, S. F. and Tan, C. W. (2013). A review of energy sources and energy management system in electric vehicles. *Renewable & Sustainable Energy Reviews, 20*: 82-102.

Tritt, T. M. and Subramanian, M. A. (2006). Thermoelectric materials, phenomena, and applications: A bird's eye view. *Mrs Bulletin, 31*(3): 188-194.

Tsai, T. C., Chang, H. C., Chen, C. H. and Whang, W. T. (2011). Widely variable Seebeck coefficient and enhanced thermoelectric power of PEDOT:PSS films by blending thermal decomposable ammonium formate. *Organic Electronics, 12*(12): 2159-2164.

Tsubota, T., Ohno, T., Shiraishi, N. and Miyazaki, Y. (2008). Thermoelectric properties of $Sn_{1-x-y}Ti_ySb_xO_2$ ceramics. *Journal of Alloys and Compounds, 463*(1-2): 288-293.

Uberuaga, B. P., Henkelman, G., Jonsson, H., Dunham, S. T., Windl, W. and Stumpf, R. (2002). Theoretical studies of self-diffusion and dopant clustering in semiconductors. *Physica Status Solidi B-Basic Research, 233*(1): 24-30.

Ullah, K. R., Saidur, R., Ping, H. W., Akikur, R. K. and Shuvo, N. H. (2013). A review of solar thermal refrigeration and cooling methods. *Renewable & Sustainable Energy Reviews, 24*: 499-513.

Ur, S. C., Kwon, J. C. and Kim, I. H. (2007). Thermoelectric properties of Fe-doped $CoSb_3$ prepared by mechanical alloying and vacuum hot pressing. *Journal of Alloys and Compounds, 442*(1-2): 358-361.

Van Herwaarden, A. W. and Sarro, P. M. (1986). Thermal sensors based on the seebeck effect. *Sensors and Actuators A: Physical, 10*(3-4): 321-346.

Vancauwenberghe, O., Short, J., Giehler, E., Bildstein, P., Ancey, P. and Gschwind, M. (1996). Microsensor for the preventive detection of water condensation: Operating principle and interface electronics. *Sensors and Actuators a-Physical, 53*(1-3): 304-308.

Vaqueiro, P., Sobany, G. G., Powell, A. V. and Knight, K. S. (2006). Structure and thermoelectric properties of the ordered skutterudite $CoGe_{1.5}Te_{1.5}$. *Journal of Solid State Chemistry, 179*(7): 2047-2053.

Vélez, F., Segovia, J. J., Martín, M. C., Antolín, G., Chejne, F. and Quijano, A. (2012). A technical, economical and market review of organic Rankine cycles for the conversion of low-grade heat for power generation. *Renewable and Sustainable Energy Reviews, 16*(6): 4175-4189.

Venkatasubramanian, R., Siivola, E., Colpitts, T. and O'Quinn, B. (2001). Thin-film thermoelectric devices with high room-temperature figures of merit. *Nature, 413*(6856): 597-602.

Vullers, R. J. M., Van Schaijk, R., Doms, I., Van Hoof, C. and Mertens, R. (2009). Micropower energy harvesting. *Solid-State Electronics, 53*(7): 684-693.

Wan, C., Wang, Y., Wang, N. and Koumoto, K. (2010). Low-Thermal-Conductivity $(MS)_{1+x}(TiS2)_2$ (M = Pb, Bi, Sn) Misfit Layer Compounds for Bulk Thermoelectric Materials. *Materials, 3*: 2606-2617.

Wang, H. C., Wang, C. L., Su, W. B., Liu, J., Zhao, Y., Peng, H., Zhang, J. L., Zhao, M. L., Li, J. C., Yin, N. and Mei, L. M. (2010). Enhancement of thermoelectric figure of merit by doping Dy in $La_{0.1}Sr_{0.9}TiO_3$ ceramic. *Materials Research Bulletin, 45*(7): 809-812.

Wang, L. M., Chang, C. Y., Yeh, S. T., Chen, S. W., Peng, Z. A., Bair, S. C., Lee, D. S., Liao, F. C. and Kuo, Y. K. (2012). Synthesis and post-annealing effects on the transport properties of thermoelectric oxide $(ZnO)mIn_2O_3$ ceramics. *Ceramics International, 38*(2): 1167-1174.

Wang, N., He, H. C., Li, X. A., Han, L. and Zhang, C. Q. (2010). Enhanced thermoelectric properties of Nb-doped $SrTiO_3$ polycrystalline ceramic by titanate nanotube addition. *Journal of Alloys and Compounds, 506*(1): 293-296.

Wang, S., Fu, F., She, X., Zheng, G., Li, H. and Tang, X. (2011). Optimizing thermoelectric performance of Cd-doped β-Zn_4Sb_3 through self-adjusting carrier concentration. *Intermetallics, 19*(12): 1823-1830.

Wang, S. H., Cheng, H. M., Wu, R. J. and Chao, W. H. (2010). Structural and thermoelectric properties of HfNiSn half-Heusler thin films. *Thin Solid Films, 518*(21): 5901-5904.

Wang, T. Y., Zhang, Y. J., Peng, Z. J. and Shu, G. Q. (2011). A review of researches on thermal exhaust heat recovery with Rankine cycle. *Renewable & Sustainable Energy Reviews, 15*(6): 2862-2871.

Wang, X., Yu, J. L. and Ma, M. (2013). Optimization of heat sink configuration for thermoelectric cooling system based on entropy generation analysis. *International Journal of Heat and Mass Transfer, 63*: 361-365.

Wang, Y. F., Lee, K. H., Ohta, H. and Koumoto, K. (2008). Fabrication and thermoelectric properties of heavily rare-earth metal-doped $SrO(SrTiO_3)n$ (n=1, 2) ceramics. *Ceramics International, 34*(4): 849-852.

Wanwan, L., Zechun, C., Bin, Z., Feng, Z., Hongtao, L., Wenbin, S., Jiahua, M. and Kang, S. (2006). Study on the effect of Cd-diffusion annealing on the electrical properties of CdZnTe. *Journal of Crystal Growth, 292*(1): 53-61.

Watanabe, N., Nakayama, H., Fukao, F. and Munakata, F. (2012). Effects of metal substitution on the electric and thermoelectric properties in $(Ni_{1-x}M_x)Mn_2O_4$ (M=Zn and Mg). *Thermochimica Acta, 532*: 56-59.

Wojciechowski, K. T. (2002). Effect of tellurium doping on the themoelectric propertis of CoSb3. *Materials Research Bulletin, 37*: 2023-2033.

Wojciechowski, K. T., Tobola, J. and Leszczynski, J. (2003). Thermoelectric properties and electronic structure of $CoSb_3$ doped with Se and Te. *Journal of Alloys and Compounds, 361*(1-2): 19-27.

Xi, H. X., Luo, L. G. and Fraisse, G. (2007). Development and applications of solar-based thermoelectric technologies. *Renewable & Sustainable Energy Reviews, 11*(5): 923-936.

Xiao, J. S., Yang, T. Q., Li, P., Zhai, P. C. and Zhang, Q. J. (2012). Thermal design and management for performance optimization of solar thermoelectric generator. *Applied Energy, 93*: 33-38.

Xiong, Z., Chen, X. H., Huang, X. Y., Bai, S. Q. and Chen, L. D. (2010). High thermoelectric performance of $Yb_{0.26}Co_4Sb_{12}$/yGaSb nanocomposites originating from scattering electrons of low energy. *Acta Materialia, 58*(11): 3995-4002.

Xu, Z. Y., Lan, Z. W., Zhu, G. W., Sun, K. and Yu, Z. (2012). Effects of the oxygen partial pressure during deposition on the material characteristics and magnetic properties of BaM thin films. *Journal of Alloys and Compounds, 538*: 11-15.

Yang, J. Y., Chen, Y. H., Zhu, W., Peng, J. Y., Bao, S. Q., Fan, X. A. and Duan, X. K. (2006). Effect of La filling on thermoelectric properties of $La_xCo_{3.6}Ni_{0.4}Sb_{12}$-filled skutterudite prepared by MA-HP method. *Journal of Solid State Chemistry, 179*(1): 212-216.

Yang, L., Hng, H. H., Ma, J., Zhu, T. J. and Zhao, X. B. (2010). Effects of Co:Sb Molar Ratio on Synthesis and Properties of Undoped $CoSb_3$ Prepared via a Polyol Method. *Journal of Electronic Materials, 39*(9): 1543-1548.

Yasukawa, M. and Kono, T. (2006). Preparation of dense $BaPbO_3$-based ceramics by a coprecipitation and their thermoelectric properties. *Journal of Alloys and Compounds, 426*(1-2): 420-425.

Yasukawa, M., Kono, T., Ueda, K., Yanagi, H. and Hosono, H. (2010). High-temperature thermoelectric properties of La-doped $BaSnO_3$ ceramics. *Materials Science and Engineering B-Advanced Functional Solid-State Materials, 173*(1-3): 29-32.

Yee, S. K., LeBlanc, S., Goodson, K. E. and Dames, C. (2013). $ per W metrics for thermoelectric power generation: beyond ZT. *Energy & Environmental Science, 6*(9): 2561-2571.

Yu, C. and Chau, K. T. (2009). Thermoelectric automotive waste heat energy recovery using maximum power point tracking. *Energy Conversion and Management, 50*(6): 1506-1512.

Yu, J., Zhao, W. Y., Zhou, H. Y., Wei, P. and Zhang, Q. J. (2013). Rapid preparation and thermoelectric properties of Ba and In double-filled p-type skutterudite bulk materials. *Scripta Materialia, 68*(8): 643-646.

Yue, R. R. and Xu, J. K. (2012). Poly(3,4-ethylenedioxythiophene) as promising organic thermoelectric materials: A mini-review. *Synthetic Metals, 162*(11-12): 912-917.

Zhan, G. D., Kuntz, J. D., Mukherjee, A. K., Zhu, P. X. and Koumoto, K. (2006). Thermoelectric properties of carbon nanotube/ceramic nanocomposites. *Scripta Materialia, 54*(1): 77-82.

Zhang, F. P., Lu, Q. M., Zhang, X. and Zhang, J. X. (2011). First principle investigation of electronic structure of $CaMnO_3$ thermoelectric compound oxide. *Journal of Alloys and Compounds, 509*(2): 542-545.

Zhang, H. Y., Mui, Y. C. and Tarin, M. (2010). Analysis of thermoelectric cooler performance for high power electronic packages. *Applied Thermal Engineering, 30*(6-7): 561-568.

Zhang, K. X., Qin, X. Y., Xin, H. X., Li, H. J. and Zhang, J. (2009). Transport and thermoelectric properties of nanocrystal substitutional semiconductor alloys $(Mg_{1-x}Cd_x)_3Sb_2$ doped with Ag. *Journal of Alloys and Compounds, 484*(1-2): 498-504.

Zhang, Qian, Chen, Chen, Kang, Yulong, Li, Xiaodong, Zhang, Long, Yu, Dongli, Tian, Yongjun and Xu, Bo. (2015). Structural and thermoelectric characterizations of samarium filled CoSb3 skutterudites. *Materials Letters, 143*: 41-43.

Zhao, D. G., Geng, H. R. and Teng, X. Y. (2012). Fabrication and reliability evaluation of $CoSb_3$/W-Cu thermoelectric element. *Journal of Alloys and Compounds, 517*: 198-203.

Zhao, D., Li, X., He, L., Jiang, W. and Chen, L. (2009). Interfacial evolution behavior and reliability evaluation of $CoSb_3$/Ti/Mo–Cu thermoelectric joints during accelerated thermal aging. *Journal of Alloys and Compounds, 477*(1-2): 425-431.

Zheng, J. C. (2008). Recent advances on thermoelectric materials. *Frontiers of Physics in China, 3*(3): 269-279.

Zhou, A. J., Zhao, X. B., Zhu, T. J., Yang, S. H., Dasgupta, T., Stiewe, C., Hassdorf, R. and Mueller, E. (2010). Microstructure and thermoelectric properties of SiGe-added higher manganese silicides. *Materials Chemistry and Physics, 124*(2-3): 1001-1005.

Zhou, Aijun, Cui, Hengguan, Li, Jingze, Zhu, Tiejun and Zhao, Xinbing. (2012). Bulk higher manganese silicide thermoelectric materials and modules. *Procedia Engineering, 27*: 94-102.

Zhou, D., Liu, J., Xu, S. and Peng, P. (2012). Thermal stability and elastic properties of Mg_2X (X=Si, Ge, Sn, Pb) phases from first-principle calculations. *Computational Materials Science, 51*(1): 409-414.

Zhou, X. F., Zhang, H., Chen, Q. M., Shang, J. and Zhang, P. X. (2011). Effects of annealing atmosphere on thermoelectric signals from ZnO films. *Thin Solid Films, 519*(10): 3026-3028.

Zhou, Y. Y. and Yu, J. L. (2012). Design optimization of thermoelectric cooling systems for applications in electronic devices. *International Journal of Refrigeration-Revue Internationale Du Froid, 35*(4): 1139-1144.

Zhu, T. J., Zhao, X. B., Yan, M., Hu, S. H., Li, T. and Zhou, B. C. (2000). Transport properties of β-Zn_4Sb_3 prepared by vacuum melting. *Materials Letters 46* 44–48.

Zhu, T. and Li, J. (2010). Ultra-strength materials. *Progress in Materials Science, 55*(7): 710-757.

Zide, J. M. O., Vashaee, D., Bian, Z. X., Zeng, G., Bowers, J. E., Shakouri, A. and Gossard, A. C. (2006). Demonstration of electron filtering to increase the Seebeck coefficient in $In_{0.53}Ga_{0.47}As/In_{0.53}Ga_{0.28}Al_{0.19}As$ superlattices. *Physical Review B, 74*(20): 205335.

Zou, M. M., Li, J. F. and Kita, T. (2013). Thermoelectric properties of fine-grained FeVSb half-Heusler alloys tuned to p-type by substituting vanadium with titanium. *Journal of Solid State Chemistry, 198*: 125-130.

LIST OF PUBLICATIONS AND PAPERS PRESENTED

LIST OF PUBLICATIONS:

1. Elsheikh, M. H., Shnawah, D. A., Sabri, M. F. M., Said, S. M., Hassan, M. H., Bashir, M. B. A., & Mohamad, M. (2014). A review on thermoelectric renewable energy : Principle parameters that affect their performance. Renewable and Sustainable Energy Reviews, 30, 377-355.

2. Elsheikh, M. H., Sabri, M. F. M., Said, S. M., Miyazaki, Y., Masjuki, H. H., Shnawah, D. A., Long, B. D., Naito, S. and Bashir, M. B. A., (2015), Thermoelectric properties of microstructurally modified CoSb3 Skutterudite by Hf-addition, Journal of electronic materials. (Accepted January 2016)

LIST OF CONFERENCE:

1. Elsheikh, M.H., Miyazaki, Y., Sabri, M. F. M, Said, M. S, Masjuki H. H., Shnawah, D. A., Naito, S. and Bashir M. B. A. Effect of minor doping on the microstructure of MCo_4Sb_{12} (M = Mn, Hf & $Al_{0.6}$) skutterudite thermoelectric material synthesized by Mechanical Alloying and Spark Plasma Sintering. 5th international conference on functional material and devices, 4th - 6th August 2015. Johor Bahru, Malaysia.

2. M.H. Elsheikh, Y. Miyazaki, M.F.M. Sabri, S.M. Said, M.H. Hassan, D.A. Shnawah, S. Naito and M.B.A. Bashir. Microstructural modification of $CoSb_3$ skutterudite thermoelectric material through Al exceed doping, 14th International Union of Materials Research Societies-International Conference on Advanced Materials (IUMRS-ICAM 2015), October 25(Sunday)~29(Thursday), 2015. Jeju, Korea.